AN ABSTRACT OF THE THESIS OF

Andrew John Cihonski for the degree of Doctor of Philosophy in
Mechanical Engineering presented on September 19, 2012.

Title:

Modeling and Simulation of Volume Displacement Effects in Multiphase Flows

Abstract approved: _____

Sourabh V. Apte

There are many options available when selecting a computational model for
two-phase flows. It is important to understand all the features of the model
selected, including when the model is appropriate and how using it may affect
your results. This work examines how volume displacement effects in two-phase
Eulerian-Lagrangian models manifest themselves. Some test cases are examined
to determine what input these effects have on the flow, and if we can predict
when they will become important. Bubble injection into a traveling vortex ring is
studied in-depth, as it provides significant insight into the physics of these
volume displacement effects. When a few bubbles are entrained into a traveling
vortex ring, it has been shown that even at extremely low volume loadings, their
presence can significantly affect the structure of the vortex core (Sridhar & Katz
1999). A typical Eulerian-Lagrangian point-particle model with two-way coupling

for this dilute system, wherein the bubbles are assumed subgrid and momentum point-sources are used to model their effect on the flow, is shown to be unable to accurately capture the experimental trends of bubble settling location, bubble escape, and vortex distortion for a range of bubble parameters and vortex strengths. Accounting for fluid volume displacement due to bubble motion, using a model termed as volumetric coupling, experimental trends on vortex distortion and bubble settling location are well captured. The fluid displacement effects are studied by introducing the notion of a volume displacement force, the net force on the fluid due to volumetric coupling, which is found to be dominant even at the low volume loadings investigated here. A method of quantifying of these forces is derived and used to study the effects for a wide range of particle to fluid density ratios in Taylor-Green vortices. A simple modification to the standard point-particle Lagrangian approach is developed, wherein the interphase reaction source terms are consistently altered to account for the fluid displacement effects and reactions due to bubble accelerations.

Modeling and Simulation of Volume Displacement Effects in
Multiphase Flow

by

Andrew John Cihonski

A THESIS

submitted to

Oregon State University

in partial fulfillment of
the requirements for the
degree of

Doctor of Philosophy

Presented September 19, 2012
Commencement June 2013

Doctor of Philosophy thesis of <u>Andrew John Cihonski</u> presented on <u>September 19, 2012</u>.

APPROVED:

_____

Major Professor, representing Mechanical Engineering

_____

Head of the School of Mechanical, Industrial and Manufacturing Engineering

_____

Dean of the Graduate School

I understand that my thesis will become part of the permanent collection of Oregon State University libraries. My signature below authorizes release of my thesis to any reader upon request.

_____

Andrew John Cihonski, Author

ACKNOWLEDGEMENTS

TABLE OF CONTENTS

TABLE OF CONTENTS (Continued)

LIST OF FIGURES

LIST OF FIGURES (Continued)

LIST OF TABLES

LIST OF APPENDIX FIGURES

LIST OF APPENDIX TABLES

DEDICATION

To My Parents...

Modeling and Simulation of Volume Displacement Effects in Multiphase Flow

Chapter 1 – Introduction

Particle and bubble-laden turbulent flows are found in a wide variety of engineering applications. From electrostatic precipitation, riser and downer flows in production processes, engines and furnaces, contaminant transport, pollution control, micro-bubble induced drag reduction in a turbulent boundary layer [5], chemical mixing in bubble column and stirred tank reactors [6, 7], cavitating tip vortex flows [8] to the breakup/coalescence of bubbles in swirl atomizers [9]. In these processes, an accurate understanding of particle or bubble dispersion and turbulent flow fields is important to be able to adequately model and assess various system properties. Improving our understanding of dispersion modeling is key because the efficiency and performance of many devices depends intimately on our understanding of these mechanisms. This motivates the current work on understanding and improving the available modeling techniques for two-phase flows.

Figure 1.1 is a map, adapted from Balachandar & Eaton (2010) [2], of Stokes number (St_b) versus the ratio of the dispersed phase (bubble/particle) diameter (d_b) to the smallest flow scales resolved on the computational grid ($\Delta_{cv} = \mathcal{V}_{cv}^{1/3}$, where $\mathcal{V}_{cv}$ is the volume of the computational cell) and the corresponding numerical modeling approaches that can be used. For example, for small Stokes numbers ($St_b < 10^{-3}$), the bubbles mainly act as tracers and a dusty gas or equilibrium Eulerian approach ($10^{-3} < St_b < 10^{-1}$) [10] are applicable and most efficient. For the range $10^{-1} < St_b < 1$, a two-fluid Eulerian approach [11, 12] is valid, wherein the carrier fluid and the dispersed bubble phases are represented by interpenetrating fluid media, and Eulerian conservation equations are solved for the fluid as well as the dispersed phase together with a concentration evolution equation. Such an

approach is advantageous for large numbers of dispersed phase particles. The Lagrangian point-particle approach [13, 14] is the most commonly used technique for moderate sized dispersed phase (up to millions of bubbles/particles) with larger Stokes numbers ($St_b > 0.1$). In this approach, the dispersed phase is assumed subgrid in scale (smaller than the smallest grid resolution used), and particle dynamics equations are solved in a Lagrangian frame. The momentum exchange between the dispersed and continuum phases are modeled as point-sources.

The point-particle approach is strictly valid for dispersed particles that are much smaller than the smallest flow scale (for example, the Kolmogorov scale, $\eta \approx \Delta_{\mathrm{cv}}$, in turbulent flow, when the fluid flow equations are solved using direct numerical simulation (DNS)). However, this approach is often utilized even when it is not strictly valid for lack of computational power to resolve all the necessary scales to improve it. For $d_b/\Delta_{\mathrm{cv}} > 0.1$, the finite-size effects of the dispersed particles, such as wakes and mass/volume displacement become important. For such cases, a fully resolved simulation, wherein all length scales and the associated dynamics of the two-phase system are completely resolved on the computational grid, is necessary; however, it can be prohibitively expensive for a large number of dispersed particles. Under such conditions, the Lagrangian point-particle approach is potentially the only viable approach, meaning it is important to develop less expensive two-fluid and Eulerian-Lagrangian models capable of reproducing experimentally observed fundamental physics of bubble-laden turbulent flows. This is important not just for simulations of small scale bubble-fluid interactions, but also for the development of closures for higher order models based on the Reynolds
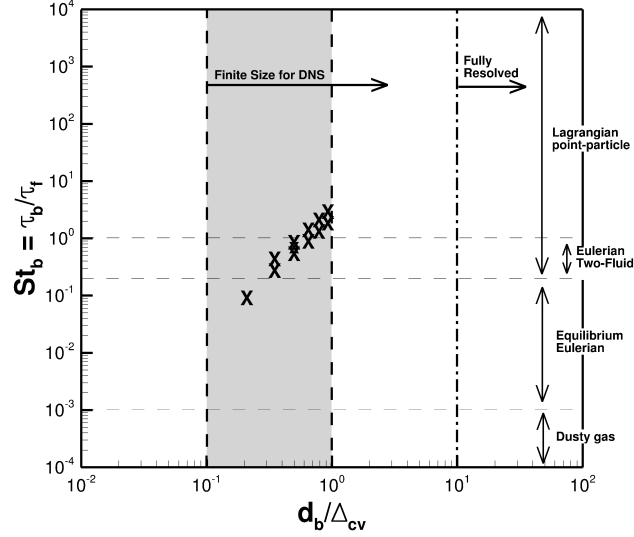
Figure 1.1: A map of the bubble Stokes number versus the non-dimensional bubble size (d_b/Δ_{cv}), modified after [1, 2]. The bubble size is non-dimensionalized by the size of the smallest scales of the flow; which are generally proportional to the grid resolution, for example in a direct numerical simulation. Also marked, by X are the cases presented in the present work on bubble-vortex ring interactions (section 5).

Averaged Navier-Stokes equations. Of particular interest are methods for handling bubbles whose size is near that of the smallest resolved fluid scales. Around this scale, individual particles/bubbles are large enough to displace a significant amount of fluid mass as they move, but are too small to be modeled with any sort of resolved approach.

There are several ways to implement Lagrangian point-particle models for disperse multiphase systems [15]. The three traditional methods are known as (i) one-way coupling, (ii) two-way coupling, and (iii) four-way coupling. A series of
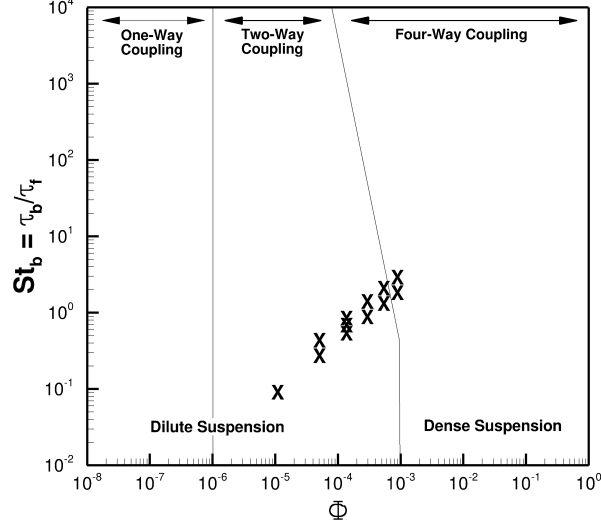
Figure 1.2: Map of Stokes number versus volume loading, modified based on El-ghobashi (2006) [3], identifying different momentum transfer modeling approaches applicable for particle-laden flows. The cases presented on bubble-vortex interaction in this work are marked with an X (section 5).

works aimed at classifying the dominant mechanisms in particle-laden isotropic turbulence were performed [15, 16, 3], which led to the development of a map relating the particle Stokes number and system volume fraction (ϕ) to the dominant mechanisms of inter-phase momentum transport. Figure 1.2 shows this map adapted from [3], which is designed to reflect the effect on the global flow structures, not necessarily local transient effects.

In one-way coupling, the fluid phase moves the disperse phase, but the reaction force of the particles onto the fluid is considered negligible. In general, this approximation is considered valid when both the volume loading and Stokes number of the dispersed phase are small, in other words, when the disperse phase is expected

to have minimal influence on carrier phase motion. The majority of studies based on the Lagrangian point-particle approach for practical applications utilize a two-way coupling method, in which the disperse phase is modeled as a collection of point sources in the carrier fluid momentum equation. For example, several simulations of particle-laden flows have been performed with the carrier fluid simulated using direct numerical simulation [17, 18, 19, 20, 21, 22], large-eddy simulation [23, 24, 25, 26], or Reynolds-Averaged Navier-Stokes equations [27, 28].

The two-way coupling approximation is valid when inter-phase momentum transport is dominated by the drag between individual elements of the dispersed phase and collisions between the dispersed phase do not alter the momentum transfer significantly. For dense-suspensions (large volume loadings), however, inter-particle collisions must be accounted for in addition to the two-way coupling effects, in a model termed four-way coupling. Four-way coupling can be important even under some moderate loadings, such as the particle-laden jet by Lain & Garcia (2006) [29] or turbulent channel flows by Yamamoto et al. (2001) [30], and are necessary for applications involving fluidized beds and bubble-column reactors [7].

The aforementioned coupling methods typically neglect the fact that locally the dispersed phase can displace fluid mass. In many systems these effects may be unimportant, such as an air pipe flow laden with copper beads [22], where the drag from the two-way reaction coupling force is dominant mechanism of momentum exchange. For many densely loaded systems, the fluid mass displacement effects are accounted as part of the four-way coupling formulation, for example, bubble-liquid interactions in column mixers [6], rising bubble columns [31], boundary layer

drag reduction [32, 33]; among others. Two-fluid formulations, implicitly include these effects, through local variations in dispersed phase concentration [11, 34], owing to the assumption that these effects are only dominant when the dispersed phase volume fraction is significant.

In the present work it is hypothesized that the local fluid mass (or volume) displacement effects are important even under dilute loadings, especially for lighter-than fluid dispersed bubbly flows [31, 35] or particle-fluid systems with small specific gravity such as sediment flows [36], wherein the two-way interaction force can be very small. In order to distinguish these effects from the standard momentum coupling techniques described above, we refer to this model as *volumetric coupling* in this work. The main hypotheses that are central to this work are:

- for subgrid but large dispersed bubbles/particles ($0.1 < d_b/\Delta_{\mathrm{cv}} < 1$), a point-particle Lagrangian approach, with standard two-way inter-phase momentum coupling, may be insufficient to accurately capture the effect of the bubbles on the fluid flow;

- the fluid volume displacement effects associated with the motion of the bubbles/particles, as well as due to local clustering, are important and should be accounted for to appropriately capture the effect of the bubbles on the fluid flow, even for low volume loadings.

A major objective of this work is to show that particle and bubble-laden flows in this regime can be effectively modeled using an Eulerian-Lagrangian approach

which accounts for the volumetric displacement effects of the dispersed phase. In order to test these hypotheses, a few test cases of a particle-laden turbulent channel flow, a traveling vortex ring laden with a small number of micro bubbles and particle/bubble-laden Taylor-Green vortices are considered since detailed experimental, computational and analytic data is available for these scenarios.
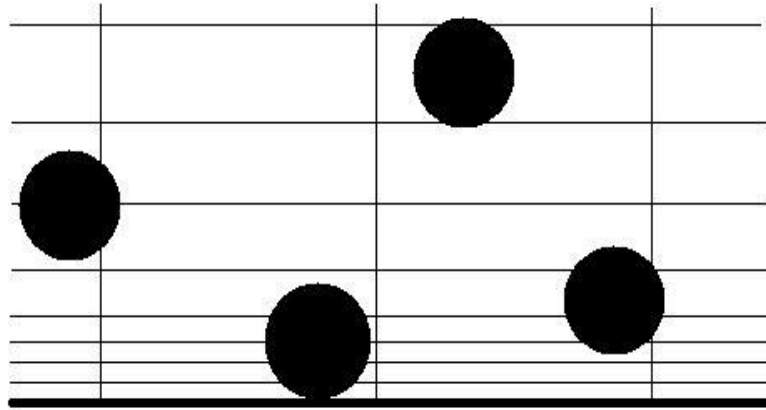
Figure 1.3: *Example of a possible near wall region snapshot. The particle volume may be a significant portion of the near wall grid cell volume and the particle diameter can be much larger than the wall-normal grid spacing.*

It was theorized that these volume displacement effects may become important in dense particle-laden flows with certain characteristics. Figure 1.3 shows an example of a close up of the near wall section of a channel flow. While the volume of the individual grid cells is larger than the volume of a particle, the wall normal grid cell length is less than the particle diameter for the near wall cells. Even

though the volume is larger, the ratio of the cell volume to the particle volume will not necessarily be high, just greater than one. Thus the flux into and out of grid cells due to particle motion could be quite large when accounting for the fluid displaced by the particles. This work studies how this feature affects a particle-laden channel flow at low to moderate mass loadings.

Using the results of the turbulent channel flow case, which notes that a significant volume fraction is not a sufficient condition for volume displacement effects to be important, the focus will change to the particle/bubble to fluid density ratio. It has been shown in experiments that under certain conditions a few small bubbles, corresponding to the conditions marked by an X is figures 1.1 and 1.2, can drastically alter local flow structures in a traveling vortex ring [4]. In the map, the bubble Stokes number is obtained as $St_b = \tau_b/\tau_f = \rho_b \overline{\omega} d_b^2 / 36\mu_\ell$, where $\tau_b = \rho_b d_b^2 / 36\mu_\ell$ is the bubble response time scale, $\tau_f = 1/\overline{\omega}$ is the small feature fluid time scale, $\overline{\omega}$ is the mean local vorticity, d_b is the bubble diameter, and μ_ℓ is the dynamic viscosity. These maps indicate that a two-way coupling Lagrangian point-particle approach is appropriate for this problem. However, it will be shown that solely utilizing the two-way momentum coupling methods is not sufficient to reproduce the experimental observations. It should also be noted that the cases studied fall in the range of $0.1 < d_b/\Delta_{\text{cv}} < 1$ (figure 1.1), for which the standard Lagrangian point-source approximation is not strictly valid; however, performing fully resolved simulations is computationally expensive. A study of how the particle to fluid density ratio is a strong input factor toward the relevance of volume displacement effects follows. This is done by studying force measurements

in Taylor-Green vortices. Finally, a mathematical formulation for a more efficient implementation of volume displacement force sources is proposed.

Table 1.1: Nomenclature.

Symbol	Meaning	Symbol	Meaning
St_b	Stokes Number	Re	Reynolds Number
Re_{vx}	Vortex Reynolds Number	RE_b	Bubble Reynolds Number
ρ_ℓ	Fluid Density	ρ_b	Bubble Density
ρ_p	Particle Density	F_d	Drag Force
F_ℓ	Lift Force	F_{am}	Added Mass Force
F_p	Pressure Force	F_{p^d}	Dynamic Pressure Force
F_{p^h}	Hydrostatic Pressure Force	F_h	History Force
F_g	Gravity Force	g	Gravity
C_D	Drag Coefficient	C_ℓ	Lift Coefficient
C_{am}	Added Mass Coefficient	d_b	Bubble diameter
α	Normalized Rotation	μ_ℓ	Dynamic Viscosity
ν_ℓ	Kinematic Viscosity	θ_ℓ	Fluid Volume Fraction
θ_b	Bubble Volume Fraction	$\mathbf{u}_b$	Bubble Velocity
$\mathbf{u}_\ell$	Fluid Velocity	$\mathbf{u}_{\ell,b}$	Fluid Velocity at Bubble Location
$\mathbf{x}_b$	Bubble Location	$\mathbf{x}_{cv}$	Control Volume Center Location
ϕ	Bubble Volume Fraction	p	Pressure
Γ_0	Circulation	y^+	Wall Units
r_s	Bubble Settling Distance	r_c	Vortex Core Radius
θ_s	Bubble Settling Angle	$\overline{\omega}$	Mean Vorticity
$\mathcal{V}_b$	Bubble Volume	m_b	Bubble Mass
$\Delta\mathbf{V}$	Volumetric Coupling Force	$\mathbf{f}_{b\to\ell}$	Momentum Coupling Force
u_τ	Wall Slip Velocity	W_b	Bubble Weight
N_b	Number of Bubbles	I	Vortex Distortion Index

Chapter 2 – Literature review

A few issues and terminologies pertinent to this work will now be defined and discussed. This overview will be split into sections on numerical modeling methods, coupling methods and their consequences and bubble-vortex interaction. These topics are of direct importance to the work presented, so a comprehensive understanding of these mechanisms is an important foundation to effective multiphase flow modeling. These sections will simply present a broad view of these topics, a more thorough overview can be found in sources such as [37] [38] [7] [16] [39].

2.1 Modeling Methods

As mentioned previously, there are several options available for modeling multiphase flows, the method of choice is completely dependent upon the application and the resources available. Several common methods for this will be presented as well as a discussion of some of their various strengths and weaknesses.

The first method is a Lagrangian-Lagrangian technique known as a molecular dynamics modeling, in which both the carrier fluid phase and the dispersed particle phase are treated in a Lagrangian manner, which in this case refers to the treatment of particles individually. Each particle is tracked separately and it's motion governed by Newton's Laws of motion. Interphase effects are based on the collisions of carrier phase molecules with particles. These types of models can be very accurate, but are extremely limited in scope due to the computational cost of simulating a significant domain. Essentially these models are only viable for extremely small scale domains. Higher level models would be more appropriate for

handling the current work [7].

The next method utilized is an Eulerian-Lagrangian construct known as fully resolved simulation. The carrier phase is treated as an Eulerian quantity in which the motion is calculated using direct numerical simulation for the fluid equations of motion, thus resolving all the scales of motion from the integral scale down to the Kolmogorov scale. This yields a high degree of accuracy for pure fluid motion, the interaction with the particle phase is the next concern. Particles are fully resolved and thus their motion requires no modeling. This method is quite expensive because the grid scales must be small everywhere to resolve the no-slip condition around the particle, not just at the wall. Another method utilizes direct numerical simulation for the fluid phase, but the particles are not fully resolved, thus modeling is required. Particles are handled in a Lagrangian sense with the motion of the particles determined by a set of equations, for example the equations of motion developed by Maxey and Riley [40], which describes the rigid body motion of a sphere. The velocity field around the particles is well resolved yielding accurate trajectories for particles. Direct numerical simulation provides a great tool for building sub-grid scale models for use in large-eddy simulation [41] [7] .

Similar to the previous method, another example of an Eulerian-Lagrangian method is unresolved simulation, the prime example of which is large-eddy simulation. In large-eddy simulation, the carrier phase motion is solved on a relatively coarse grid compared to direct numerical simulation, thus where the name large-eddy simulation comes from. The smallest eddies are not resolved with the grid, only the motion of the largest eddies is directly computed. The particle phase

is handled in a similar manner to the resolved modeling efforts, the velocity field is however not resolved around the particle. Since the vast majority of the dissipation occurs at the smallest scales a model must be implemented in order to effectively have the energy balance within the flow. Large-eddy simulation is a logical choice for the types of flows being studied as the lower Reynolds numbers make it tractable for simulation unlike some high Reynolds number external flows [37] [24] . It is also a good tool for building closure models and an understanding of particle behavior in complex systems in order to build two-fluid models [7].

The next larger level models are Eulerian-Eulerian, such as the two-fluid model in which both phases are treated as continuum quantities, thus individual particles are no longer being followed [7]. Conservation of mass and momentum equations must be solved for both phases [42] [43]. The interaction between the phases and between particles is handled using models based on spatial volume fraction gradients [42]. With accurate models for this behavior two-fluid models can be just as concise and considerably less computationally expensive than Euler-Lagrangian simulations. Studies show that even with the current underdeveloped two-fluid modeling closures good accuracy can be achieved with more than two orders of magnitude less effort than direct numerical simulation [41] [11]. The main downfalls of this method are it's failures when high particle concentration gradients occur and/or when the dispersed phase volume fraction is low.

Another type of method that is often utilized for its computational efficiency is known as Reynolds Averaged Navier-Stokes modeling. In this method the physical parameters are split into a mean and fluctuating component and then substituted

into the equations of motion. The equations are then time averaged, this process then relates mean properties of the flow with one unknown quantity. This quantity is known as the Reynolds stress tensor because it represents forces on the a local fluid volume due to turbulent stresses. Several attempts have been made to relate this unknown tensor to the current variables in order to close the system. These have been met with varying degrees of success. The two most common closure methods are the k-ϵ and k-ω models. In these models dimensional analysis yields a relationship for the various Reynolds Stress tensor quantities, then are provided by solving transport equations for say k and ϵ if the k-ϵ model is being used. These quantities are then used to solve the fluid momentum equation. Several models are used to include the effect of particles on the fluid phase, see for example [44] [45] [46]. These models seem to be effective for well understood systems where the needed relationships have been well established and tested. This is not ideal for true predictive capability in new flows and geometries. The common complaints about Reynolds Averaged Navier-Stokes models (RANS models) are that in more complex geometries the inaccuracies in calculating fluid phase motion can be significant. When the fluid phase properties are not handled properly the motion of the particles is then not calculated properly as a result [24] [47] [23]. When this happens the two-way coupling effect causes non-physical momentum transfer back to the carrier phase further eroding the accuracy. These inaccuracies yield both problematic fluid and gas phase velocities but also improper particle dispersive behavior [47]. Also, in RANS simulations particles are often treated as parcels of particles. The implementation of this method has implications that

are not always clearly understood with respect to handling phase-coupling and collisions [24].

The most popular methods of handling particle-laden flows have been discussed, however other techniques exist but are considerably less popular. For example, using the integrated Boltzmann equations with a variety of possibilities for handling the particle phase, such as Lagrangian particle tracking or stochastic motion modeling [48]. A more rare method uses Lagrangian eddy interaction models and Lagrangian particle tracking, but seems to be limited in its scope [49]. The last of the less common methods that will be mentioned is vortex simulation with Lagrangian particle tracking [50]. A more robust review of the common modeling methods can be found in the literature, such as Deen et al. (2007) and van der Hoef et al. (2008) [7] [51] .

2.2   Flow Regimes and Coupling Methods

There are two properties in particular which seem to determine the regime in which varying processes tend to dominate the characteristic behavior. The particle Stokes number, or the relative particle response time scale to the flow's small structure time scale is one, the other is the particle volume fraction. At low loadings the particles *tend* to exert an extremely low level of influence on the flow structure, as such these low loadings are known as the one-way coupling regime where the fluid structure determines the particle phase motion, but the particle motion has a negligible effect on the flow structure. At higher loadings the particles become

numerous enough that based on their size, their combined momentum coupling to the carrier phase becomes significant. At the higher end of the regime the dominant process is the momentum transfer between the phases, overshadowing the carrier phase flow field. This regime is known as the two-way coupling regime because the dominant physics is determined by the momentum transfer from the carrier phase to the particulate phase and vice versa. At even higher loadings the inter-particle collisions come to dominate the momentum transfer, this is termed four-way coupling, two for the coupling between the carrier and particulate phases and two for the coupling between colliding particles.

2.2.1   One-Way Coupling

When a method for simulation is chosen for a given flow configuration it is often beneficial to make approximations. One of the most rudimentary approximations we can make for such flows is known as the one-way coupling approximation. In this approximation the fluid phase motions are used to push the particles, thus particle motion is determined through this fluid phase motion and a basic laws, such as that of drag from flow over a sphere. In some studies additional forces can be considered on the particle such as lift, added mass, etc. Physically it is understood that the particles can transfer momentum back to the fluid through the no-slip boundary condition. This is where the name of the approximation comes from, the momentum is only transferred in one way, from the fluid to the particles. As stated before, this is not a physical reality, this is an approximation meant to save

time and/or effort for both the user and computer. This approximation is ideal for dilute flows containing particles of low Stokes number [52] [53] [3]. For flows with higher volume loadings a more involved approximation is used in order to achieve some reasonable measure of accuracy.

2.2.2 Two-Way Coupling

In studies involving so called two-way coupling an added level of complexity is seen. The two-way coupling is so named because momentum is transferred from the fluid to the particles and then echoed back from the particles to the fluid in differing quantities, thus the momentum is transferred in two ways. From this explicit fluid phase information several forces acting on the particle can be calculated. These forces can be drag, gravity, pressure, added mass, lift and others. When the explicit velocity field is known and the particle properties are known the second aspect of the two-way coupling force can be calculated. This is the momentum that the particle imparts on the fluid through it's relative motion within with carrier phase.

It is common practice in many heavy particle-laden flows to assume that the drag and gravity forces are the only ones acting on a particle. While this is, in general a good approximation, other authors have evaluated the importance of other forces. While the overall conclusion is the same, it is not entirely clear exactly when and to what degree these small forces could have a large effect [21] [54].

2.2.3 Four-Way Coupling

The so called four-way coupling approximation is named so because it uses the same two methods of transferring momentum as two-way coupling, as well as includes the ability for particles to transfer momentum among themselves. Thus particle A transferring momentum to particle B is the third way, and the reverse process constitutes the fourth method of coupling. The inclusion of these computations becomes important when inter-particle collisions begin to lead to preferential accumulation, thus the momentum transfer between particles and their then augmented momentum transfer to the fluid become the dominant factors in determining flow characteristics [11]. This behavioral regime tends to be dominant in flows with large volume fractions or more moderate volume fractions but consists of particles with larger Stokes numbers [3].

2.2.4 Volumetric Coupling

When Lagrangian particle tracking methods were first utilized they made what is commonly called the point-particle assumption. This means that the carrier phase has no knowledge of particle volume, as such the particles displace no mass, acting as a point source. The particles are tracked based on their center location and their motion was determined through the a fore mentioned methodology. The only manner in which the mean flow knows of the particle existence is through a momentum source in the fluid momentum equations. For many types of flows this may be a perfectly valid approximation because either the displaced mass is small

due to a low particle volume fraction, or the dynamics of the flow are not strongly effected by more moderate amounts of displaced mass [36]. This is a major subject of the current work.

Several studies have developed different methods for taking into account the fluid displaced by the presence of particles. The importance of this effect can vary drastically depending on the physical system being studied. In some systems, such a collection of particles under the influence of gravity settling into a pile, the inclusion of finite-sized effects is small since the dominant physics are the effects of gravity and inter-particle collisions [36]. Lun (2000) used $k - \epsilon$ and $k - \omega$ Reynolds averaged Navier-Stokes models respectively to study particle-laden jet and particle-laden channel flows [45]. It is difficult to interpret the results of their work and apply it to direct numerical simulation or large-eddy simulation methods. The reason for this is the large relative grid size differences between the methods. In DNS and LES, the grid cells are not large in the wall-normal direction in comparison with the particle diameter whereas, typically the cell size requirements are not as strict in RANS modeling. In Eulerian-Lagrangian modeling efforts such as DNS and LES, the assumption of having subgrid scale particles is an important one, but can break down in the near wall region [36]. Studies have shown that even for relatively dilute flows the local particle clustering properties can vary with the inclusion of finite sized effects [36].

2.3   Vortex-Bubble Interaction

The interaction of bubbles with vortical flow features serves as an important canonical problem to advance our basic understanding of more complex flows where such flow structures are common, such as turbulent, separated or wall-bounded flows and has been studied extensively. Oweis et al. (2005) [55] studied the properties of bubble capture and cavitation in a line vortex. Their study utilized a one-way coupling approach to predict capture times, which was found to be accurate when utilized for small bubbles, but was not sufficient when bubble growth was a significant factor. Several groups, see [56], [57], [58] and [59], utilized experimental methods to determine the appropriate choices for drag and lift coefficients on bubbles in vortical structures. In studying these lift and drag coefficients, Sridhar & Katz (1995) [59] found significantly higher lift coefficients than were present in many previous studies and suggest that an appropriate choice of drag model is very important within an isolated vortical structure to predict bubble behavior. Two-way coupling of bubble interactions with homogeneous isotropic turbulence was investigated by Mazzitelli & Lohse (2003) [60]. They concluded that bubble accumulation on the downward side of vortices was primarily due to the lift force, in what is known as the preferential sweeping mechanism. Deng et al. (2006) [61] experimentally investigated the behavior of bubbles in a Taylor vortex wherein the drag and buoyancy forces are in balance, in line with later observation in this work. An equilibrium position is derived for a bubble in a horizontally rotating cylinder with the suggestion of investigating changes in lift models [62].

Sridhar & Katz (1999) [4] showed that a few small Stokes number bubbles have the ability to augment the core structure of both laminar and turbulent traveling vortex rings during their entrainment cycle. This is significant due to the extremely low overall volume fraction in comparison with the magnitude of the core distortion observed. The case of bubble entrainment into a traveling vortex ring was chosen to test the ability of the volumetric coupling approach to predict the experimental trends for this low volume loading case. This case is also ideally suited to identify the effects of volume displacement, as the bubbles tend to settle in a small region away from the ring center, where all the forces on the bubbles are in balance. The effect of any point-source reaction force on the flow structure is thus generally small.

Recently, Finn et al. (2011) [35] investigated a two-dimensional generalization of this problem, by studying a traveling vortex-tube laden with a few microbubbles, wherein a periodic boundary condition was used in the direction of the vorticity vector. With dilute bubble volume loadings ($< 10^{-2}$), the volumetric displacement effects due to bubble motion were found to be significant. Results from that work suggested that for the two-dimensional vortex tube there was a decrease in the local vorticity at the core center and volume displacement effects were necessary for significant vortex distortion to occur. However, periodicity in the spanwise direction, implied that there are several bubbles in the plane normal to the propagation of the vortex tube. In this work, it will be verified that even in a three-dimensional vortex-ring configurations, these effects are dominant in comparison to two-way coupling momentum transport. The concept of a *volumetric coupling force*, the

force induced on the liquid due to volume displacement effects, will be developed and compared with the standard two-way coupling force to evaluate their relative magnitudes.

2.4 Outline of Present Work

This section gives an overview of the work presented. Chapter 3 outlines the mathematical formulation used in this work for the fluid phase motion, particle motion, coupling and inter-particle collisions, section 3.4 discusses the numerical methods used to implement the mathematical formulation. Chapter 4 will provide analysis of a particle-laden channel flow to determine the role volumetric coupling effects play in dense particle-laden flows at dilute to moderate loadings. A traveling vortex ring with a small number of low Stokes number bubbles injected into is studied in chapter 5. A mapping method to determine when volumetric effects will be important is proposed and some preliminary studies done in using a Taylor-Green vortex setup laden with particles and bubbles in chapter 6. Chapter 7 provides an overview of the work and results presented here as well as discusses methods of improving the work for future studies.

The methods for computing the fluid phase flow, particle motion, coupling forces and inter-particle collisions are presented within. A validation case of Taylor-Vortex flow is given in Appendix A. Turbulent channel flow results are presented in Appendix B at a Reynolds number of 180 and the effect of varying the Reynolds number is shown in the same section. A collision model test case of crossing

particle jets is shown in Appendix C. Some validation work on bubble settling location prediction compared with analytic solutions is discussed in Appendix D. In Appendix E some sample grid refinement studies are presented for the three-dimensional traveling vortex ring case.

Chapter 3 – Mathematical Formulation

In the present volumetric coupling formulation, the bubbles are assumed spherical, subgrid scale and constant in size. Standard Lagrangian particle tracking is performed to track the centroid of the bubble by using closure models for the various forces exerted by the flow on the bubbles. The reaction of the bubbles on the fluid is handled as a point-source, similar to the two-way coupling methodology. In addition, the effect of fluid displaced by the bubbles is accounted for through the local bubble volume fractions, computed by mapping the Lagrangian bubble location and its volume onto a fixed Eulerian grid used for fluid flow solutions. In the present work, all scales associated with the undisturbed fluid flow are captured on the computational grid by using a fine enough mesh, similar to a direct numerical solution procedure. Bubble-bubble collisions are neglected due to the fact that only eight bubbles are used in all of the cases studied, resulting in extremely low volume fraction (see figure 1.2). It was also verified in the computation that the bubble trajectories rarely cross over the duration of the simulation.

3.1 Dispersed Phase

The bubble phase is handled using the equations of motion developed by Maxey & Riley (1983) [40]. Forces on bubbles are computed from explicit carrier (liquid) phase information. The forces are used to update the bubble velocity and position by solving the following system of ordinary differential equations 3.1 and 3.2.

$$\frac{d}{dt}(\mathbf{x}_b) = \mathbf{u}_b \tag{3.1}$$

$$m_b\frac{d}{dt}(\mathbf{u}_b) = \sum \mathbf{F}_b. \tag{3.2}$$

Here, $\mathbf{x}_b$ is the bubble location, m_b is the mass of an individual bubble, $\mathbf{u}_b$ is the bubble velocity vector and $\mathbf{F}_b$ denotes the force acting on a bubble. In this case $\mathbf{F}_b$ can be broken up into the gravity ($\mathbf{F}_g$), drag ($\mathbf{F}_d$), lift ($\mathbf{F}_\ell$), added mass ($\mathbf{F}_{am}$), and pressure ($\mathbf{F}_p$) forces on the bubble.

$$\sum \mathbf{F}_b = \mathbf{F}_g + \mathbf{F}_d + \mathbf{F}_\ell + \mathbf{F}_{am} + \mathbf{F}_p. \tag{3.3}$$

The gravitational force is simply taken as the weight of the bubble, where $\mathbf{g}$ is the gravitational acceleration ($\mathbf{g} = 9.81 m/s^2$ vertically), and is given as

$$\mathbf{F}_g = -\rho_b \mathcal{V}_b \mathbf{g}, \tag{3.4}$$

where the volume of the individual particle is denoted by $\mathcal{V}_b$ and the bubble density is ρ_b. The drag force on the bubble is modeled using the standard drag equation for flow past a sphere,

$$\mathbf{F}_d = -\frac{1}{8}C_d\rho_\ell\pi d_b^2|\mathbf{u}_b - \mathbf{u}_{\ell,b}|(\mathbf{u}_b - \mathbf{u}_{\ell,b}), \tag{3.5}$$

where C_d is the drag coefficient, ρ_ℓ is the liquid density, d_b is the bubble diameter,

$\mathbf{u}_b$ is the bubble velocity and $\mathbf{u}_{\ell,b}$ is the local fluid velocity vector interpolated at the bubble centroid. This solid sphere viscous drag model choice is appropriate for this system because the impurities that gather on a real bubble's surface create a no-slip condition [63, 64]. Experiments by Sridhar & Katz (1995) [59] also indicate presence of 'dirty' bubbles. Here, $\mathbf{u}_{\ell,b}$ strictly denotes the 'undisturbed' fluid velocity at the bubble location, which is close to the local fluid velocity for small, subgrid bubbles, as studied in this work. For larger bubbles, finding $\mathbf{u}_{\ell,b}$ is not straightforward, and may require additional modeling including stochastic components to the drag forces. Such second-order changes to the drag force, may alter the bubble trajectory slightly, however, its influence on the volume displacement effects to be studied in this work are negligible. For the Reynolds number ranges and bubble mass loadings being studied here, the Schiller & Naumann (1933) [65] drag curve has been selected. In this model the drag coefficient is determined using,

$$C_d = \frac{24}{Re_b}(1 + 0.15 Re_b^{0.687}), \tag{3.6}$$

in which Re_b is the bubble Reynolds number, given by $Re_b = (\rho_\ell d_b |\mathbf{u}_b - \mathbf{u}_{\ell,b}|)/\mu_\ell$, where μ_ℓ is the dynamic viscosity of the fluid.

The lift force is modeled based on the experimentally determined lift model [59] for this particular configuration,

$$\mathbf{F}_\ell = -C_\ell \rho_\ell \pi r_b^2 (\mathbf{u}_b - \mathbf{u}_\ell) \times (\nabla \times \mathbf{u}_\ell). \tag{3.7}$$

In this study, they emphasized the importance of C_L on bubble trajectory and

settling location. Their experimentally determined lift model gave higher coefficients, C_ℓ, than most analytically developed models. In the present work, the experimentally determined lift coefficient is used and is given as,

$$C_\ell = 0.22\alpha^{-3/4}; \quad \text{where} \quad \alpha = \frac{|\nabla \times \mathbf{u}_{\ell,b}|d_b}{2|\mathbf{u}_{\ell,b} - \mathbf{u}_b|} \tag{3.8}$$

Here α is a measure of the local rotation over the relative velocity of the carrier and dispersed phases. The lift force models how the particle interacts with local gradients across the diameter of the particle. The added mass force ($\mathbf{F}_{am}$) is modeled as, basically

$$\mathbf{F}_{am} = -\frac{1}{2}\rho_\ell \mathcal{V}_b \left(\frac{d\mathbf{u}_b}{dt} - \frac{D\mathbf{u}_\ell}{Dt} \right). \tag{3.9}$$

Here, D/Dt is the total derivative following a fluid parcel and d/dt is the derivative following the bubble velocity. The standard added mass coefficient of $1/2$ is used. The added mass force represents the additional mass carried around by a bubble or particle. Thus, when forces act on the dispersed phase, they act on both the particle itself, as well as the fluid attached to it.

The far-field pressure force on the bubbles is due to the buoyancy force (hydrostatic pressure gradient), the inertial forces and the viscous strains,

$$\mathbf{F}_p = -\mathcal{V}_b \nabla p. \tag{3.10}$$

The pressure force can be broken up into two parts, the dynamic pressure F_{p^d} and

hydrostatic F_{ph}. A short note on the history force is given here. The history force can be modeled as

$$\mathbf{F}_h = 6\pi r_b^2 \mu_\ell \int_0^t \frac{d(\mathbf{u}_b - \mathbf{u}_{\ell,b})/d\tau}{\sqrt{\pi \nu_\ell (t - \tau)}} d\tau. \tag{3.11}$$

The history force effects were shown to be smaller than 6% of the buoyancy force at any time for the traveling vortex ring [59]. Due to the settling nature of the bubbles in this system, once the bubbles are settled, the history effect is small, as the relative acceleration is not large compared to $||\mathbf{u}_{\ell,b} - \mathbf{u}_b||^2/d_b$ [66]. The history force is neglected in this work, as its maximum magnitude was determined to be less than one-third of the smallest force component on the bubbles at any time. It is also neglected in the turbulent channel flow as the particle density prevents the history force from being significant.

3.2   Continuous Phase

In the volumetric coupling formulation, the fluid phase equations are altered to account for the mass displaced by the presence and motion of the bubbles [67]. Each bubble occupies a volume, $\mathcal{V}_b$, which corresponds to a local bubble volume fraction, θ_b. The local liquid volume fraction is defined as $\theta_\ell = 1 - \theta_b$. Accounting for the mass of the bubble within a control volume, the conservation of the mass becomes,

$$\frac{\partial}{\partial t}(\rho_\ell \theta_\ell) + \nabla \cdot (\rho_\ell \theta_\ell \mathbf{u}_\ell) = 0, \tag{3.12}$$

where ρ_ℓ is the liquid density. No summation is implied on the subscript ℓ. Note that in this form the flow field, even for an incompressible fluid, is not divergence free as long as the volume fraction changes with time or has spatial gradients. Rearrangement of equation 3.12 yields an expression for the local divergence,

$$\nabla \cdot \mathbf{u}_\ell = -\frac{1}{\theta_\ell} \left(\frac{\partial \theta_\ell}{\partial t} + \mathbf{u}_\ell \cdot \nabla \theta_\ell \right) = -\frac{1}{\theta_\ell} \frac{D\theta_\ell}{Dt}. \tag{3.13}$$

In a similar manner, the conservation of momentum equation is altered to include the presence of bubbles [67, 68, 69, 70],

$$\frac{\partial}{\partial t} \left(\rho_\ell \theta_\ell \mathbf{u}_\ell \right) + \nabla \cdot \left(\rho_\ell \theta_\ell \mathbf{u}_\ell \mathbf{u}_\ell \right) = -\nabla p + \nabla \cdot \left(\theta_\ell \mu_\ell \mathbf{D} \right) - \theta_\ell \rho_\ell \mathbf{g} + \mathbf{f}_{b \to \ell}^t, \tag{3.14}$$

where p is the dynamic pressure in the fluid phase, $\mathbf{D} = \nabla \mathbf{u}_\ell + \nabla \mathbf{u}_\ell^{\mathrm{T}}$ is the deformation tensor. The total reaction force ($\mathbf{f}_{b \to \ell}^t$) from the bubbles onto the fluid per unit mass of fluid contains contributions from the surface forces and is given as,

$$\mathbf{f}_{b \to \ell}^t \left(\mathbf{x}_{cv} \right) = -\sum_{b=1}^{N_b} \mathcal{G}_\Delta \left(\mathbf{x}_{cv}, \mathbf{x}_b \right) \left(\mathbf{F}_p + \mathbf{F}_d + \mathbf{F}_\ell + \mathbf{F}_{am} \right), \tag{3.15}$$

where $\mathcal{G}_\Delta$ denotes interpolation function from the bubble locations on to the Eulerian grid and is constrained by the conservation condition $\int_\mathcal{V} \mathcal{G}_\Delta d\mathcal{V} = 1$. In the present work, a Gaussian interpolation function is used, see [31, 36] for details. Here $\mathbf{x}_{cv}$ and $\mathbf{x}_b$ are the centers of the control volume and bubble, respectively and N_b is the total number of bubbles in the neighborhood of the control volume centered at $\mathbf{x}_{cv}$.

Note that the total force on the bubble consists of the pressure force, $F_p = -\mathcal{V}_b \nabla p$. The reaction of this force onto the fluid phase results in the force density $+\theta_b \nabla p$. This reaction term related to the pressure gradient can be combined with the pressure gradient in the momentum equation to obtain

$$\frac{\partial}{\partial t} \left(\rho_\ell \theta_\ell \mathbf{u}_\ell \right) + \nabla \cdot \left(\rho_\ell \theta_\ell \mathbf{u}_\ell \mathbf{u}_\ell \right) = -\nabla p + \nabla \cdot \left(\theta_\ell \mu_\ell \mathbf{D} \right) - \theta_\ell \rho_\ell \mathbf{g} + \mathbf{f}_{b \to \ell} + \underbrace{\theta_b \nabla p}_{\mathbf{F}_{\mathrm{P}} \text{ Force Density}},$$

(3.16)

where $\theta_b \nabla p$ is the Eulerian force density obtained from the pressure force and $\mathbf{f}_{b \to \ell}$ is the Eulerian force density constructed from the Lagrangian force on the bubbles without the pressure force (equation 3.15 without the pressure force, $\mathbf{F}_p$). Noting that $\theta_b + \theta_\ell = 1$, the above equation can be re-written in a more commonly used form by combining the first and last terms on the right-hand side of the above equation 3.16,

$$\frac{\partial}{\partial t} \left(\rho_\ell \theta_\ell \mathbf{u}_\ell \right) + \nabla \cdot \left(\rho_\ell \theta_\ell \mathbf{u}_\ell \mathbf{u}_\ell \right) = -\theta_\ell \nabla p + \nabla \cdot \left(\theta_\ell \mu_\ell \mathbf{D} \right) - \theta_\ell \rho_\ell \mathbf{g} + \mathbf{f}_{b \to \ell}, \qquad (3.17)$$

This formulation is commonly used in gas-fluidized beds [71, 72, 70, 7]. Note that, in the absence of any fluid velocity, but in the presence of bubbles, the pressure gradient force is then appropriately balanced by the gravity force. The pressure gradient and the gravitational term can also be combined together to remove the hydrostatic part of the pressure field by dropping the gravitational term in the momentum equation. In such a case, the gravitational force on the bubble (equation 3.4) typically includes the buoyancy force.

3.3   Collisions

As discussed in the literature review, the effect of particle-particle and particle-wall collisions on the carrier phase flow and particle dispersion depends greatly on the flow properties, in particular the mass loading within the domain and the Stokes numbers of the particles. The inter-particle collisions are taken into account using the method of Cundall and Strack (cite). The force exerted on a particle due to a collision is given by:

$$\mathbf{F}_{jp}^{P-P} = (k_c \delta_{pj}^{3/2} - \eta_c(\mathbf{u}_p - \mathbf{u}_j) \cdot \mathbf{n}_{pj})\mathbf{n}_{pj} \tag{3.18}$$

$$\text{where: } \delta_{pj} = (r_p + r_j + \alpha) - d_{pj} \tag{3.19}$$

where k_c is the stiffness parameter, η_c is the damping parameter, e is the coefficient of restitution and α is the force range. Here $\mathbf{n}_{pj}$ is the unit vector in the direction connecting the particle centers of particles p and j, r_p and r_j are the radius of particles p and j, d_{pj} is the distance between particle centers . $P-P$ denotes the particle to particle momentum transfer, pj denotes the momentum transfer from particle p to particle j, η_c and α are computed as follows:

$$\eta_c = 2\alpha\sqrt{\frac{m_p k_c}{1+\alpha^2}} \tag{3.20}$$

$$\alpha = -ln(e/\pi) \tag{3.21}$$

Collisions between particles and walls are taken into account in a similar manner to the inter-particle collisions as the dominant physics of the process are analogous.

$$\mathbf{F}_{jw}^{P-W} = (k_c \delta_{pw}^{3/2} - \eta_c(\mathbf{u}_p) \cdot \mathbf{n}_{pw})\mathbf{n}_{pw} \tag{3.22}$$

$$\text{where: } \delta_{pw} = (r_p + r_j + 2\alpha) - d_{pw} \tag{3.23}$$

Following the inter-particle equations F_{jw} denotes the force imparted on the particle by the wall and d_{pw} is the distance between the particle center and the wall. Collisions are considered in some of the turbulent channel cases, and are labeled as such, but are neglected in the traveling vortex ring and Taylor-Green vortex cases.

3.4   Numerical Formulation

A procedure for the solution of the equations from the previous section will now be outlined. The methodology outlined in this section has developed from the original fractional step method of Kim and Moin (1985) [73], to an updated form in Choi and Moin (1995) [74], to a very similar method detailed by Kim and Choi (2000) [75] and then into the present form.

To begin with an explicit Euler advancement, as shown in equations (3.24) and (3.25), is used to project intermediate values of particle and fluid velocities.

$$u_p^{n+1/2} = u_p^{n+3/2} \tag{3.24}$$

$$u_f^n = u_f^{n+1} \tag{3.25}$$

The particle phase locations are taken and velocities are interpolated from the local control volumes to provide a velocity at the point at which the particle exists. The forces acting on the particle are calculated based on the last time steps fluid flow field. Thus the particle motion is determined explicitly. Once each particle is assigned a velocity, the particle equations of motion (3.2) are solved using third order Runge-Kutta with inter-particle collisions being checked for at each iteration. If a collision takes place it is handled and the forces on the particle are augmented to reflect this. Once this has occurred the particle motion solution continues. The particle motion is determined from the forces by equation 3.26.

$$\mathbf{a}_p = \sum F_p / m_p \tag{3.26}$$

The particle acceleration is the utilized to determine the particle velocity and then position using equations 3.27 and 3.28.

$$\mathbf{u}_p^{new} = \mathbf{u}_p + \mathbf{a}_p \Delta t_p \tag{3.27}$$

$$\mathbf{x}_p^{new} = \mathbf{x}_p + \mathbf{u}_p \Delta t_p \tag{3.28}$$

Once the particles have been advanced to the next time step, $(n+1)$, they are once again located using the interpolation function (3.29), their mass is associated with the surrounded control volumes using a Gaussian interpolation kernel (3.30)

$$\Theta_p(\mathbf{x}_{cv}) = \sum_{p=1}^{N_p} \forall_p \mathbf{G}_\sigma(\mathbf{x}_{cv}, \mathbf{x}_p) \tag{3.29}$$

$$G_\sigma(\mathbf{x}_{cv}, \mathbf{x}_p) = \frac{1}{(\sigma\sqrt{2\pi})^3} exp(-\frac{\sum_{k=1}^{3}(x_k - x_{p,k})^2}{2\sigma^2}) \tag{3.30}$$

In volumetric coupling the particle phase has a finite size, this size displaces a certain amount of fluid in each control volume. The volume that has been interpolated to each control volume is summed to find a particle volume fraction within each control volume. The particle volume fraction is then subtracted from one to determine the local fluid volume fraction ($\Theta_f = 1 - \Theta_p$). The fluid volume fraction multiplied by the density ρ_f is then set to be the new local operational density of the fluid.

$$\rho^{n+1} = \rho_f \Theta_f \tag{3.31}$$

This augmented density is used in the momentum equation solver, this is where the code has utilized volumetric coupling. Once this is done and the predictors (u_f^n) have been utilized, the equations of motion have been linearized. Gauss-Seidel is then applied using successive over relaxation to iteratively solve the momentum equations (3.32), to find a predicted velocity for the value at time step $n+1$, this predicted velocity is generally denoted by $\hat{u}$.

$$\frac{\rho^{n+1}\hat{u}_i - \rho^n u_i^n}{\delta t} + \frac{1}{2\forall_{cv}} \sum_{facesofcv} [u_{i,f}^n + \hat{u}_{i,f}]g_N^{n+1/2}A_f =$$

$$\frac{1}{2\forall_{cv}} \sum_{facesofcv} \mu_f(\frac{\partial \hat{u}_{i,f}}{\partial x_j} + \frac{\partial u_{i,f}^n}{\partial x_j})A_f + F_i^n \tag{3.32}$$

This is why the fractional step method is called semi-implicit, the velocity field is not strictly predicted implicitly, but partially implicitly and partially based on projected values from explicit time steps. In equation (3.32), g_N is the normal momentum flux through a control volume face, so $g_N = \rho u_{f,N}$. In equation (3.32) F_i^n is the interphase momentum transport. At this point the old pressure gradient is removed from the velocity field in order to allow the freedom necessary to apply a corrector step, the enforcement of continuity.

$$\frac{\rho^{n+1}u_i^{n+1} - \rho^{n+1}\hat{u}_i}{\Delta t} = -\frac{\delta p^n}{\delta x_i} \tag{3.33}$$

$$\frac{\rho^{n+1}u_N^{n+1} - \rho^{n+1}\hat{u}_N}{\Delta t} = -\frac{\delta p^n}{\delta x_N} \tag{3.34}$$

With the old pressure removed the new pressure is determined by applying the incompressibility condition, that of a divergence free velocity field, to find an equation for the new pressure which is required to augment the velocity field such that it satisfies continuity. Once the pressure Poisson equation (3.35) is solved, the corrected u^{n+1} velocity can be calculated directly.

$$\frac{1}{\forall_{cv}} \sum_{facesofcv} \frac{\delta p}{\delta x_N} A_f \Delta t = \frac{1}{\forall_{cv}} \sum_{facesofcv} \rho_f^{n+1} \hat{u}_{i,f} A_f + \frac{\delta \rho}{\delta t} \qquad (3.35)$$

Chapter 4 – Particle-laden Channel Flow

As noted previously, extensive experimental and computational work has been done on bubble column reactor modeling. In the bubble column reactor it is noted that the disperse phase volume fraction is not dilute, and will exceed 0.01% for almost all cases. This leads to the assertion that perhaps these volume displacement forces are significant in other systems containing a high disperse phase volume fraction. One particular application where this can be important is pulverisezed coal fire power plants. If the volume displacement effects are important in these high particle to fluid density ratio systems, then the ability of Eulerian-Lagrangian models to properly predict fuel/oxygen mixing is highly dependent on properly simulating the local flow features in the vicinity of the particulates. In this case it is particularly important since the only fuel source is directly from the particle due to evaporation. If the local turbulent intensities are modeled as being too low, because these effects are being neglected, then the models will underpredict the reaction rates and thus, temperatures and efficiencies of the plants. This section will study one particular feature of a pulverised coal power plant, pneumatic transport of coal particles through a channel, which would occur on the way to the burner.

4.1 Problem Description and Setup

In this case a particle-laden channel flow is studied using large-eddy simulation. Designed after the work of Yamamoto et al. (2001) [30], this work investigates the effect of particle mass loadings and coupling method on this channel flow. In these cases, a high turbulent Reynolds number flow of 644, yielding a mean flow

Reynolds number of approximately 13,000 is simulated. Particle mass loadings for this study have a range varying from 0.01 to 5.
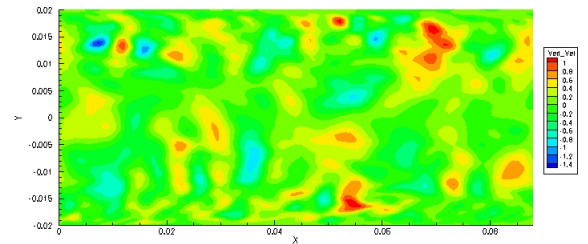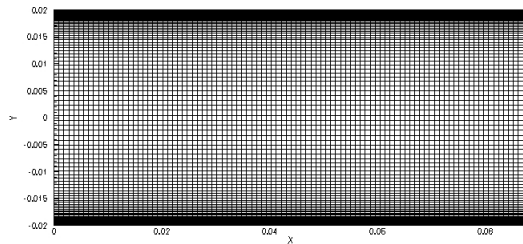
Figure 4.1: *Cross section of the turbulent channel flow mesh used in this work.*

Figure 4.2: *Instantaneous snapshot of a vertical gas phase velocity from a case in this work.*

A mesh cross section normal to the lateral ($\hat{z}$) direction is shown in figure 4.1. There is significant grid refinement in the wall normal direction in order to well resolve the wall layer. Periodic boundaries are used in the streamwise ($\hat{x}$) and lateral directions, with no-slip condition at the wall-surface. Particles were subject to a specular reflection condition at the walls. An instantaeous snapshot of the plane-normal vorticity profile is shown in figure 4.2 to demonstrate the turbulent nature of the channel. Other parameters used in this work are given in table 4.1.

The simulation was continued for several flow through times in order to achieve a fully developed gas velocity profile, at which point particle were injected and several more flow through times passed before fluid and particle statistics were collected. Flow properties such as streamwise momentum, wall-slip velocity and bulk flow rate are tracked to determine when the new particle-laden flow has become fully developed. In the studies of Yamamoto et al. [30] the channel

Table 4.1: Particle-laden Channel - Computational Parameters

Parameter	Value
Computational Domain	0.088 m x 0.04 m x 0.03 m
Fluid Viscosity (μ_f)	1.5 x 10^{-5} kg/ms
Fluid Density (ρ_f)	1.0 kg/m^3
Reynolds Number (Re_τ)	644
Mass Loading (m)	0.01 - 5.0
Stokes Number (St_p)	0.89 - 70

is forced using a constant pressure gradient (CPG) forcing method. With some knowledge of the expected flow field, the expected wall shear stress τ_w for example, the wall-slip velocity u_τ can be calculated.

$$u_\tau = \left(\frac{\tau_w}{\rho} \right)^{1/2} \tag{4.1}$$

In order to determine the appropriate forcing for the flow, it is required that the shear stress at the walls balance out the pressure driven forcing. A body force equal to the pressure gradient required to drive the channel is applied to the flow field. The necessary body force can be calculated using the equation below.

$$\text{(Domain Volume)} * b_x = \text{(Wall Surface Area)} * \tau_w \tag{4.2}$$

Thus in a pure gas flow the desired body force is derived directly. The extension to particle-laden flows however is more complicated. Following the method of Yamamoto et al. (2001), a correction factor may be added to the original balance equation to account for the effect of adding dense particles to the flow [30].

$$(\text{Domain Volume}) * b_x = (\text{Wall Surface Area}) * \tau_w + N m_p \overline{g} \qquad (4.3)$$

The presence of particles is now accounted for by adding in the force of N particles on the flow field. This works well for low mass loading cases and was used for some of these cases to compare results to those of [30], as well as to validate that the results were the consistent when a constant mass flow rate in the streamwise condition was enforced.

4.2   Validation of Work

In order to ensure our case conditions were handled properly, several tests runs were done to validate our results against the work of [30]. Validation cases were ran for all four major cases studied in [30], however only a sampling are shown here for brevity. In the lowest mass loading case, where $m = 0.01$, a collection of $28\mu m$ diameter particles with a density of $\rho_p = 700 \ kg/m^3$ were injected into the turbulent channel. These particles are meant to reflect the properties of lycopodium particles after the experiments of Kulick et al. (1994) [76]. Typical turbulent flow statistics such as mean flow rates and RMS velocities for both phases was computed and compared to existing data. Figure 4.3 compares the mean streamwise velocity profile as a function of wall normal distance for both fluid and particulate phases.

The first case that will be examined is the lowest mass loading (m) case, corresponding to a mass loading of $m = 0.01$. In this case 28 μm particles with a
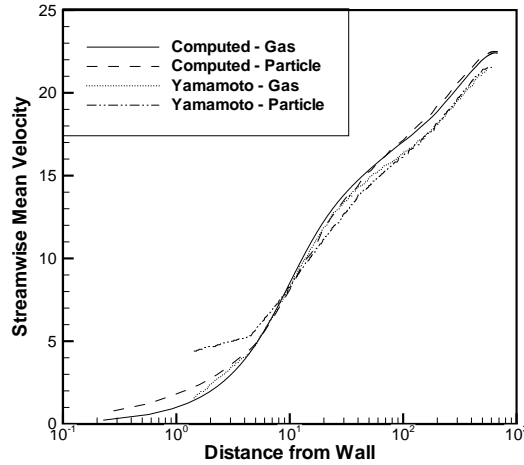
Figure 4.3: *Case 1: Mean Streamwise Gas and Particle Velocities*
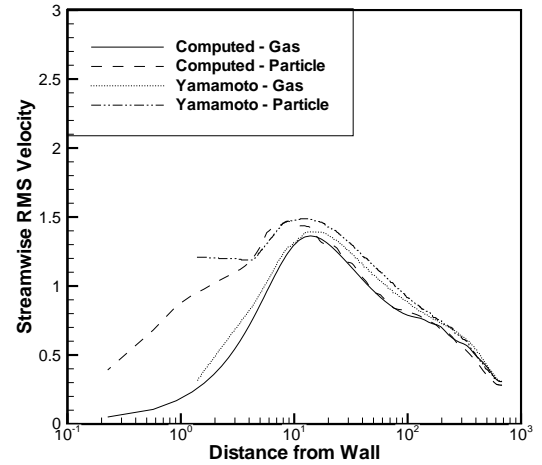
Figure 4.4: *Case 1: RMS Streamwise Gas and Particle Velocities*

density (ρ_p) of 700 kg/m^3, which corresponds to a Stokes number (St) of 0.89 for this flow, are injected into a fully developed single phase flow field to shorten the development time. These are the smallest Stokes number particles studied and as expected, their behavior very similarly to the carrier phase flow field is obtained. Figure 4.3 shows that there is a slight trend for the particles to have a faster streamwise velocity closer to the channel centerline than the fluid due to the effect of gravity on the particles, since their density is more than two orders of magnitude higher than that of the air. This effect is not pronounced and adds little energy to the particles and produces very little in the way of additional turbulent intensity, as can be seen in figure 4.4. The one deviation from this occurs near the wall where the particle velocities, both mean and RMS, are higher than that of the surrounding fluid. This is because the particles are not subject to the no-slip
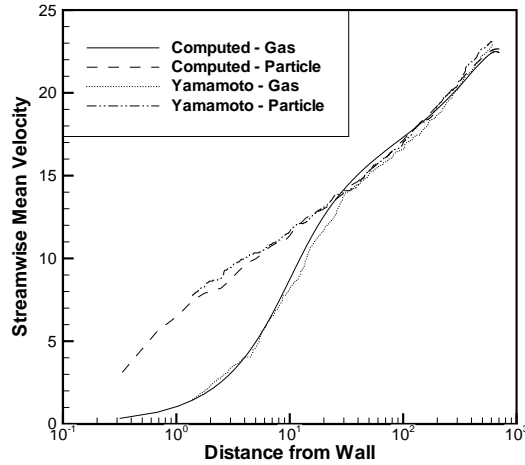
Figure 4.5: *Case 2: Mean Streamwise Gas and Particle Velocities*
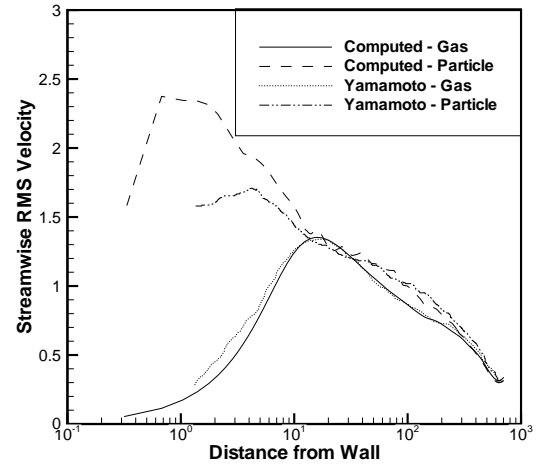
Figure 4.6: *Case 2: RMS Streamwise Gas and Particle Velocities*

condition and as such do not lose all their momentum near the wall. They do lose a substantial amount due to drag from the fluid phase as the fluid phase is much slower than the mean flow.

Similar trends can be seen in the second test case. In this case 50 μm particles with a density of 2500 kg/m^3 and a Stokes number of 10 are injected into the flow to yield a particle mass loading of 0.2. These particles are made to reflect the properties of glass beads. The main trends in this case are qualitatively the same as the trends in the previous case. The particles still generally reflect the mean flow characteristics but tend to deviate near the wall as is shown in figure 4.5. The particle RMS velocity near the wall, which is shown in figure 4.6 is most likely artificially enlarged in comparison with that of the established results due to an unphysically large repulsion force from the wall. The authors make no mention

of their method for handling particle-wall collision in the "collision-free" case, but it seems likely that they implemented an inelastic reflection condition of some sort. The difference in the handling of these properties can leads to significantly different near wall properties. Higher mass loadings and particle to fluid density ratios were also simulated, but the results here are sufficient to establish agreement with reputable published data.

4.3 Statistics

With the presently used code validated against relevant computational data, some results are analyzed to determine the role that volume displacement effects play in this system. For the purposes of this work, the results will focus on the case with a mass loading of $m = 1$ and injected particles with diameters of $70\mu m$ and densities of 8800 kg/m^3. The streamwise velocities of each phase are plotted in figure 4.7 with separate cases including and neglecting collisions. For the same cases figure 4.8 shows lateral RMS gas velocity profiles. It is clear that while accounting for collisions is important, the choice of coupling method between two-way and volumetric is not a primary concern for mean fluid statistics.
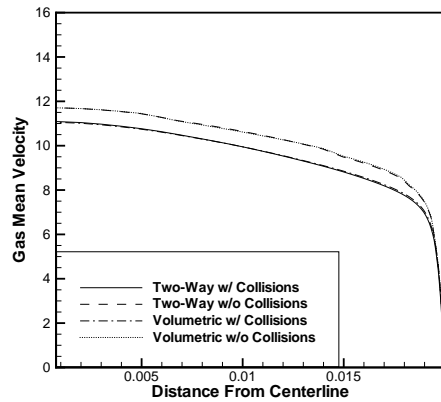
Figure 4.7: *Streamwise mean gas velocity for m = 1, with the coupling and collision method indicated in the legend.*
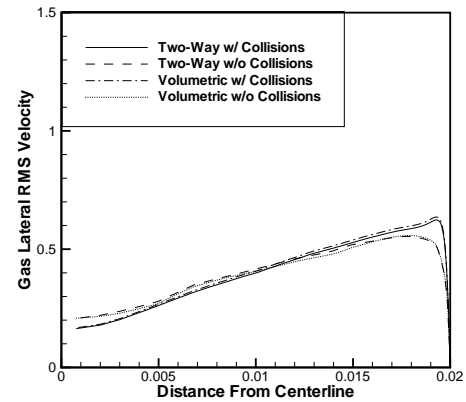
Figure 4.8: *Lateral RMS gas velocity for m = 1, with the coupling and collision method indicated in the legend.*

Wall-normal RMS particle velocities are plotted in figure 4.9 to demonstrate that these too are unaffected. The wall-normal particle volume fraction is plotted

in figure 4.10 to verify that the mean particle distributions also remain unchanged.
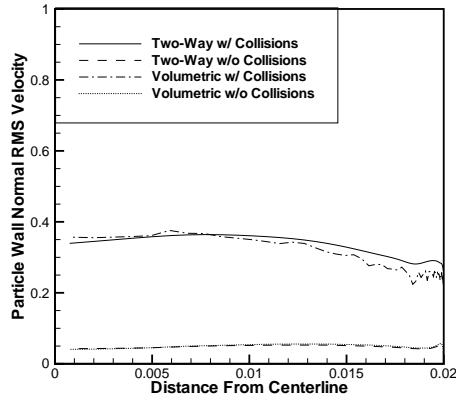
Figure 4.9: *Wall-normal RMS particle velocity for m = 1, with the coupling and collision method indicated in the legend.*
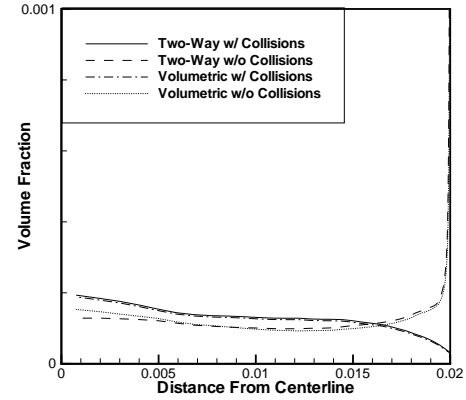
Figure 4.10: *Wall-normal volume fraction profile for m = 1, with the coupling and collision method indicated in the legend.*

With it established that the usual statistical measures of two-phase turbulent flow show no true indication of a difference between coupling methods, possible differences are sought using other measures.

4.4   Near Wall Structures

In some ways the near wall structures are what ultimately defines the characteristics of a turbulent wall-bounded flow. These structures are dependent on several things, including mass loading, flow rate and Reynolds number among others. Examining patterns in near wall structures and possible correlations with structures of particle positions provide another way in which the coupling method effects can be analyzed. The near wall region seems the most likely place for differences since the volume fraction is highest here for collision-free cases.
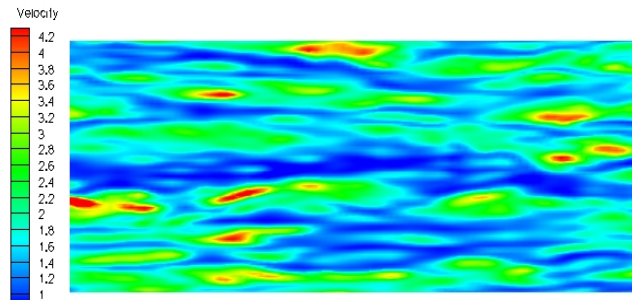
Figure 4.11: *Instantaneous gas velocity profile at a near wall plane corresponding to $y^+ = 4$ for the clean gas case ($m = 0$).*

In figure 4.11 we see the near wall streamwise velocity features. The near wall gas structures in figures 4.11 to 4.15 are taken at a wall normal distance of $y^+ = 4$, particle images are the collection of particles between $y^+ = 0$ and $y^+ = 4$. We can use 4.11 as a basis for comparison for the particle laden cases to see the effect of loading on the flows.
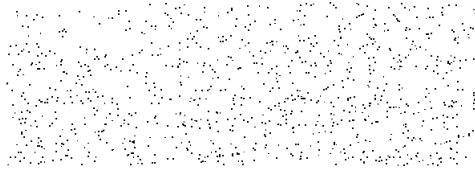
Figure 4.12: *Instantaneous particle structures in the near wall region $(0 < y^+ < 4)$ for the $m = 1$ case using two-way coupling and neglecting the effects of collisions, with $St = 70$.*
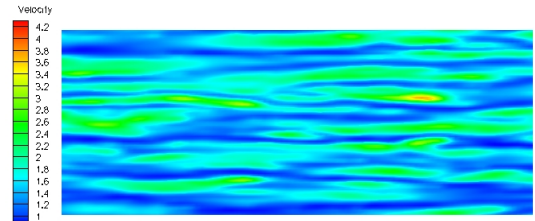
Figure 4.13: *Instantaneous gas velocity profile at a near wall plane corresponding to $y^+ = 4$ for the $m = 1$ case with two-way coupling and neglecting the effects of collisions, with $St = 70$.*

The particle structures shown in figures 4.12 and 4.14, for the cases when collisions are neglected, contain no real identifiable structure other than some streamwise streaking. This one snapshots suggests it may be more prevalent in the volumetric case, but some statistical analysis discussed in section 4.6 will demonstrate this is not true in general. The fluid phase velocity profiles also appear to have the same basic properties, suggesting the volume displacement effects are small here as well. Similarly, no defineable differences exist in particle profile observations for the cases with collisions, as shown in figures 4.16 and 4.18. Their respective fluid phases are shown in figures 4.17 and 4.19, and again there are no noteworthy differences.

The statistics of the preceeding section and the visualizations of this section were done for mass loadings ranging from 0.01 to 5 and Stokes number from less than 1 to 70. For this entire range the results were quite similar to those shown here.
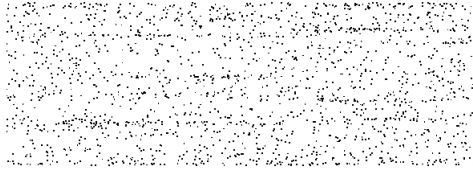
Figure 4.14: *Instantaneous particle struc-tures in the near wall region $(0 < y^+ < 4)$ for the $m = 1$ case using volumetric coupling and neglecting the effects of collisions, with $St = 70$.*
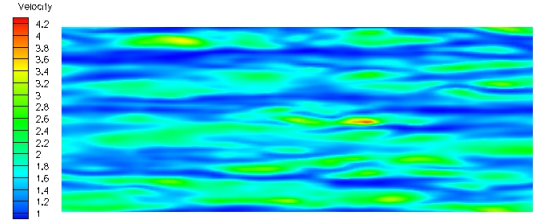
Figure 4.15: *Instantaneous gas velocity profile at a near wall plane corresponding to $y^+ = 4$ for the $m = 1$ case with volu-metric coupling and neglecting the effects of collisions, with $St = 70$.*
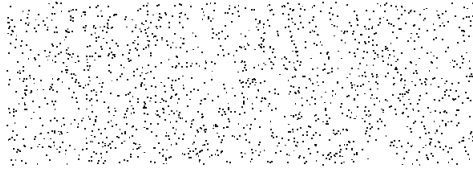
Figure 4.16: *Instantaneous particle struc-tures in the near wall region $(0 < y^+ < 4)$ for the $m = 1$ case using two-way coupling and including the effects of collisions, with $St = 70$.*
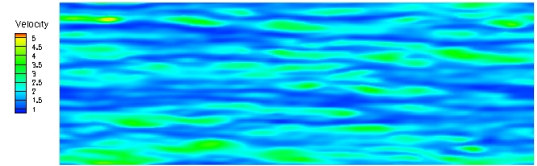
Figure 4.17: *Instantaneous gas velocity profile at a near wall plane corresponding to $y^+ = 4$ for the $m = 1$ case with two-way cou-pling and including the effects of collisions, with $St = 70$.*

4.5   Channel Centerline Particle Structures

Some of the most interesting patterns that form in particle-laden turbulent chan-nel are at the channel centerline, perpendicular to the walls. In figure 4.20 the structures formed by a collection of small Stokes number particles at the channel centerline is shown. The channel centerline particle profile will be briefly viewed here on the hopes of some noticeable difference based on coupling method.
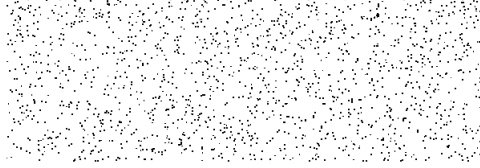
Figure 4.18: *Instantaneous particle structures in the near wall region $(0 < y^+ < 4)$ for the $m = 1$ case using volumetric coupling and including the effects of collisions, with $St = 70$.*
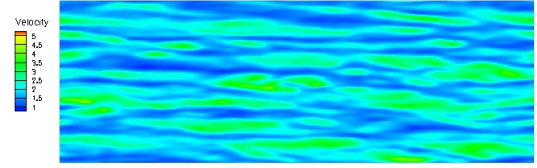
Figure 4.19: *Instantaneous gas velocity profile at a near wall plane corresponding to $y^+ = 4$ for the $m = 1$ case with volumetric coupling and including the effects of collisions, with $St = 70$.*
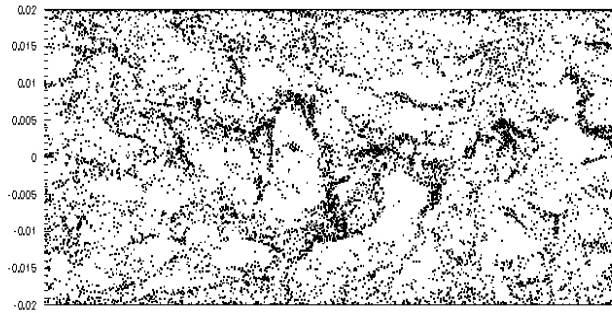
Figure 4.20: *Case 1: Wall Normal Streamwise Particle Structures $m = 0.01$, $d_p = 28\mu m$ - Volumetric Coupling*

In figures 4.21 and 4.22, particle profiles along the channel centerline are shown. While it may seem that perhaps a few more particle are present in the volumetric case on the right, there is otherwise no discernable difference between these images. Once again, this will be verified with two statistical measures in section 4.6.
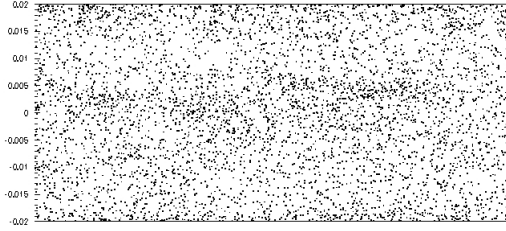
Figure 4.21: *Case 4: Wall Normal Stream-wise Particle Structures - Two Way coupling*
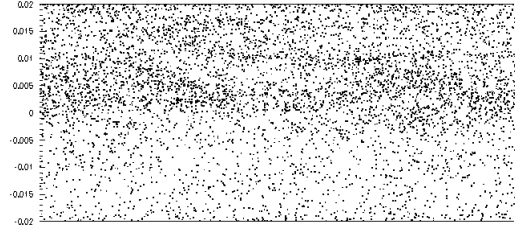
Figure 4.22: *Case 4: Wall Normal Stream-wise Particle Structures - Volumetric coupling*

4.6 Particle Clustering

In order to verify the previous observations, two statistical measures of particle clustering and dispersiveness are computed here. One method of classifying particle clustering is known as the PDF method, or probability density function method. In this method the domain is split into small bins of equal size, the number of particles in each bin are tallied and a probability density function is built for the number of particles per bin. In general this function is most appropriately compared to the Poisson distribution, which represents the PDF that would result from applying this same technique to a purely random group of particles. Particle distributions closer to the Poisson distribution indicate a random distribution of particles in the domain. There are a few variations of this theme used here to analyze particle clustering in these flows. The global distribution refers to the entire domain as the subject of a single PDF, as such as regions within the flow are meshed together, it is not clear that this is an entirely accurate view of particle clustering since two different types of clustering can in effect cancel each other. The deviation from

the Poisson distribution gives a degree of variation from random.

$$\hat{D}_g = \sum_{n=1}^{\infty} [f_B(n) - f_P]^2 \tag{4.4}$$

In order to obtain more information about spatially non-uniform clustering features the domain is split, in two separate calculations, into slices in the wall normal and lateral direction. The hope is that by slicing the domain in the wall normal direction, any clustering features that are unique to the near wall area will be identified, as well as features unique to the channel centerline. Both of these sets of results are discussed for the cases with a mass loading of 0.01 and 1.

The Poisson distribution is calculated using equation 4.5, where λ is the average number of particles per cell and n is the number of particles that the given probability is being calculated for. A measure of clustering that can be calculated for this type of particle-laden flow is the deviation of the number density from that of a random distribution, $\hat{D}_g$, which is the deviation over the entire domain [77]. Calculated for each individual slice, $\hat{D}_{wn}$ is the deviation over each wall normal slice averaged and $\hat{D}_{zp}$ is averaged over each lateral slice. A second measure of the deviation is calculated by dividing the difference between the standard deviation of the actual distribution and the standard deviation of the Poisson distribution by the average number of particles per bin and is denoted by d_g [78]. The same averaging techniques are applied to find d_{wn} and d_{zp}.

$$f_P(n) = \frac{e^{\lambda}}{n!} \lambda^n \tag{4.5}$$

Table 4.2: Clustering Measurements ($m = 0.01$, $St = 0.89$)

Case	$\hat{D}_g$	$\hat{D}_{wn}$	$\hat{D}_{zp}$	d_g	d_{wn}	d_{zp}
Two-Way w/o Collisions	0.049	0.0437	0.0449	0.626	0.548	0.580
Two-Way w/ Collisions	0.058	0.0501	0.0471	0.702	0.601	0.664
Volumetric w/o Collisions	0.051	0.0444	0.0458	0.632	0.573	0.591
Volumetric w/ Collisions	0.057	0.0596	0.0468	0.705	0.645	0.662

Table 4.3: Clustering Measurements ($m = 1.0$, $St = 70$)

Case	$\hat{D}_g$	$\hat{D}_{wn}$	$\hat{D}_{zp}$	d_g	d_{wn}	d_{zp}
Two-Way w/o Collisions	0.024	0.0074	0.0422	0.4854	0.1220	0.4333
Two-Way w/ Collisions	0.0095	0.0078	0.0307	0.2072	0.1283	0.1583
Volumetric w/o Collisions	0.0238	0.0118	0.0427	0.4287	0.1529	0.3778
Volumetric w/ Collisions	0.0088	0.0128	0.0302	0.2015	0.1625	0.1520

Another way to classify clustering is the use of a particle radial distribution function. When doing this the RDF, or radial distribution function, is calculated by finding the distance between each pair of particles in the domain and placing them into bins of distances from the original particle. The number obtained from doing this is divided by the number of particles that would be expected in each bin if the particles were to be distributed either uniformly or randomly throughout the domain, in this case a uniform distribution was used. This tool is generally used in isotropic turbulence because the lack of a preferential direction yields more interesting results.
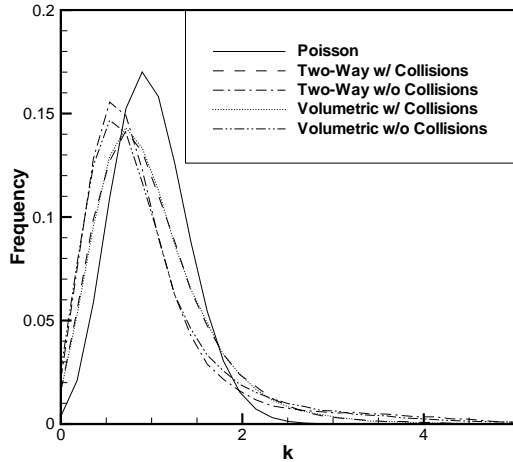
Figure 4.23: *PDF of particle number density over the entire domain plotted against the Poisson distribution for the case when $m = 1$ and $St = 70$. The inclusion of collisions and the coupling method are indicated in the legend.*
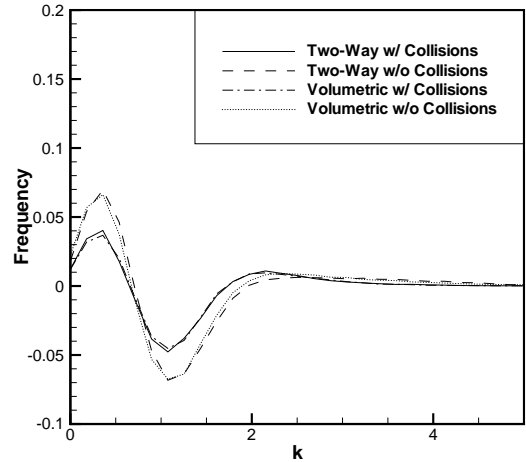
Figure 4.24: *Difference between Poisson distribution and actual distribution of particle number density over the entire domain for the case when $m = 1$ and $St = 70$. The inclusion of collisions and the coupling method are indicated in the legend.*

Table 4.2 shows several measures of the deviation for the case where $m = 0.01$. The calculated values show little to no deviation between two-way and volumetric coupling. The differences seen in the applicable figures are well represented here as seen by the differences between the cases ran with and without coupling.

The same results are presented for the case with a mass loading of 1. The global PDF is plotted with the Poisson distribution in figure 4.23 and the difference from the Poisson distribution in 4.24. This case has a mass loading a full $100\times$ higher than the previous, however, globally the same trend exists. The coupling method has an insignificant effect on the particle structure but the collision model drastically changes the distribution profile.
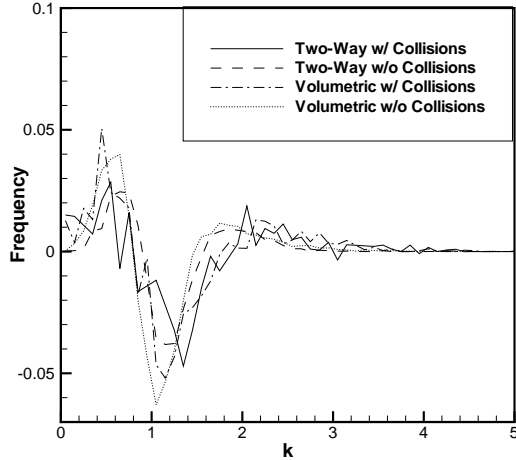
Figure 4.25: *Average difference between Poisson distribution and actual distribution of particle number density in a near wall slice with a thickness of one twentieth of the channel width for the case when $m = 1$ and $St = 70$. The inclusion of collisions and the coupling method are indicated in the legend.*
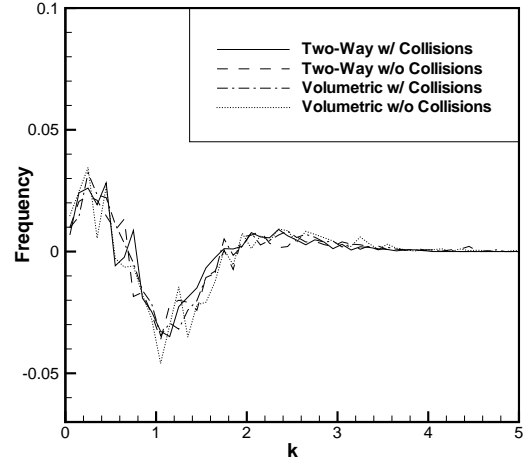
Figure 4.26: *Average difference between Poisson distribution and actual distribution of particle number density in a slice taken halfway between the wall and the channel centerplane for the case when $m = 1$ and $St = 70$. The inclusion of collisions and the coupling method are indicated in the legend.*

Even though the global PDF distribution appears to show no sizable difference it is important to see if theres any differences locally. It is possible that volumetric effects alter the clustering in the near wall region compared to near the channel center. Figure 4.25 shows the near wall region PDF for the case with a mass loading of one. The coupling method again shows no difference at a mass loading of one in the near wall region. The quarter-width PDF is shown in figure 4.26 with the same result.

The features shown in figure 4.6 are not particularly interesting for two reasons. One is that the scope of the distance is limited by the wall-normal directional
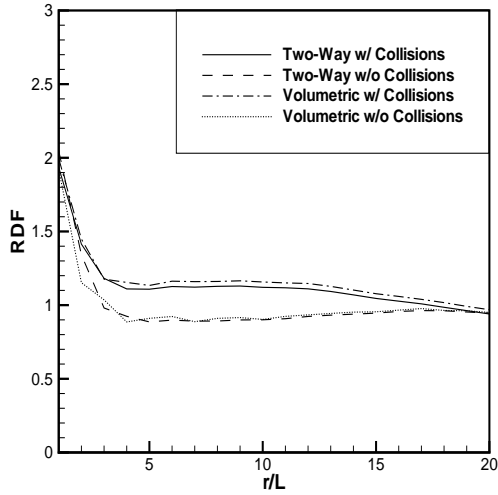
Figure 4.27: *Particle radial distribution functions for the indicated coupling method and collision effect for the case where $m = 1$ and $St = 70$.*

limitations. The second reason is that once again little to no difference is found between the coupling methods, however a moderate difference is found when the collision model is employed.

4.7   Summary of Channel Flow Cases

This section has demonstrated that having a high mass or moderate volume fraction loading is not a sufficient condition for having volume displacement effects become important, even in the near wall region where the volume fractions can become significant. This was demonstrated by comparing the mean fluid and particle velocities, the RMS velocities of both phases, visualizing near wall and channel centerline profiles, as well as computing several statistical measures. This suggests that the strength of volume displacement effects may not be entirely volume fraction dependent, but also are predominantly dependent on some other quantity, such as Stokes number or particle to fluid density ratio. To follow through with this hypothesis a case with a small bubble to fluid density ratio is examined next in detail.

Chapter 5 – Bubble-laden Vortex Ring

5.1 Problem Description

A traveling vortex ring, shown in figure 5.1(a), is generated through an inlet veloc-ity pulse [4, 35]. As the inlet pulse flows, it forms a shear layer, which rolls up into a vortex ring that is convected downstream. At $0.5m$ downstream from the inlet, the vortex ring is fully developed, at which point bubbles are injected individually every $10ms$ just in front of and below the bottom portion of the ring. The bubbles then begin the entrainment process, in which they circle the lowest portion of the ring to arrive in front of the vortex core center, as shown in figure 5.1(b). Once the entrainment process is complete, the bubbles tend to settle around a mean lo-cation, referred to as the bubble settling location with coordinates (r_s, θ_s) defined with respect to the core center. At the settling location the forces on the bubble are nearly in balance, i.e. sum close to zero in each direction. The force balance on the bubbles at a radial settling location from the core, shown in figure 5.1(c), indicates a balance of the pressure, added mass, lift and gravity forces [4, 35, 56]. Likewise, the angle of the settling location results from a balance between the buoyancy and drag forces. As the bubbles entrain and settle their presence forces an alteration of the local flow field, which can result in significant observable distortion. If this distortion becomes significant the bubbles tend to leave the plane of injection and escape laterally along the vortex core center, see figure 5.1(d). Once the bubbles escape the plane of injection, the vortex ring along this plane slowly begins to repair itself back to a structure similar to its pre-bubble entrainment form. Using this system as a model problem, volume displacement effects will be shown to be
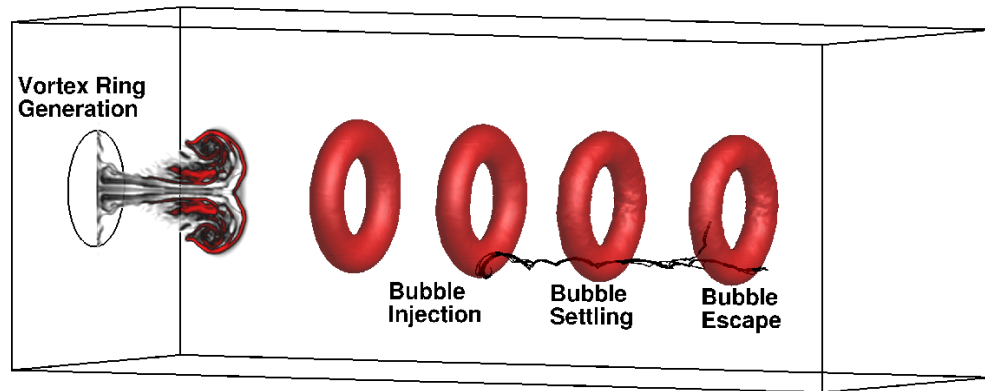
(a)
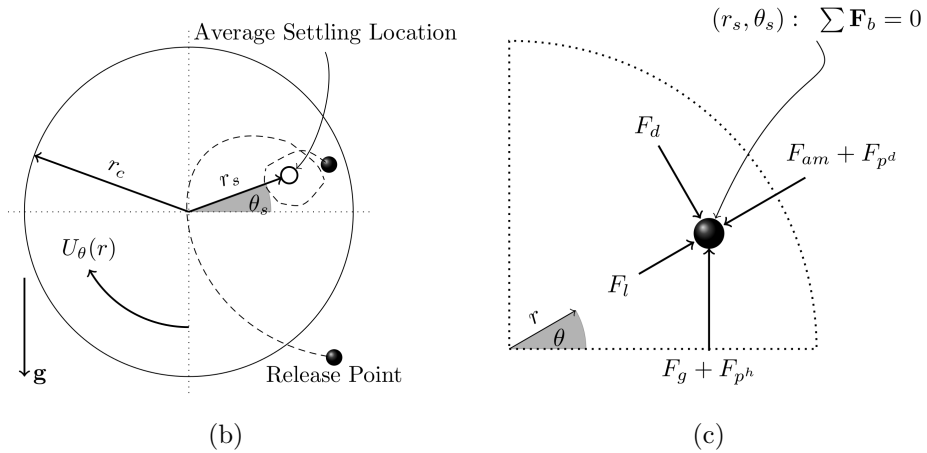
(b)

(c)
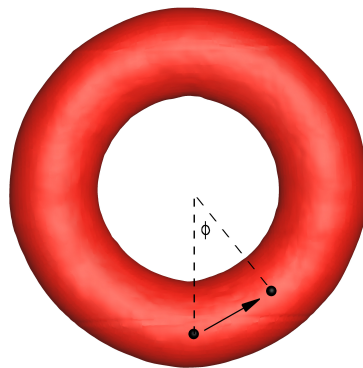
(d)

Figure 5.1: Bubble entrainment and escape process in a traveling vortex ring created by an inlet pulse that rolls up and propagates downstream: (a) bubble injection location and motion relative to the vortex core, (b) settling location (r_s, θ_s) and a typical trajectory of bubbles in cylindrical co-ordinates, (c) mean force balance occurring at the settled location, and (d) bubble escape path along the center of the vortex core, measured as an angle ϕ on either side from the plane of bubble injection.

significant even for very dilute volume loadings. These effects will be measured and their influence on the carrier phase analyzed.

The rest of the chapter is arranged as follows. The simulation setup is described in section 5.2. Section 5.3 discusses the behavior of both phases, showing agreement with experimental data. Quantification of vortex distortion, bubble escape and their effects on the forces on the bubbles are presented in section 5.4. Various techniques quantifying and analyzing the volumetric coupling effects are presented in section 5.5. A summary of the results and conclusions for the vortex ring cases are given in section 7.

5.2   Simulation Setup

The vortex ring is generated within a rectangular box of dimensions $0.8m \times 0.3m \times 0.3m$ in the streamwise ($\hat{x}$), vertical ($\hat{y}$) and lateral ($\hat{z}$) directions, respectively. This domain size was found to be sufficient based on previous two-dimensional studies [79, 35] and provides appropriate amount of field of view for bubbles to get entrained within the ring and influence the ring after settling. In addition, it was verified that further increase in the domain size does not alter the vortex ring structure or its propagation.

The inlet pipe section is of radius $0.05m$ and centered around the $x = 0$ plane, that injects a pulse of fluid generating the vortex ring, is captured by using a simple Cartesian grid. This was found to give clean generation of the vortex ring as opposed to use of tetrahedral unstructured grids. A Cartesian grid, $800 \times 241 \times 241$

is utilized in this work. Cell spacing is coarse in the corners and dense in the center to resolve the inlet section as well as the region of interest accurately. For studying vortex ring formation Mohseni et al. (2001) [80] used a grid resolution of $1/25^{th}$ of the inlet radius to achieve grid convergence. The finest grid used in this study has even finer spacing of $1/50^{th}$ of the inlet radius in order to resolve the inlet ring generation accurately. Several grid resolutions were studied to ensure proper vortex behavior. This was monitored by computing the vortex ring evolution and its strength decay from the inlet to the exit. With the fine grid resolution used in this study, the vortex ring propagates for the length of the numerical experiment with minimal dissipation of the vortex strength, in line with experimental observations. The time step was kept constant at $\Delta t = 0.001s$ in order to accurately capture the temporal evolution of the vortex ring and bubble dynamics. The inlet velocity profile (see figure 5.2) is assigned through a polynomial interpolation of the experimental profile, see Finn et al. (2011) [35] for details. The inlet condition is handled as a velocity source, which accurately represents the experimental piston inlet profile of the experiments [81]. In order to achieve the three different strengths of vortex rings studied in this work, the cylindrical slug model of Glezer (1988) [82] is used to match the experimental data. The vortex strength, Γ_0, is computed as shown in equation 5.1, with it's associated vortex Reynolds number (Re_{vx}) in equation 5.2.
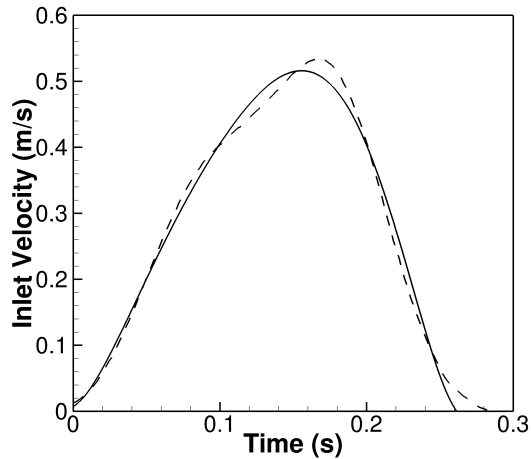
Figure 5.2: Inlet velocity profile used for generating the vortex ring: (—) present work, (---) experimental data of [4].

$$\Gamma_0 = \int_0^T \frac{u_0^2(t)}{2}dt = 0.0159;\ 0.0207;\ 0.0254\ m^2/s \qquad (5.1)$$

$$Re_{vx} = \frac{1}{2\nu_\ell} \int_0^T u_0^2(t)dt = 15900;\ 20700;\ 25400 \qquad (5.2)$$

The inlet velocity profile is scaled by a constant value for the three different vortex strengths. The weakest of the three strengths, $\Gamma_0 = 0.0159m^2/s$, constitutes a transitional vortex, while the two stronger vortices can be classified as turbulent based on Glezer (1988) [82]. As the liquid enters into the ambient domain, a shear layer forms that rolls up to create a vortex ring that strengthens as the inlet pulse dissipates. The generated traveling vortex ring propagates to the end of the domain. The ring maintains a consistent structure during the entire path of its motion. The core propagation speeds, averaged over the entire time of the

Table 5.1: Parameter variations for traveling vortex ring cases. Here Γ_0 is the vortex strength, r_b is bubble radius, r_c is vortex core radius, St_b is the bubble Stokes number, Δ_{cv} is the local grid resolution, VF is the volume loading.

Case #	$\Gamma_0(m^2/s)$	$2r_b(\mu m)$	St_b	$gr_b^3/\Gamma_0^2(\times 10^6)$	r_b/r_c	$2r_b/\Delta_{\mathrm{cv}}$	$VF(\times 10^4)$
1	0.0159	300	0.09	0.13	0.013	0.21	0.11
2	0.0159	500	0.27	0.61	0.022	0.35	0.51
3	0.0159	700	0.53	1.66	0.031	0.50	1.39
4	0.0159	900	0.87	3.54	0.039	0.65	2.96
5	0.0159	1100	1.30	6.46	0.048	0.79	5.42
6	0.0159	1300	1.81	10.66	0.057	0.93	8.94
7	0.0207	700	0.68	0.98	0.031	0.50	1.39
8	0.0254	500	0.43	0.24	0.022	0.35	0.51
9	0.0254	700	0.84	0.60	0.031	0.50	1.39
10	0.0254	900	1.39	1.39	0.039	0.65	2.96
11	0.0254	1100	2.07	2.53	0.048	0.79	5.42
12	0.0254	1300	2.89	4.18	0.057	0.93	8.94

simulation, are 0.11, 0.16 and 0.19 m/s for the three strengths, respectively. The vortex ring formed from this process is symmetric, as plotted in figure 5.1(a) based on the computed flow.

Table 5.1 lists the various cases studied in this work, similar to those studied in [4, 35]. Three different vortex strengths, weak ($\Gamma_0 = 0.0159m^2/s$), medium ($0.0207m^2/s$) and strong ($0.0254m^2/s$), are used for generating the traveling vortex ring. A wide range of bubble diameters (300-1300 μm) are injected to study their effect on the vortex. For the cases studied, the ratio of bubble diameter to grid resolution, $2r_b/\Delta_{\mathrm{cv}}$, is less than one and ranges between 0.21-0.93. The volume loading of the disperse phase is based on only the region of the vortex core where bubbles are present, not on the entire domain, but is still very small.

Let the vortex core radius, r_c, be the length scale, the velocity at the settling location, $U_{\rm rel} = \Gamma_0 r_s/2\pi r_c^2$, be the velocity scale, and hence $2\pi r_c^2/\Gamma_0$ is the time scale, and $\rho_\ell r_s \Gamma_0^2/4\pi^2 r_c^4$ is the local pressure gradient scale at the bubble settling location for the flow structure in a vortex ring. Then, the following non-dimensional groups can be obtained for the bubble dynamics and bubble settling location [4],

$$\bar{r}_s = r_s/r_c; \quad \bar{r}_b = r_b/r_c; \quad \bar{g} = gr_c^3/\Gamma_0^2; \quad \text{and} \quad Re_{vx} = \Gamma_0/\nu_\ell, \qquad (5.3)$$

where $\bar{r}_s$ is the non-dimensional settling location, $\bar{r}_b$ is the non-dimensional bubble radius, $\bar{g}$ is non-dimensional gravity force, and Re_{vx} is the vortex Reynolds number. The non-dimensional gravity force is proportional to the ratio of the weight of the fluid in the vortex core to the integrated pressure gradient in the core. In the present cases, the vortex core size (r_c) remains roughly constant for all cases and is much larger than the bubble size (r_b). Then $\bar{r}_b$ and $\bar{g}$ can be combined to form a non-dimensional group (gr_b^3/Γ_0^2), that becomes the ratio of the buoyancy force on the bubble to the hydrodynamic pressure gradient force. The non-dimensional settling location $(\bar{r}_s)$ is then a function of the gravity parameter $(\bar{g}\bar{r}_b^3)$ and the vortex Reynolds number. The Reynolds number dependence mainly comes through the drag and lift coefficients, which can depend on the bubble size and bubble (or vortex) Reynolds number.

Likewise, $\bar{r}_b$ and Re_{vx} can be combined to obtain the bubble Stokes number,

$$St_b = (\overline{\omega}) \left(\frac{\rho_b d_b^2}{36\mu_\ell} \right) = \left(\frac{\Gamma_0}{\pi r_c^2} \right) \left(\frac{\rho_b d_b^2}{36\mu_\ell} \right) = \frac{1}{9\pi} \frac{\rho_b}{\rho_\ell} \bar{r}_b^2 Re_{vx} = \frac{1}{9} \frac{\rho_b}{\rho_\ell} \frac{\bar{r}_b}{\bar{r}_s} Re_b^{ref}, \qquad (5.4)$$

where $Re_b^{ref} = U_{\text{rel}}d_b/\nu_\ell$ is the reference bubble Reynolds number based on the bubble diameter. Bubble Stokes numbers range from 0.09 to 2.89, with three different vortex strengths. Sridhar & Katz (1999) [4] argued that the bubble Reynolds number varies over a small range $20 < Re_b^{ref} < 80$ for the given Stokes number range, whereas the gravity-based parameter $(\bar{g}\bar{r}_b^3)$ varies by two-orders of magnitude for the cases studied (see table 5.1) and assumed that the settling location is only a weak function of the Reynolds number.

5.3   Bubble Behavior and Vortex Distortion

The vortex ring is allowed to develop until it reaches $0.5m$ downstream of the injection plane. The position of the vortex ring is tracked by finding the weighted center of vorticity on the plane of bubble injection (the lowest two-dimensional slice of the core) with coordinates (X_c, Y_c), which are calculated as:

$$X_c = \sum_i X_i\omega_i^2 \Big/ \sum_i \omega_i^2 \;\; ; \;\; Y_c = \sum_i Y_i\omega_i^2 \Big/ \sum_i \omega_i^2. \tag{5.5}$$

In a perfectly symmetric vortex, the core center would be at the point of zero velocity relative to the motion of the structure. In the bubble-free case this is close but not exactly true, as the core has a slight asymmetry due to its traveling nature and turbulent features. In the bubble-laden cases, however, the two points of zero velocity and the weighted center of vorticity, may not be in close proximity owing to core fragmentation and asymmetry of the vortex core. When the vortex ring
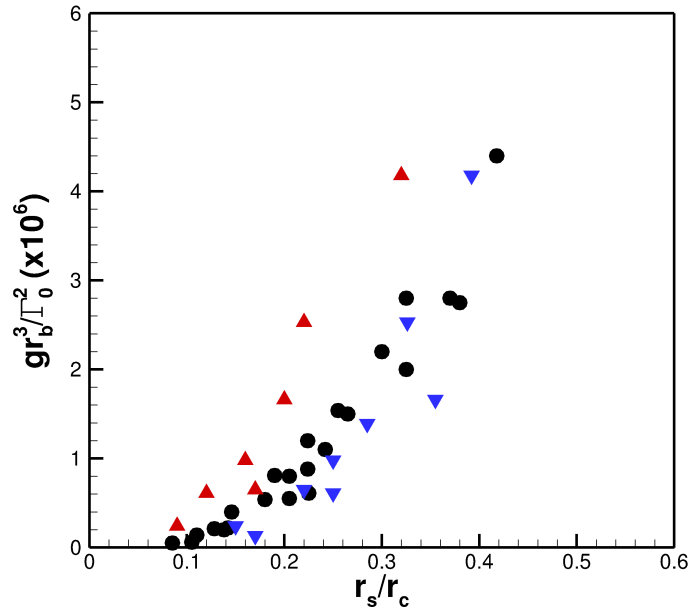
Figure 5.3: Ratio of buoyancy force to hydrodynamic pressure gradient versus the non-dimensional bubble settling location: ($\blacktriangle$) two-way coupling, ($\blacktriangledown$) volumetric coupling, ($\bullet$) experimental data of [4].

reaches $0.5m$, the bubbles are released in front of and below the core in the $z = 0$ plane containing part of the vortex ring, as shown in figure 5.1(a). Eight bubbles are injected individually every $10ms$. Each bubble is injected, then entrained separately. Although each bubble entrains at a different time, each follows very similar paths initially.

Figure 5.3 plots the gravity parameter (gr_b^3/Γ_0^2) versus the non-dimensional bubble settling locations $(\bar{r}_s)$ for the cases studied, where $\bar{r}_s$ is the average position of the bubbles after entrainment into the first quadrant of the vortex. Predictions based on two-way and volumetric coupling formulations are compared with the

experimental data of [4]. It is observed that both formulations predict the basic trend that as the ratio of the buoyancy to the pressure gradient is increased the bubbles settle further away from the vortex center. Similarly, for same size bubbles, increase in the vortex strength results in settling locations closer to the vortex core. The surface forces such as drag and lift are proportional to r_b^2, whereas the buoyancy, the added mass and pressure gradient forces are proportional to r_b^3. The variability in the settling location with respect to the force ratio, gr_b^3/Γ_0^2, is attributed to the dimensional analysis process neglecting the dependence on the vortex Reynolds number. It is also observed that the two-way coupling formulation tends to under-predict the settling location for the entire range of buoyancy to hydrodynamic pressure gradient ratios, with the error between the predicted location and the actual location being proportional to bubble size. The volumetric coupling formulation, however, provides better agreement with experimental results. It will be shown later that the fluid displacement effects present in the volumetric coupling formulation, are critical in affecting the distribution of vorticity within the vortex core for bubbles that settle beyond $r_s/r_c > 0.2$, whereas, the two-way coupling formulation showed negligible effect on vorticity distribution. It is also shown that the fluid displacement effects, expressed as an equivalent momentum coupling force (equation 5.13), show dependence on the vortex Reynolds number (Γ_0/ν_ℓ).

Bubble trajectories relative to the vortex core center are shown in figure 5.4 for the weak as well as strong vortex cases with two representative bubble sizes. The coordinate system used to describe the bubble settling locations is shown in
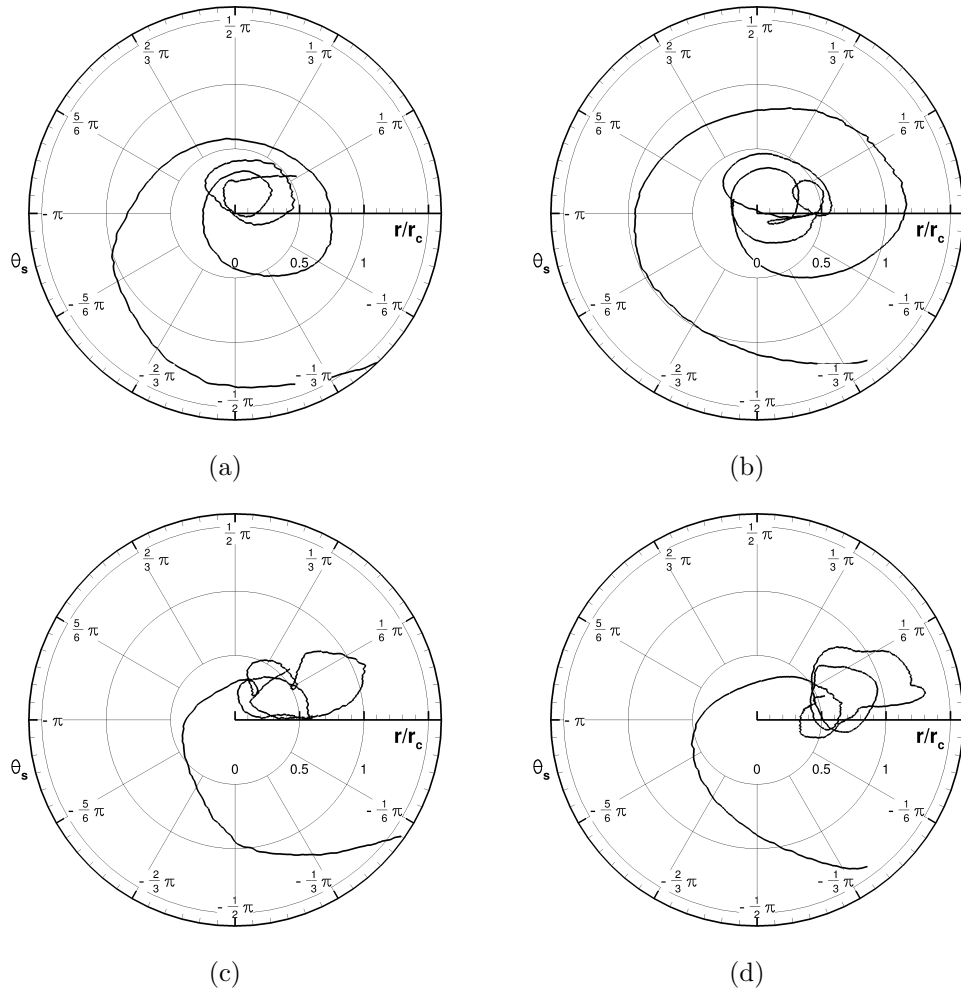
Figure 5.4: Bubble trajectories and settling locations relative to the vortex core center: strong vortex cases (a) $d_b = 500$ μm (case # 8), (c) $d_b = 900$ μm (case # 10); and weak vortex cases (b) $300 \mu m$ (case #1), and (f) $1100 \mu m$ (case #5) .

figure 5.1(b). The relative bubble positions are computed as $\mathbf{x}_{rel} = \mathbf{x}_b - \mathbf{X}_c$, then converted to cylindrical coordinates and plotted as (r_{rel}, θ_{rel}) on the plane of bubble injection, so (0,0) is the core center as computed in equation 5.5. The differences in entrainment time and trajectories amongst the cases are easily noticeable. Large bubbles tend to take a more direct path to their settling location, whereas smaller bubbles take a longer route. For the present three-dimensional vortex ring studies, the bubbles do not completely settle but tend to move in a small circular path around a mean settling location, owing to the unsteadiness in the flow as well as the three-dimensional nature of the ring. For the weak vortex cases, large bubbles tend to show considerable volatility in settling position after they are entrained.

Owing to the three-dimensional, transitional flow within the vortex ring, the bubbles do not perfectly remain in the plane of injection for the entire duration of the simulation. After achieving a mean settling location in the plane of injection, the bubbles drifted from this plane as the vortex ring travelled downstream. This behavior of the bubbles is referred to as *bubble escape* and shown is schematically in figure 5.1(d). Note that only minimal escape of the bubbles was obtained with two-way coupling computations, whereas significant escape is observed in some cases with volumetric coupling.

In the vortex ring, bubbles escape to both sides of the plane of injection, however, for the sake of quantifying escape, the absolute value of the lateral ($\hat{z}$) component of their position is used in averaging their position along the core. This position is plotted at the end of simulation, i.e. when $X_c = 0.65m$. It is observed that bubble escape is smaller for stronger vortex strength, whereas with weaker
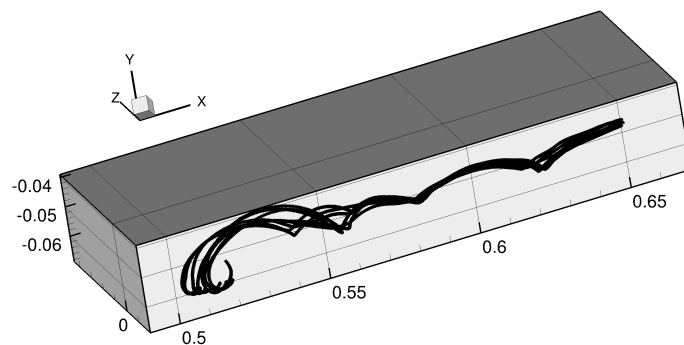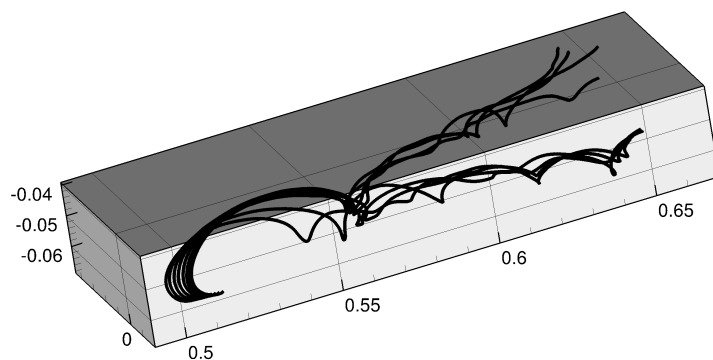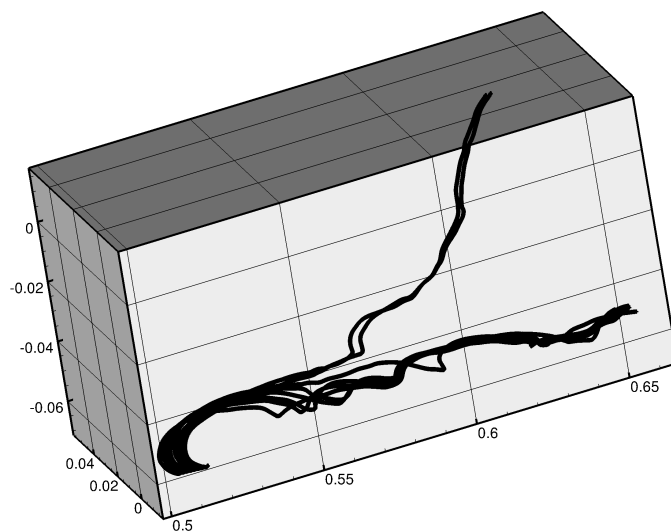
Figure 5.5: Paths traversed by bubbles within a vortex ring showing bubble escape: (a) marginal escape for strong vortex case # 8 ($d_b = 500\mu m$), (b) moderate escape for weak vortex case # 3 ($d_b = 700\mu m$), and (c) significant escape for weak vortex case # 5 ($d_b = 1100\mu m$).

vortex ring the bubbles tend to escape more. The amount of bubble escape (i.e angle ϕ from the plane of injection) changes with time. Figure 5.5 shows the escape trajectories of eight bubbles for representative strong and weak vortex strengths. For the strong vortex case (#8), all eight bubbles stay relatively close together as they move downstream in the flow direction (x direction) and do not veer to either side of the vortex ring, showing minimal bubble escape. For the weak vortex case with $700\mu m$ bubbles (case # 3), the bubbles show moderate escape that increases as they travel downstream along with the vortex ring. Case #5 with large bubbles ($1100\mu m$) shows significant escape, to an extent that the bubbles are no longer entrained into the vortex core at later times, but are still contained within the upper portions of the ring. As the bubbles escape from the injection plane, the vortex ring was found to begin to repair itself back to a structure similar to its structure, pre-bubble entrainment. This is found to be related to the variations in local bubble concentrations and hence the fluid displacement effects as discussed later.

Figure 5.6 shows the temporal evolution of the out-of-plane vorticity contours plotted in the moving cylindrical frame for unladen as well as bubble-laden cases for the weak vortex strength of $\Gamma_0 = 0.0159 m^2/s$. The transitional nature of the vortex ring is evident. For the unladen case (as well as bubble-laden case computed using a two-way coupling reaction point-source), a strong vortex core is observed (seen as the red spot at the center) and remains mostly unaltered over the duration of the simulation. Figure 5.6 also shows time-evolution of the vortex ring when eight bubbles are entrained, obtained using the volumetric coupling formulation, in

(a) x = 0.5m   (b) x = 0.5m

(c) x = 0.55m   (d) x = 0.55m

(e) x = 0.6m   (f) x = 0.6m

(g) x = 0.65m   (h) x = 0.65m
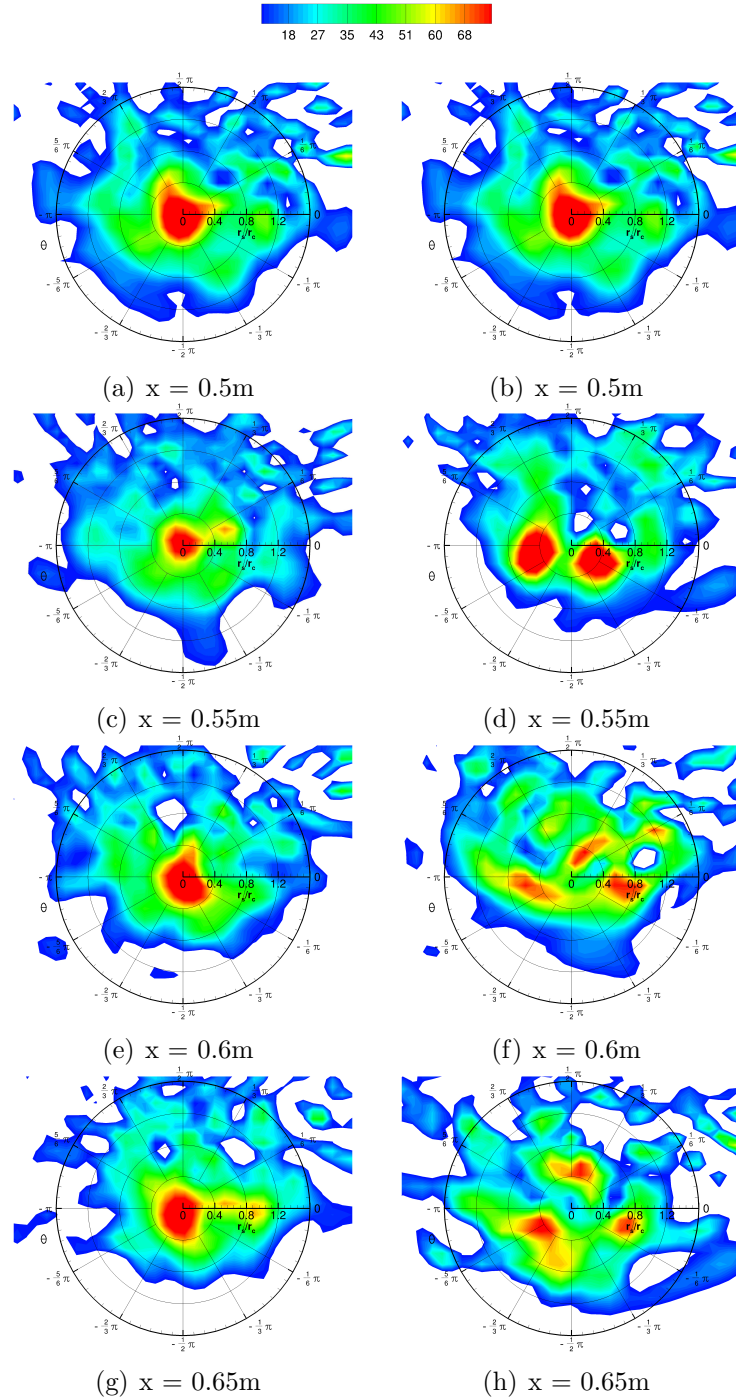
Figure 5.6: Temporal evolution of the out-of-plane vorticity in cylindrical co-ordinates for the weak vortex case #3, $\Gamma_0 = 0.0159 m^2/s$: left column (a),(c),(e),(g) are for the unladen case; right column (b),(d),(f),(h) are when eight bubbles of $d_b = 700\mu m$ are entrained. The time difference between each plot is approximately $0.4s$. The vorticity field has been filtered below $\omega_z < 10$ to show the high degree of distortion and core fragmentation.

comparison with the corresponding unladen case. The four visualizations roughly correspond to positions of the vortex ring at which the bubbles are injected ($x = 0.5m$), entrained ($x = 0.55m$), settled ($x = 0.6m$), and escaped in the $\hat{z}$ direction ($x = 0.65m$). Before bubble injection, the vorticity profile consists of mainly concentric iso-vorticity contours, as shown in figure 5.6a,b. As the bubbles are injected and they become entrained into the ring, they begin to alter the vortex structure.

As the bubble is entrained and passes through close to the vortex center ($x = 0.55m$, figure 5.6(d)), it splits the high vorticity region into smaller regions. Settled bubbles cause significant distortion in the vortex structure (figure 5.6(f), 5.6(h)), not just in the local region of bubble motion, but within the entire core radius ($r_c = 0.01145m$), an observation similar to the experimental data. The vortex core radius is the same as utilized in the experimental studies.

The volume displacement effects present in the volumetric coupling cases were found to be important in predicting this behavior. As is discussed later, this process of vortex core fragmentation was not observed using standard two-way coupling approaches even with presence of bubbles. With two-way coupling, the vortex structure is very similar to the unladen case, indicating that the point-source momentum coupling alone is insufficient to affect the vorticity distribution within the core.

Figure 5.7 shows bubble escape characterized by the angle ϕ from the plane of injection and obtained by averaging over all bubbles in the vortex ring at $x = 0.65m$, close to the end of the simulations. The scatter in radial distance from the
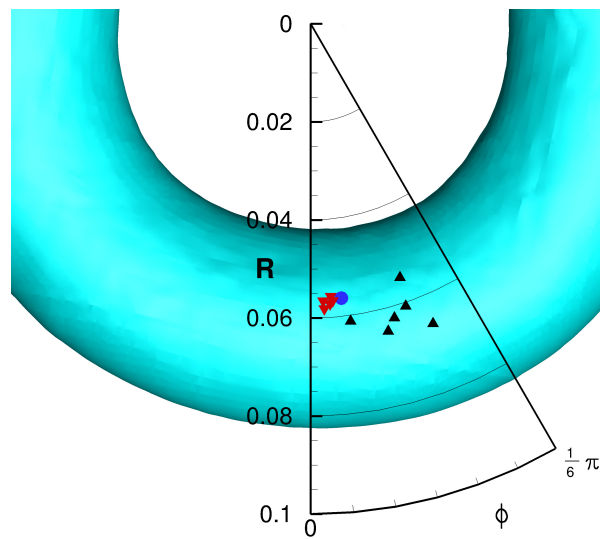
Figure 5.7: Bubble escape locations away from the plane of injection. Position indicated is the average location of the 8 bubbles in each case when the vortex core center reaches $0.65m$: (▲) $\Gamma_0 = 0.0159 m^2/s$, (•) $\Gamma_0 = 0.207 m^2/s$, (▼) $\Gamma_0 = 0.0254 m^2/s$.

center of the vortex ring (R) is evident for cases with different vortex strengths. The degree of escape was found to be substantially larger in the volumetric coupling cases as compared to the two-way coupling, which confirms that the effect of bubbles on the vortex structure is driving this escape behavior. It is conjectured that the bubble escape is dependent on the degree to which the bubbles have locally weakened the vortex, which can change with time. As shown in figure 5.6, large bubbles entrained in a weak vortex can fragment the vortex core, and hence the escape of the bubbles from the plane of injection is more likely and their positions more scattered. Although the bubble escape was observed in the experiments, it was not quantified or correlated to the vortex distortion. For the strong vortex cases, the distortions in the vortex structure are small and the bubbles are settled in relatively close proximity of each other (with minimal escape). However, for weak vortex cases, the bubbles show moderate to significant escape and are scattered further away from each other. This means local variations in the liquid volume fraction will be reduced, and the distorted vortex core can begin to repair itself, as seen in the experimental observations of Sridhar & Katz (1999) [4].

5.4 Quantification of Vortex Distortion and its Effects

It is clear from the previous discussion that the fluid displacement effects are important in distorting the vortex and distributing the vorticity within the core. This can be further seen by inspecting the radial variation of azimuthally averaged vorticity for the unladen and bubble-laden case #5 (corresponding to the weak

vortex strength of $\Gamma_0 = 0.0159m^2/s$ and large bubbles $d_b = 1100\mu m$) with different modeling techniques, as shown in figure 5.8. As shown before, this case exhibits significant escape of bubbles when the vortex ring reaches $x = 0.65m$ (figures 5.6(h), 5.5(c)). Figure 5.6 shows that on the plane of injection, the regions of peak vorticity are pushed away from the core center, due to the bubble passing near the core center. Once the bubbles settle further away from the core and slowly escape from the plane of injection, a different trend appears. With averages taken over the region of bubble escape, a consistent increase in the core center vorticity was observed. This suggests that, as the bubbles move into planes other than the injection plane, they affect a much larger area of the ring. A core center increase in vorticity was also found in the experiments by Sridhar & Katz (1999) [4]. It is also observed from these figures that the one-way and two-way profiles are very similar, maximum variation in the averaged vorticity is less than 1% at any location within the domain. This indicates that even for weak vortex strength and large bubbles, the point-source momentum coupling induced no effect on the flow structure, unlike that observed in the experiments.

Figure 5.9 compares the change in azimuthally averaged vorticity distribution when different size bubbles are entrained in the weak vortex. In general, the core center vorticity increase is larger as the size of the bubbles entrained is increased. It also shows that vorticity increases near the core center, $r/r_c < 0.4$ and decreases further away from the core, $0.5 < r/r_c < 1$. In the strong vortex cases, these averaged vorticity profiles differed only marginally from the unladen cases.

In order to further quantify the degree of vortex distortion as a function of
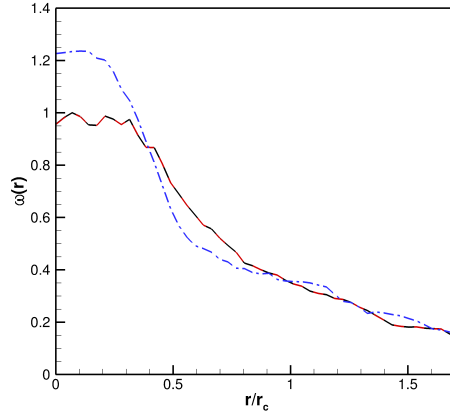
Figure 5.8: Radial variation of averaged vorticity profiles for the weak vortex case of $\Gamma_0 = 0.0159 \ m^2/s$ for $d_b = 1300 \ \mu m$, corresponding to case #5: (——) one-way (un-laden case), (- - -) two-way coupling, (- · -) volumetric coupling:average azimuthally as well as over different planes within thickness of $0.004m$, representative of bubble escape.

Table 5.2: Quantification of vortex distortion using various measures.

Case #	$Cr(\times 10^{-5}m)$	$I_{0.4}$	I	Distortion
1	2.15	0.07	0.68	Minimal
2	8.85	0.26	1.63	Minimal
3	5.15	1.01	5.68	Moderate
4	10.65	0.71	4.15	Significant
5	46.15	2.54	11.8	Significant
6	53.15	1.92	8.77	Significant
7	7.2	0.71	2.1	Minimal
8	7.5	0.09	0.48	Minimal
9	3.75	0.23	1.10	Minimal
10	22.9	0.61	4.10	Moderate
11	20.9	0.62	4.02	Moderate
12	33.6	0.79	4.26	Moderate
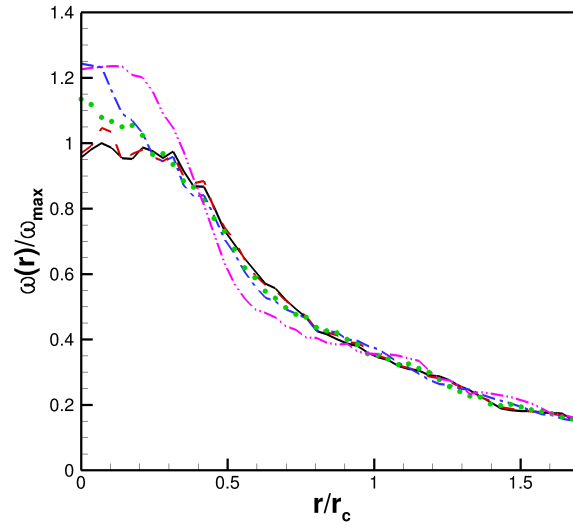
Figure 5.9: Radial variation of azimuthally averaged vorticity profiles, average taken over a several planes within thickness $0.004m$ representative of bubble escape, for the weak vortex case of $\Gamma_0 = 0.0159\ m^2/s$ using the volumetric coupling formulation: (—) unladen case, (- - -) $500\mu m$, (-·-·) $700\mu m$, (● ● ●) $900\mu m$, (-··-··) $1100\mu m$.

bubble size or bubble settling location, several measures can be used. Sridhar & Katz (1999) [4] used two point measurements to characterize the vortex distortion, namely, (i) relative rise in peak vorticity within the vortex core, and (ii) relative rise in the vortex core center (termed as core rise C_r) due to bubble entrainment in comparison with the unladen case. Based on the amount of increase in the peak vorticity or core rise, they classified distortion into minimal, moderate and significant. They found that bubbles that settled in a band of $0.2 \leq r_s/r_c \leq 0.4$ showed moderate to significant distortion based on these criteria. In the present work, in addition to the core rise as the point measure, a global measure based on change in azimuthally averaged vorticity in the bottom plane for bubble-laden and unladen cases was computed and used to quantify vortex distortion. Accordingly, two measures are defined as,

$$I_{0.4} = \frac{\int_0^{2\pi} \int_0^{0.4r_c} |\omega(r) - \omega(r)_{\text{unladen}}| r \, dr \, d\theta}{\Gamma_0} \times 100 \qquad (5.6)$$

$$I = \frac{\int_0^{2\pi} \int_0^{1.71r_c} |\omega(r) - \omega(r)_{\text{unladen}}| r \, dr \, d\theta}{\Gamma_0} \times 100, \qquad (5.7)$$

where $\hat{\omega}$ and $\hat{\omega}_{\text{unladen}}$ represent the local vorticity in the bubble-laden and unladen cases, respectively. Note that this measure can be obtained by using vorticity values in the plane of injection only or by averaging vorticity values over several planes in a region of certain thickness, corresponding to the bubble escape, around the plane of injection. The limits for radial integrations are based on the region containing the settled bubbles where an increase in average vorticity was obtained

compared to the unladen case ($< 0.4 r_c$) or the entire radial region of vortex, not just the core. Both are normalized by the vortex strength, Γ_0.

Table 5.2 lists the values of these measures and accordingly quantifies the amount of distortion as minimal, moderate, and significant. Moderate distortion was classified as having $I > 2.0$ and $Cr > 5.0 \times 10^{-5} m$, significant distortion features $I > 4.0$ and $Cr > 10.0 \times 10^{-5} m$. Anything less than moderate is classified as minimal distortion. Figure 5.10 shows a measure of vortex distortion (I) as a function of bubble settling location for the weak as well as strong vortex strengths. These measures indicate that as bubbles settle further away from the vortex core, they strongly influence the vorticity distribution within the core. As discussed later, within injection of bubbles into the vortex ring, fluid is displaced locally through their presence and motion. The magnitude of fluid displacement and its impact on fluid momentum increases with r_s/r_c. The deformation to the vortex core increases with increased bubble size and final settling location. Note that these measures based on averaged vorticity within the region of bubble escape showed an increase in vortex distortion, even for bubbles that show significant escape.

5.5 Quantifying the Volumetric Displacement Effects

The results presented in section 5.3 demonstrated that a low volume fraction of small Stokes number bubbles can have a substantial effect on the carrier phase flow when volume displacement effects are included. With only point-particle
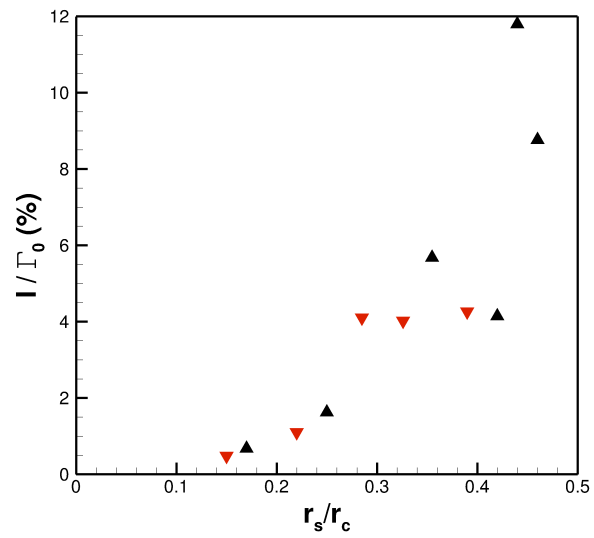
Figure 5.10: Variation of the vortex distortion measures versus bubble settling location for the weak ($\blacktriangle$, $\Gamma_0 = 0.0159m^2/s$) and strong ($\blacktriangledown$, $\Gamma_0 = 0.0254m^2/s$) vortex cases.

momentum-source model, that is two-way coupling, the vortex ring structure was very similar to an unladen case. It is thus important to quantify and investigate these volume displacement effects in order to understand the mechanisms that alter the vortex structures. First the effects on the forces experienced by the bubbles is quantified by obtaining probability mass functions for different forces and comparing them with the unladen and two-way coupling cases. Next, as derived in section 5.5.2, the effect of local variations in fluid volume fractions can be isolated by comparing the linear momentum equations with the two-way coupling counterpart. Equation 5.13 gives an expression for the volumetric coupling influences on the flow field. A few measures to quantify these effects are identified here that are used to discuss the importance of the volumetric coupling formulation for bubble-laden flows.

5.5.1   Effect on Bubble Forces

In order to investigate how the changes in the vortex flow structure affect particle motion, the probability mass functions of the radial pressure, added mass and lift forces on the bubble are shown in figure 5.11 for the one-way, two-way, and volumetric coupling formulations. The forces are normalized by the maximum absolute value amongst the three coupling methods, so changes in both the mean and maximum can be seen. It can be seen that the probability mass functions for these force variations are nearly identical for the unladen (one-way) case and bubble-laden case with two-way coupling. However, all forces show a broader distribution

with volumetric coupling. Comparing the mean of the distributions between the volumetric and two-way coupling, the pressure and added mass forces indicate a smaller force exerted onto the bubble towards the core with the volumetric coupling formulation. The mean pressure force decreased by 7.6%, whereas the added mass force decreased by 12.8%, while the lift force shows a larger force pushing away from the core center, with an increase of 1.7%. The effect on drag force was found to be very small. The combined effect of changes in these forces results in a radial settling location that is slightly further away when the volume displacement effects are considered. These modifications to bubble forces due to vortex distortion are found to be important to obtain the correct trend for settling locations as shown in figure 5.3.

5.5.2   Measuring Volumetric Influences

The volume displacement effects in the volumetric coupling formulation play an integral role in properly modeling the conservation of mass and momentum equations. It is important to understand how these effects manifest themselves, and a method of quantification in comparison with the standard two-way coupling point-source approach is needed. In order to find the magnitude of the volumetric coupling forces on the flow, an expression for the source term due to volume displacement effects is derived by writing the original conservative form of the governing equations in a non-conservative form and expressing the additional terms in comparison with the two-way coupling formulation as the *volumetric coupling*
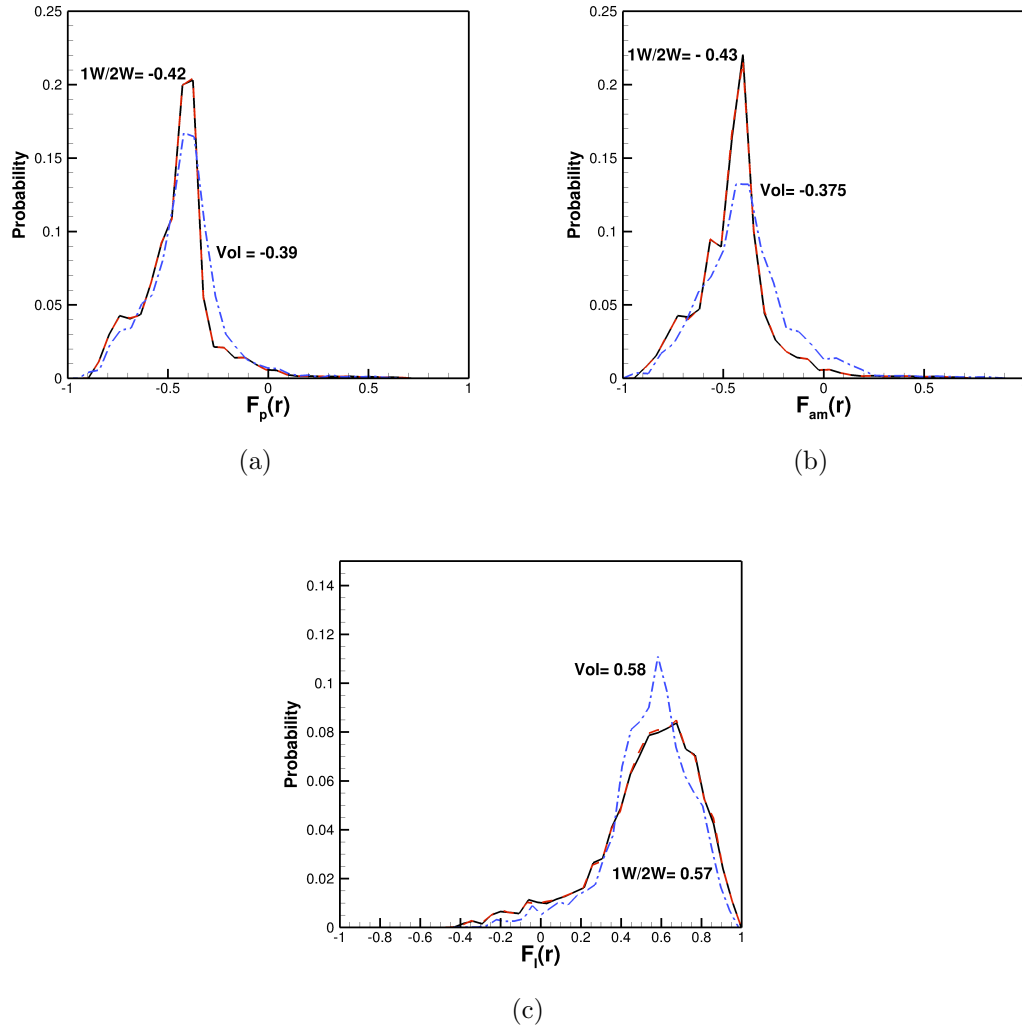
Figure 5.11: Probability mass functions for the radial components of forces on the bubble obtained in (—) one-way, (---) two-way, (-·-·) volumetric coupling formulation for case # 5: (a) radial pressure force, (b) radial added mass force, and (c) radial lift force, normalized by the maximum absolute value. Mean values of the forces are also given for one-way (or unladen), two-way, and volumetric coupling methods.

force. Equation 5.8 gives the volumetric coupling momentum equations in the conservative form, with $\mathbf{f}_{b\to\ell}$ being the two-way coupling source term,

$$\frac{\partial(\rho_\ell\theta_\ell\mathbf{u}_\ell)}{\partial t} + \nabla\cdot(\rho_\ell\theta_\ell\mathbf{u}_\ell\mathbf{u}_\ell) = -\theta_\ell\nabla p + \nabla\cdot[\mu_\ell\theta_\ell(\nabla\mathbf{u}_\ell + \nabla\mathbf{u}_\ell^T)] + \mathbf{f}_{b\to\ell} - \rho_\ell\theta_\ell\mathbf{g} \tag{5.8}$$

The first two terms are then expanded in a non-conservative form to obtain,

$$\mathbf{u}_\ell\underbrace{\left(\frac{\partial(\rho_\ell\theta_\ell)}{\partial t} + \nabla\cdot(\rho_\ell\theta_\ell\mathbf{u}_\ell)\right)}_{(I)} + \rho_\ell\theta_\ell\left(\frac{\partial\mathbf{u}_\ell}{\partial t} + \mathbf{u}_\ell\cdot\nabla\mathbf{u}_\ell\right) = -\theta_\ell\nabla p$$
$$+ \nabla\cdot\left(\mu_\ell\theta_\ell(\nabla\mathbf{u}_\ell + \nabla\mathbf{u}_\ell^T)\right) + \mathbf{f}_{b\to\ell} - \rho_\ell\theta_\ell\mathbf{g}. \tag{5.9}$$

Utilizing conservation of mass, term (I) vanishes,

$$\rho_\ell\theta_\ell(\frac{\partial\mathbf{u}_\ell}{\partial t} + \mathbf{u}_\ell\cdot\nabla\mathbf{u}_\ell) = -\theta_\ell\nabla p + \nabla\cdot[\mu_\ell\theta_\ell(\nabla\mathbf{u}_\ell + \nabla\mathbf{u}_\ell^T)] + \mathbf{f}_{b\to\ell} - \rho_\ell\theta_\ell\mathbf{g}. \tag{5.10}$$

The above equation can be rewritten using the product rule for the advective terms and re-arranging to get,

$$\rho_\ell\theta_\ell\left(\frac{\partial\mathbf{u}_\ell}{\partial t} + \nabla\cdot(\mathbf{u}_\ell\mathbf{u}_\ell)\right) = -\theta_\ell\nabla p + \nabla\cdot[\mu_\ell\theta_\ell(\nabla\mathbf{u}_\ell + \nabla\mathbf{u}_\ell^T)] +$$
$$\mathbf{f}_{b\to\ell} - \rho_\ell\theta_\ell\mathbf{g} + \rho_\ell\theta_\ell(\mathbf{u}_\ell\nabla\cdot\mathbf{u}_\ell) \tag{5.11}$$

To find the forcing terms arising from the volumetric displacement effect, equation 5.11 is compared to the traditional one-way coupling equations for an incompress-

ible fluid (equation 5.12) with an additional source $\widehat{\Delta \mathbf{V}}$,

$$\rho_\ell \left(\frac{\partial \mathbf{u}_\ell}{\partial t} + \nabla \cdot (\mathbf{u}_\ell \mathbf{u}_\ell) \right) = -\nabla p + \nabla \cdot [\mu_\ell (\nabla \mathbf{u}_\ell + \nabla \mathbf{u}_\ell^T)] - \rho_\ell \mathbf{g} + \widehat{\Delta \mathbf{V}}. \quad (5.12)$$

Note that the advective terms in equation 5.12 (and hence in equation 5.11 as well) are written in a conservative form, mainly because for incompressible flows, the numerical approach uses this form for discrete approximations. The source $\widehat{\Delta \mathbf{V}}$ can be obtained by subtracting equation 5.12 from 5.11.

$$\widehat{\Delta \mathbf{V}} = \underbrace{\theta_b \nabla p}_{(\widehat{\Delta \mathbf{V}}_1)} + \underbrace{\rho_\ell \theta_b \left(\frac{\partial \mathbf{u}_\ell}{\partial t} + \nabla \cdot (\mathbf{u}_\ell \mathbf{u}_\ell) \right)}_{(\widehat{\Delta \mathbf{V}}_2)} - \underbrace{\mu_\ell [\nabla \cdot \theta_b (\nabla \mathbf{u}_\ell + \nabla \mathbf{u}_\ell^T)]}_{(\widehat{\Delta \mathbf{V}}_3)} +$$

$$\underbrace{\boldsymbol{f}_{b \to \ell}}_{(\widehat{\Delta \mathbf{V}}_4)} + \underbrace{\rho_\ell \theta_b \mathbf{g}}_{(\widehat{\Delta \mathbf{V}}_5)} + \underbrace{\rho_\ell \theta_\ell \mathbf{u}_\ell (\nabla \cdot \mathbf{u}_\ell)}_{(\widehat{\Delta \mathbf{V}}_6)} \quad (5.13)$$

The net source includes both the liquid displacement effects, due to spatial and temporal volume fraction gradients, as well as the two-way momentum coupling force.

The terms on the right hand side can be interpreted as follows.

$$
\begin{aligned}
\widehat{\Delta \mathbf{V}}_1 &= \text{Local pressure gradient term,} \\
\widehat{\Delta \mathbf{V}}_2 &= \text{The unsteady and fluid inertial terms,} \\
\widehat{\Delta \mathbf{V}}_3 &= \text{Viscous stresses due to volume fraction variation,} \\
\widehat{\Delta \mathbf{V}}_4 &= \text{Point-source momentum transfer term,} \\
\widehat{\Delta \mathbf{V}}_5 &= \text{Hydrostatic gravity term,} \\
\widehat{\Delta \mathbf{V}}_6 &= \text{Local flow divergence term.}
\end{aligned}
$$

Note that, $\widehat{\Delta \mathbf{V}}_1$ and $\widehat{\Delta \mathbf{V}}_4$ can be combined together to obtain the net two-way coupling momentum source $\mathbf{f}^t_{b \to \ell}$. By separating out volumetric effects in this manner it is possible to measure the relative influence of these effects compared to traditional two-way coupling momentum transfer effects.

5.5.3 Two-Way Point-Source Versus Volumetric Coupling Reaction

The individual contribution of different reaction terms in $\mathbf{f}^t_{b \to \ell}$ are computed on each bubble for the different cases studied. The *magnitudes* of forces (averaged over the $N_b = 8$ injected bubbles) are plotted against the gravity parameter gr_b^3/Γ_0^2 in figure 5.12. The forces are normalized by the bubble weight. The buoyancy force (or the hydrostatic pressure gradient force, $\rho_\ell \mathcal{V}_b \mathbf{g}$) is close to 1000 times the weight of the bubble owing to the small specific gravity of the bubble. It is also observed that the magnitudes of individual drag, lift, added mass and pressure forces (due to dynamic pressure gradient) are large, and on the order of 300-1200 times the bubble weight. However, the net two-way reaction force, $\mathbf{f}^t_{b \to \ell}$, is found to be small and does not affect the vortex ring structure in a two-way coupling formulation, even for the weak vortex case. This can be explained based on the balance of the forces on the bubbles.

If the bubbles settle perfectly at a location that remains stationary with respect to the vortex core, then the different forces acting on them are in perfect balance
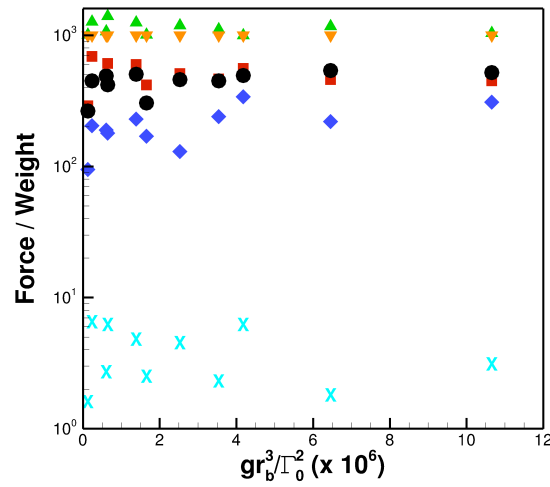
Figure 5.12: The magnitudes of individual two-way coupling forces averaged on the bubbles and normalized by the bubble weight for different cases on log-linear scale: (▲) drag, (■) dynamic pressure gradient, (●) lift, (♦) added mass, (▼) hydrostatic pressure gradient (buoyancy force), and (X) summation of net force on the bubble.
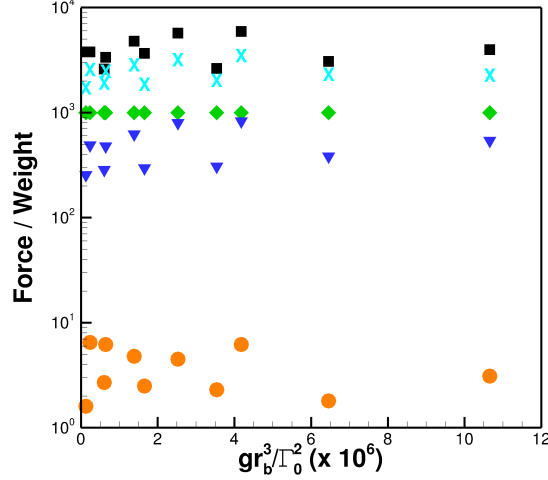
Figure 5.13: The magnitudes of individual volumetric coupling reaction forces (given in equation 5.13) normalized by the net bubble weight on log-linear scale. The forces are averaged in time after the bubbles are settled: ($\blacktriangledown$) unsteady and inertial terms ($\overline{\Delta V}_2$), ($\bullet$) two-way coupling momentum transfer term ($\overline{\Delta V}_1 + \overline{\Delta V}_4$), ($\blacklozenge$) hydrostatic gravity term ($\overline{\Delta V}_5$), ($\blacksquare$) local divergence term ($\overline{\Delta V}_6$), and (X) total magnitude of signed summation of the volumetric forces ($\overline{\Delta V}_{\text{net}}$).

with their weight, that is,

$$(\mathbf{F}_d + \mathbf{F}_\ell + \mathbf{F}_{am} + \mathbf{F}_p) = -\mathbf{F}_g = \rho_b \mathcal{V}_b \mathbf{g}. \tag{5.14}$$

Owing to transitional flow in a vortex ring, the bubbles do not settle perfectly but continue to circle around a mean settling location. But, the net reaction force is still small in a two-way coupling formulation due to the small specific gravity of the bubbles. While these forces have components in all three directions, they are dominated by the components in the settling plane as shown in figure 5.1(c).

Figure 5.13 shows the relative magnitudes of the various volumetric source

terms obtained in equation 5.13. These magnitudes are obtained by accounting for the net sources on the fluid and averaging them over the period of time after the bubbles have settled around a mean position. The magnitudes are normalized by the net bubble weight and are given as,

$$\overline{\Delta V_i} = \frac{\overline{\sum_{\mathrm{cv}} \left|\widehat{\Delta \mathbf{V}}_i\right| \mathcal{V}_{\mathrm{cv}}}}{W_b} = \frac{\overline{\sum_{\mathrm{cv}} \left(\widehat{\Delta V}_{i_x}^2 + \widehat{\Delta V}_{i_y}^2 + \widehat{\Delta V}_{i_z}^2\right)^{1/2} \mathcal{V}_{\mathrm{cv}}}}{N_b \rho_b \mathcal{V}_b g}, \qquad (5.15)$$

where N_b is the number of bubbles, W_b is the weight of the bubbles, $\mathcal{V}_{\mathrm{cv}}$ is the volume of the cell and the overbar represents time-average. Also shown in the figure 5.13 is the magnitude of the vector sum (signed sum) of the volumetric forces normalized by the net bubble weight,

$$\overline{\Delta V_{\mathrm{net}}} = \frac{\overline{\widehat{\Delta V}_{\mathrm{net}}}}{W_b} = \frac{\overline{\sum_{\mathrm{cv}} \left|\sum_{i=1}^6 \widehat{\Delta \mathbf{V}}_i\right| \mathcal{V}_{\mathrm{cv}}}}{N_b \rho_b \mathcal{V}_b g}. \qquad (5.16)$$

It is observed that the individual magnitudes of the different volumetric coupling forces are large, with the divergence-based reaction term ($\overline{\Delta V}_6$) being the largest in all cases. Since the local divergence in flow field is related to the local spatio-temporal variations in the bubble volume fraction (see equation 3.13), the effect of fluid displaced by the presence of bubbles can be significant. The summed magnitudes of two-way coupling forces, although large, are still smaller than this divergence reaction term. The forces here are roughly constant when normalized by the bubble weight for all gr_b^3/Γ_0^2 since both the volumetric coupling forces and

the bubble weights are proportional to bubble volume. There are variations which are caused by the differences in the flow field seen by the bubbles due to their respective settling distances and bubble escape properties. The net magnitude of the vector summation of the volumetric coupling forces ($\overline{\Delta V_{\text{net}}}$) shows that the net addition is smaller than some of the individual components, and thus some of these effects are balancing each other. However, the net magnitude is still considerably larger than the net magnitude of the two-way coupled forces (which is close to the weight of the bubbles for settled bubbles). Thus, the volumetric coupling does impart a larger reaction force and can cause distortion of the vortex ring for certain cases.

5.5.4 Comparing Volumetric Forces to a Simple Two-Dimensional Estimate

In previous two-dimensional work on bubble-vortex tube interactions [35], models have been developed to estimate an analogous expression for the volumetric coupling force. The reaction force was derived by directly subtracting the one-way coupled Navier-Stokes equations (5.17), from the volumetric coupling equation 3.14, shown again here for completeness. This expression is in general agreement with those given by Sridhar & Katz (1999) [4] and Druzhinin & Elghobashi (1998) [11] for similar bubble-laden systems.
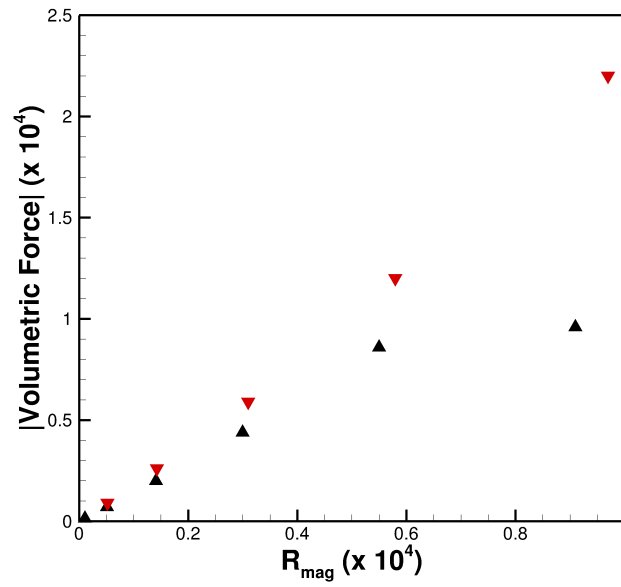
Figure 5.14: Comparison of the net volumetric coupling force obtained in present three-dimensional computations to the two-dimensional estimate based on a simplified Gaussian vortex of similar strength for the weak (▲, $\Gamma_0 = 0.0159m^2/s$), and strong (▼, $\Gamma_0 = 0.0254m^2/s$) cases.

$$\underbrace{\frac{\partial(\rho_\ell \mathbf{u}_\ell)}{\partial t} + \nabla \cdot (\rho_\ell \mathbf{u}_\ell \mathbf{u}_\ell)}_{\boldsymbol{C}} \; = \; \underbrace{-\nabla p}_{\boldsymbol{P}} + \underbrace{\nabla \cdot [\mu_\ell(\nabla \mathbf{u} + \nabla \mathbf{u}^T]}_{\boldsymbol{V}} - \underbrace{\rho_\ell \mathbf{g}}_{\boldsymbol{B}} \qquad (5.17)$$

$$\underbrace{\frac{\partial(\rho_\ell \theta_\ell \mathbf{u}_\ell)}{\partial t} + \nabla \cdot (\rho_\ell \theta_\ell \mathbf{u}_\ell \mathbf{u}_\ell)}_{\hat{\boldsymbol{C}}} \; = \; \underbrace{-\nabla p}_{\hat{\boldsymbol{P}}} + \underbrace{\nabla \cdot [\theta_\ell \mu_\ell(\nabla \mathbf{u} + \nabla \mathbf{u}^T]}_{\hat{\boldsymbol{V}}} - \underbrace{\rho_\ell \theta_\ell \mathbf{g}}_{\hat{\boldsymbol{B}}} + \mathbf{f}^t_{b \to \ell} (5.18)$$

Subtracting the two equations gives,

$$\widehat{\Delta \boldsymbol{R}} = (\boldsymbol{C} - \hat{\boldsymbol{C}}) + (\hat{\boldsymbol{P}} - \boldsymbol{P}) + (\hat{\boldsymbol{V}} - \boldsymbol{V}) + (\hat{\boldsymbol{B}} - \boldsymbol{B}) + \mathbf{f}^t_{b \to \ell}. \qquad (5.19)$$

To obtain a simple two-dimensional estimate of the reaction force, the differences in the convective, viscous, pressure, buoyancy and two-way coupling momentum transfer terms, shown in equation 5.19, can be approximated using a Gaussian vortex profile (based on the nature of the averaged vorticity distribution shown in figure 5.8) under the assumptions of an undisturbed flow field and zero bubble acceleration (or that the forces on bubbles are in balance) which provides good estimates for velocity, vorticity, and dynamic pressure gradient at all positions in the vortex core. The individual terms in equation 5.19 can then be simplified by neglecting the viscous terms (for low volume loadings and large Re_{vx}) as [35],

$$\mathbf{C} - \hat{\mathbf{C}} \; = \; \rho_\ell \frac{D\mathbf{u}_\ell}{Dt} - \frac{D\left(\theta_\ell \rho_\ell \mathbf{u}_\ell\right)}{Dt} \approx \rho_\ell \frac{u_\theta^2}{r} - \rho_\ell \frac{\theta_\ell u_\theta^2}{r} \approx \rho_\ell \theta_b \frac{u_\theta^2}{r}$$

$$\hat{\mathbf{B}} - \mathbf{B} \; = \; -\theta_\ell \rho_\ell \mathbf{g} + \rho_\ell \mathbf{g} = +\theta_b \rho_\ell \mathbf{g}. \qquad (5.20)$$

Also, assuming that the bubbles reach a settling location that is steady with respect to the vortex core, the net forces on the bubble are in balance,

$$\mathbf{F}_{b \to \ell} = -\left(\mathbf{F}_d + \mathbf{F}_\ell + \mathbf{F}_{am} + \mathbf{F}_p\right) \sim \mathbf{F}_G = -\rho_b \mathcal{V}_b \mathbf{g};$$

$$\therefore \mathbf{f}_{b \to \ell}^t \sim \sum_{b=1}^{N_b} \mathcal{G}_\Delta(\mathbf{F}_{b \to \ell}) = -\theta_b \rho_b \mathbf{g}. \tag{5.21}$$

Note that the interphase reaction term will be small when the bubbles are not accelerating, explaining why the point-particle, two-way coupling source causes almost no vortex distortion.

If all terms in equations 5.20 and 5.21 are combined, and multiplied through by the local volume of the fluid cell, then the two-dimensional approximation to the total reaction force ($\Delta\mathbf{R} = \mathcal{V}_{cv}\widehat{\Delta\mathbf{R}}$) onto the fluid because of N_b bubbles having volume $\mathcal{V}_b$ can be obtained. The radial and tangential components (radially outward and counterclockwise being positive) of this force are given as,

$$R_r = -N_b \mathcal{V}_b \left(\rho_\ell u_\theta^2 / r_s - g(\rho_\ell - \rho_b)\sin(\theta_s)\right) \tag{5.22}$$

$$R_\theta = N_b \mathcal{V}_b g(\rho_\ell - \rho_b)\cos(\theta_s) \tag{5.23}$$

$$R_{mag} = \sqrt{R_r^2 + R_\theta^2}, \tag{5.24}$$

where R_{mag} denotes the net magnitude of these two components. Note that equation 5.24 indicates that the two-dimensional estimate of the interaction force

varies with the bubble volume. Figure 5.14 compares the volumetric coupling force magnitudes directly computed in this work ($|\widehat{\overline{\Delta \mathbf{V}}_{\mathrm{net}}}|$) to the prediction based on the stationary two-dimensional model (R_{mag}). For the strong vortex cases, where the vortex distortion is minimal and the bubbles tend to settle close to each other, the present computational prediction of the volumetric coupling force is directly correlated with the two-dimensional estimate. For these cases, the bubble escape observed in the computations was minimal and the steady two-dimensional assumption seems valid. For the weak vortex, however, the forces tend to deviate from a direct correlation. The vortex distortion effects and bubble escape was significant for these cases.

5.5.5 Volumetric Reaction Force and Vortex Distortion

In order to study the influence of the net volumetric coupling force ($\overline{\Delta V}_{\mathrm{net}}$) on the vortex structure and other forces acting on the bubble, it is first non-dimensionalized by the net bubble weight and plotted against the non-dimensional bubble settling location, $\bar{r}_s$, in figure 5.15.

The weak and strong vortex cases are identified for comparison. It is observed that, for the strong vortex case, as the bubbles settle further away from the vortex core, the net volumetric coupling force is large. This is also the trend for the majority of the bubbles with the weak vortex, except for two cases where the bubbles settle further away from the core, where the normalized reaction force is lower. The magnitudes of these forces are larger for the strong vortex cases

compared to the weaker vortex. These two effects can be explained as follows. For the strong vortex, the bubbles tend to settle in close proximity of each other with little or no escape, increasing the local spatial gradient in the bubble volume fraction. This increases the local divergence term and hence the local volume displacement effects. They also tend to move more rapidly due to larger circulation rates. For the weaker vortex, on the other hand, the bubbles continue to move in small circles around a mean settling location and generally are more dispersed. They also show significant bubble escape from the plane of injection as shown in figures 5.5 and 5.7. These combined effects tend to have relatively lower net volumetric coupling forces for the weaker vortex. However, it is observed in the experiments as well as in the simulations that the large bubbles distort the weaker vortex significantly more compared to the strong vortex. To explain the effect of volumetric coupling forces on the vortex distortion, it is important to compare the volumetric coupling force to some measure of the vortex strength.

The volumetric coupling force, can be normalized by the radial hydrodynamic pressure force within an undisturbed vortex core, which scales as $\rho_\ell \Gamma_0^2$ (which was also used to non-dimensionalize the bubble weight to obtain $\bar{g}$). The variation of this normalized force against the settling location, $\bar{r}_s$ is shown in figure 5.16(a).

Two distinct trend curves arise from this normalization, indicating that the bubbles tend to settle further away for the weak vortex as compared to the large vortex. Note that the relationship of this normalized force with respect to the settling location for weak as well as strong vortex strengths is not linear.

Since variation of the vortex strengths results in different vortex Reynolds num-
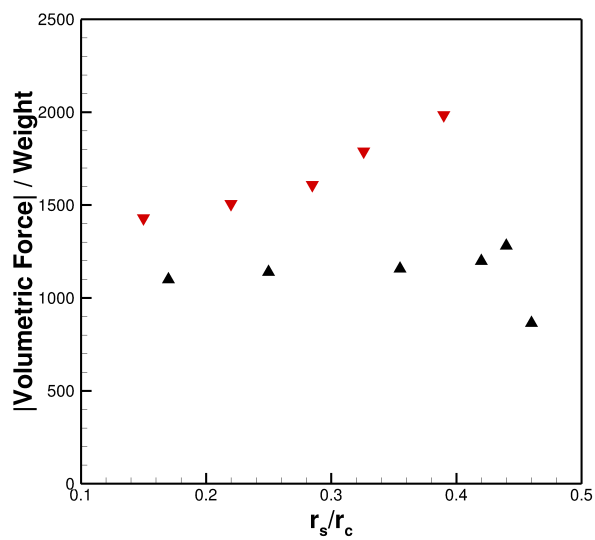
Figure 5.15: The resultant volumetric coupling force $(\overline{\widehat{\Delta V}_{\text{net}}})$ normalized by the net bubble weight for the, weak ($\blacktriangle$, $\Gamma_0 = 0.0159 m^2/s$) and strong ($\blacktriangledown$, $\Gamma_0 = 0.0254 m^2/s$) vortex cases, versus the mean non-dimensional settling location (r_s/r_c).
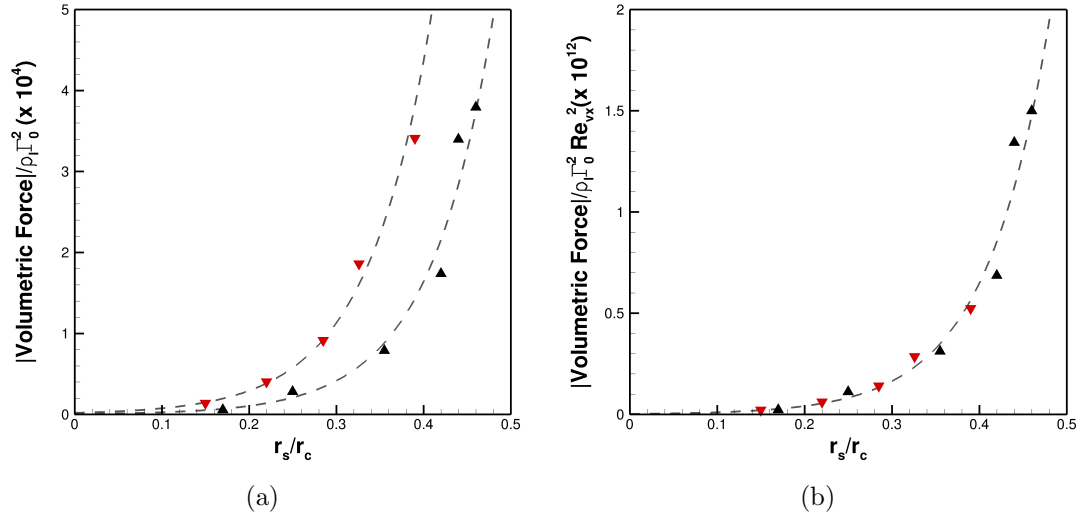
Figure 5.16: The net volumetric coupling force $(\overline{\widehat{\Delta V}_{\text{net}}})$ as a function of the mean settling location, r_s/r_c, for the weak ($\blacktriangle$, $\Gamma_0 = 0.0159 m^2/s$) and strong ($\blacktriangledown$, $\Gamma_0 = 0.0254 m^2/s$) vortex strengths: (a) normalized by the net radial hydrodynamic pressure force in an undisturbed vortex ($\rho_\ell \Gamma_0^2$), (b) normalized by $\rho_\ell \Gamma_0^2 Re_{vx}^2$.

bers, $Re_{vx} = \Gamma_0/\nu_\ell$, it is then reasonable to assume that the normalized volumetric coupling force depends on Re_{vx}. The trend tends to collapse well when the net volumetric coupling force is normalized by the net hydrodynamic pressure force times the vortex Reynolds number squared, $\rho_\ell \Gamma_0^2 Re_{vx}^2$, as shown in figure 5.16(b). This plot shows that, as the bubbles tend to settle further away for the weak vortex, the normalized force is larger compared with the corresponding cases for the strong vortices. This plot thus indicates that the potential of the bubbles to distort the vortex ring is large for the weaker vortex, and hence significant distortion of the ring is observed for these cases. The volumetric coupling forces thus are given as,

$$\frac{\overline{\widehat{\Delta V}_{\text{net}}}}{\rho_\ell \Gamma_0^2} = Re_{vx}^2 \mathcal{F}\left(\bar{r}_s\right), \tag{5.25}$$

where $\mathcal{F}$ is a non-linear function of the settling location $(\bar{r}_s)$. In addition, it was previously shown that the settling location depends on the ratio of the bubble weight to the hydrodynamic pressure force, $\bar{g} = gr_b^3/\Gamma_0^2$. It is important to note that the drag and lift forces acting on the bubble implicitly depend on bubble Reynolds number Re_b, which in turn depend on Re_{vx}. The bubble Reynolds numbers do not vary appreciably for the present case and hence the dependence of the drag and lift forces on vortex Reynolds number is weak. However, it is observed that the volumetric coupling forces, when normalized by Re_{vx}^2 and the hydrodynamic pressure force $(\rho_\ell \Gamma_0^2)$, are direct function of the settling location and collapse the data onto a single curve. This indicates that the vortex distortion occurring due to the fluid volume displaced by the bubbles is a function of Re_{vx} and gr_b^3/Γ_0^2.

In order to understand the directionality of the normalized net volumetric coupling force $(\overline{\Delta V}_{\text{net}}/\rho_\ell \Gamma_0^2 Re_{vx}^2)$, it is plotted in the $r_s - \theta_s$ co-ordinates together with the location of the settled bubbles as shown in figure 5.17. The arrow denotes the directionality of the net force and the magnitude is represented by its length. It is observed that, for the weak as well as the strong vortex cases, as the bubbles settle further away from the vortex core, the net volumetric coupling force is also large. The resultant reaction force is still large for these cases. It is noticed from these plots that the resultant volumetric coupling forces are aligned roughly at 45° from the horizontal. Present computational results as well as experimental data [4]
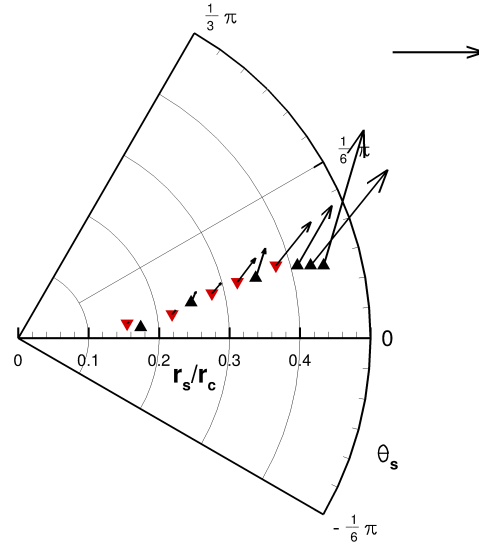
Figure 5.17: The normalized resultant volumetric coupling force $(\overline{\widehat{\Delta V}_{\mathrm{net}}}/\rho_\ell \Gamma_0^2 Re_{vx}^2)$ at different mean settling locations for strong ($\blacktriangledown$, $\Gamma_0 = 0.0254 m^2/s$) and weak ($\blacktriangle$, $\Gamma_0 = 0.0159 m^2/s$) vortices. Arrow length represents 1×10^{-12} dimensionless units.

indicate a core elongation at roughly $45°$ incline from the horizontal for cases in which significant distortion occurs.

This approximate angle at which the core elongation occurs is the result of a competition between two mechanisms, the natural inclination of the vortex to have a horizontal elongation owing to its traveling nature (in the streamwise direction), and the influence of the bubbles attempting to push the core to a more vertically inclined angle, shown in figure 5.17. The effect of fluid displaced by the bubbles is to locally elongate the flow structure near the center of the vortex core.

Finally, the vortex distortion index (I) defined in equation 5.7 is plotted against the normalized volumetric coupling force in figure 5.18.

This plot clearly shows that increase in volumetric coupling force increases the
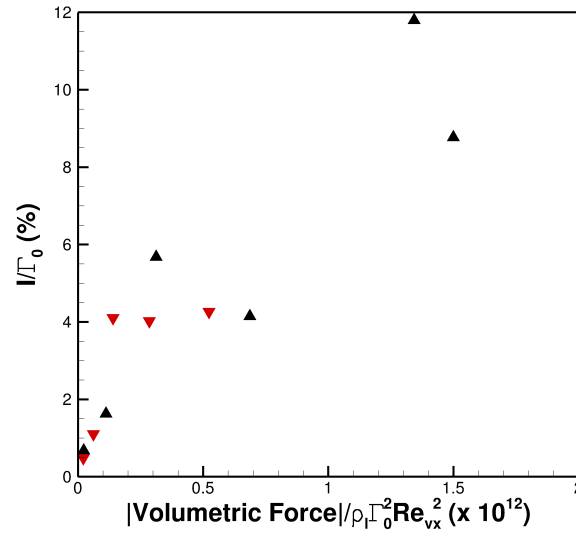
Figure 5.18: The vortex distortion index (I) versus the normalized resultant volumetric coupling force $(\widehat{\overline{\Delta V}_{\mathrm{net}}}/\rho_\ell\Gamma_0^2 Re_{vx}^2)$ for strong ($\blacktriangledown$, $\Gamma_0 = 0.0254 m^2/s$) and weak ($\blacktriangle$, $\Gamma_0 = 0.0159 m^2/s$) vortex.

vortex distortion. Since the volumetric coupling force contains a major contribution from the local divergence term in the velocity field then vortex distortion increases as the bubbles displace the fluid locally. As larger bubbles tend to displace more fluid and also settle further away from the vortex core, vortex distortion increases with increase in bubble settling location as shown previously in figure 5.10.

Chapter 6 – Taylor-Green Vortices

With the dominance of volumetric coupling forces established for some cases, such as the traveling vortex ring, and it being shown to be negligible in others, such as the turbulent channel flow cases, it is reasonable to wonder if criteria can be established for the importance of this force. This section describes a method for classifying the ratio of the volumetric to two-way coupling forces, in hopes of learning when and why these forces are important, as well as when they become negligible.

$$u(x, y, t) = -4cos(\pi x)sin(\pi y) \tag{6.1}$$

$$v(x, y, t) = 4sin(\pi x)cos(\pi y) \tag{6.2}$$

Taylor-Green vortices offer an inexpensive test case to measure volumetric force effects, the initial velocity profile is provided in equations 6.1 and 6.2. Figures 6.1(a) and 6.1(b) show the general profile of these vortices. The black dots in the second figure are particle locations after $t = 0.2s$ has passed. The particles were initial placed in ordered rows of $10 \times 10 \times 2$ particles, where the third component is into the page. In order to determine the dominant mechanism of momentum transport, a measure of the relative ratio of volumetric to two-way coupling forces is created. The volumetric input is measured as shown in equation 6.3. The two-way coupling measure is analogously defined as the total two-way coupling force exerted onto the fluid. So a ratio (volumetric/two-way) of these forces of less than one, signifies that two-way coupling forces are larger, a ratio of one says they
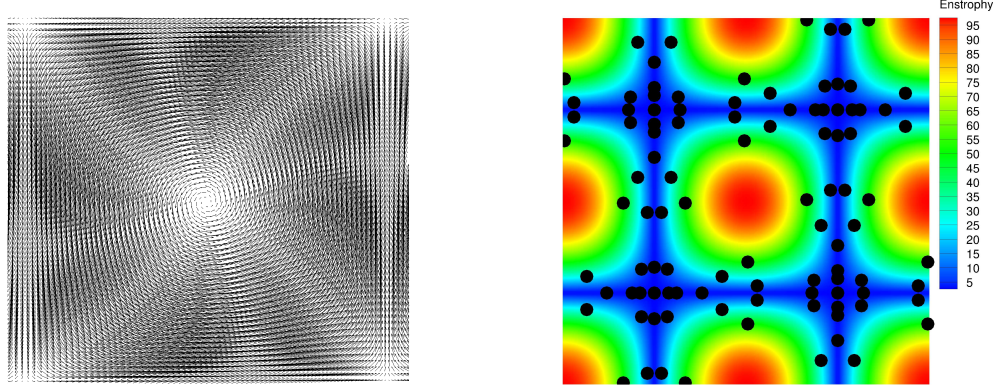
(a) Velocity vectors of the central vortex.

(b) Vorticity contours and particle locations.

Figure 6.1: Taylor-Green Vortices

are the same, and higher ratios mean volumetric coupling forces are larger than two-way coupling forces. Collision effects are neglected in this study.

$$\overline{\Delta V_{\text{net}}} = \overline{\frac{\widehat{\Delta V_{\text{net}}}}{W_b}} = \frac{\overline{\sum_{\text{cv}} \left| \sum_{i=1}^{6} \widehat{\Delta \mathbf{V}}_i \right| \mathcal{V}_{\text{cv}}}}{N_b \rho_b \mathcal{V}_b g}. \tag{6.3}$$

Table 6.1 gives the parameters for the four cases examined in this chapter. The

Table 6.1: Parameter variations for Taylor-Green vortex cases. Here ρ_ℓ is the liquid density, μ_ℓ is the liquid viscosity, d_b is bubble radius, N_b is the number of bubbles.

Case #	Symbol	ρ_ℓ (kg/m^3)	$\mu_\ell \times 10^{-5}$ (kg/ms)	d_b (m)	N_b	g (m/s^2)
A	▲	1000	2	$0.001m$	200	0.0
B	▼	1	2	$0.001m$	200	0.0
C	●	1	0.002	$0.001m$	200	0.0
D	◆	1	2	$0.001m$	200	-9.81
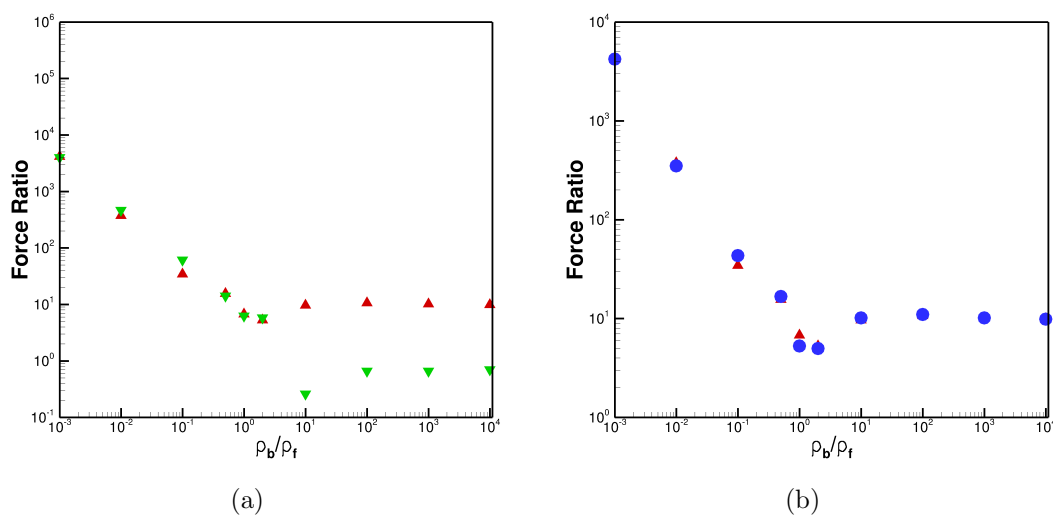
Figure 6.2: (a) Cases A and B: The effect of varying liquid density on the ratio of volumetric to two-way coupling forces, the Reynolds number is not constant here since only the liquid density is varied. (b) Cases A and C: Two cases with the same Reynolds number, but who's liquid densities vary by a factor of 1000, the viscosity is altered to enforce the same Reynolds number.
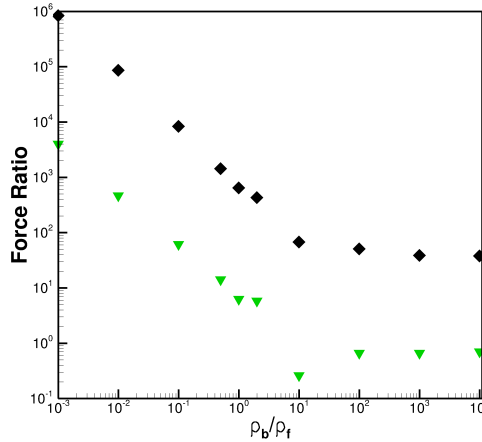
Figure 6.3: Cases B and D: Two cases with the same Reynolds number, but case D includes the gravity, whereas case B neglects it.

parameters varied are the fluid density, the Reynolds number and the inclusion or exclusion of gravitational effects. Figure 6.2(a) shows the effect of varying the liquid density. Since the liquid density is the only parameter changed between these two cases, the systems are at two different Reynolds numbers which are a factor of 1000 different. The two trends seem to collapse for lighter than fluid bubbles, but as the density ratio increases a clear separation is seen. When the liquid density is still varied, but the Reynolds number is held constant, as in figure 6.2(b). Note that the force ratios collapse well for the entire range of density ratios. When gravity is included, but all other parameters are held constant, there is a dramatic increase the in the volumetric to two-way force ratio, this is shown in figure 6.3.

A few trends stand out from these results. The first is that when gravity is neglected, the force ratios collapse for the smallest Stokes number particles. When

the Reynolds number is held constant, the entire range of density ratios show a solid collapse. This suggests that the force ratio is strongly dependent on the bubble response time within the flow. Due to the nature of the flow, and the short times that must be simulated to avoid the bubbles from congregating in the center of the vortices, it makes sense why even for the largest bubble to liquid density ratios, the force ratio stays of order 1 or just slightly smaller. When gravitational effects are included, causing the even the lightest objects to act less like tracers within the flow field, the small density ratio collapse that was previous seen no longer occurs. This suggests that in flows where there is a constant acceleration or something forcing particulate motion to not strictly follow liquid streamlines, the force ratio will be significantly larger than in system where a fully developed state is reached and maintained via forcing.

Chapter 7 – Conclusions and Outlook

7.1 Conclusions

This work focused on coupling methods for multiphase phase flows using Eulerian-Lagrangian methods. To begin with, an in depth analysis of how the two-way and volumetric coupling approximations predict the features of a turbulent channel flow was performed. This work was motivated through basic intuition and a series of studies showing how profound an effect the inclusion of a volume displacement model can have in many systems. The systems that show significant differences are not limited to bubbly flows but also include flows with Stokes numbers much larger than one and/or particle to fluid density ratios greater than one [36]. For large density ratios, the coupling method showed no deviation in prediction of the traditional statistical measures of turbulent flows; i.e. mean velocity, gas and particle *rms* velocities and volume fraction. Near wall and channel centerline images of instantaneous profiles of gas phase structures and particle profiles also showed little to no variation when the coupling method was changed. A statistical analysis was performed using the probability density function method and the radial distribution function methods to see if particle clustering was affected throughout the domain. These methods showed no discernible difference when the coupling method was changed, only including interparticle collisions using an inter-particle repulsion force model drastically affected the statistical measures of particle clustering, which is to be expected. With it shown that having a moderate volume fraction not being a sufficient condition for volumetric coupling dominance, we look at flows of interest involving a low disperse to fluid phase density ratio.

For investigating low density ratio cases, direct numerical simulation utilizing point-particle Lagrangian bubble tracking was performed to study interactions of a few small bubbles with a traveling vortex ring, corresponding to the experimental setup of Sridhar & Katz (1999) [4]. Two approaches modeling the effects of bubbles on the vortex ring were studied: (i) two-way coupling, and (ii) volumetric coupling. In both approaches, the bubbles are considered subgrid and only the centers of the bubbles are tracked by modeling the forces on the bubbles through drag, lift, pressure, added mass, and gravity. In the traditional two-way coupling approach, the effect of the bubbles on the flow was modeled through momentum point-sources based on the net reaction of forces exerted on the bubble by the fluid. In volumetric coupling, in addition to this momentum point-source, the local variations in the bubble (or fluid) volume fractions are accounted for modifying the continuity and momentum equations. With this formulation, the velocity field is no longer divergence free even in an incompressible fluid owing to presence of discrete bubbles.

The two approaches were used to study bubble-ring interactions by varying the bubble size ($300 \leq d_b \leq 1300$) and vortex strengths ($\Gamma_0 = 0.0159, 0.0207, 0.0254$ m^2/s). It was found that the two-way coupling point-particle approach was insufficient to reproduce the experimental observations for bubble settling location, bubble escape properties, vortex core deformation and core fragmentation even with the use of experimentally determined lift coefficients [4]. The volumetric coupling approach performed well in reproducing these observations for both the bubble and liquid phases. It was shown that even for low volume loadings, a small

number of bubbles entrained in a vortex ring can significantly alter the vortex core for certain combination of the vortex strengths and bubble sizes. The bubbles were able to fragment the vortex core so as to increase the vorticity at the core center, similar to experimental observations. For the weak vortex strength, the entrained bubbles also escape from the plane of injection along the vortex ring, with the larger bubbles showing more escape. The distortion of the vortex ring was found to be significant for the weak vortex case, when medium size bubbles were entrained between 20-40% of the core radius. Bubbles that are entrained too close to the vortex core resulted in significantly less distortion.

The distortion of the vortex structure owing to bubbles is attributed to the fluid volume displacement due to bubble motion. The bubbles, once entrained in the vortex ring, nearly settle at a mean position away from the vortex core, owing to the balance between the drag, lift, pressure, and added mass forces. Once settled, the bubble do not experience any appreciable acceleration to exert a strong momentum coupling force and thus the point-source two-way coupling model does not affect the vortex ring structure. It was shown that the local displacement of the fluid due to bubbles tends to alter the vortex ring structure, distorting it completely for certain cases. These volume displacement effects were found to be critical in reproducing experimental observations.

A method for isolating volume displacement effects was derived in detail from the momentum equations by introducing the notion of a volumetric force on the fluid. This force was shown to have contributions from the local pressure gradient, the unsteady and inertial terms, viscous terms due to local variations in the fluid

volume fraction, the interphase momentum exchange, the hydrostatic force, and the local flow divergence owing to the volume displaced by the bubbles. The magnitudes of these individual forces were compared with the individual forces on the bubble, namely, drag, lift, added mass and pressure, to show that they were on the same order; however, the net contribution was also large unlike the balance among the forces on the bubble. The contribution due to the flow divergence was found to be the most dominant mechanism in distorting the vortex core. The volumetric force was also compared with analytical estimate of this force based on a two-dimensional symmetric Gaussian vortex to show good correlation for the strong as well as weak vortices which showed minimal bubble escape from the plane of injection. For cases with large distortion of the vortex core, the three-dimensional bubble escape and unsteady effects were found to be important.

The volumetric forces, when non-dimensionalized by the measure of hydrodynamic pressure force $(\rho_\ell \Gamma_0^2)$, showed direct dependence on the non-dimensional bubble settling location, r_s/r_c, as well as the vortex Reynolds number, $Re_{vx} = \Gamma_0/\nu_\ell$. The reaction force normalized by $\rho_\ell \Gamma_0^2 Re_{vx}^2$ collapsed onto a single curve showing strong correlation with the settling location. The magnitude of the normalized reaction force increased monotonically with the bubble settling location, indicating that the volume displacement effects, and hence vortex distortion potential, were large if the bubbles settled further away from the vortex core. The direction of the net resultant force was found to be aligned at roughly 45° in the bubble settling plane, r_s-θ_s, which explains the elongation of the vortex core, seen in experimental results and this work, in this direction.

This work has established the need for the inclusion of the volume displacement effects, due to motion of a disperse phase even for a dilute volume loading, to properly model the two-phase interactions. It is shown that for subgrid particles where the finite-size effects are important but conducting fully resolved simulations is not realistic ($0.1 < d_b/\Delta_{\mathrm{cv}} < 1$ and $St_b > 0.1$), accounting for local variations in bubble volume fractions can provide a practical and improved approach to standard two-way point-particle method.

An effort to classify the relative contributions of volume displacement effects and momentum coupling effects was undertook. It was noted that this force ratio is perhaps most dependent on the system, i.e. wall bounded or boundary-free, the orientation of gravity, etc., and secondarily on the Stokes number of the dispersed phase. Utilizing Taylor-Green vortices, a case with a consistent fluid acceleration, predicted large differences in the force ratio as the density ratio changed. More work should be undertaken in the future to more rigorously establish the criteria under which these volume displacement effects become important.

7.2   Outlook

There are many places to build upon this work, one in particular is discussed in this section. A method for more efficiently simulating volume displacement effects in multiphase flows is proposed here. To account for the volumetric displacements, the formulation presented here involves modification to the continuity and momentum equations. The fluid flow solver algorithm has to be modified considerably to

account for the local variations in volume fractions and a variable-density like pressure based formulation is needed. The pressure Poisson equation has a source term due to variations in the local volume fractions and the flow field is no longer divergence free. This can cause convergence issues in regions of large variations in volume fractions or for densely loaded systems.

A simplified approach that retains some of the main features of the volumetric coupling can be obtained for dilute loadings such that considerable changes to the basic incompressible flow solver are not needed. If the size of the dispersed phase is assumed small compared to the grid size (as in the cases studied in this work), the volumetric coupling reaction force in the momentum equation 5.11 can be accounted for as a volumetric source term in the momentum equation, in addition to the two-way coupling point source.

Starting with equation 5.11, dividing throughout by θ_ℓ, expanding the viscous term using product rule, and subtracting from this the one-way coupling equation 5.12 with a volumetric source term $(\widehat{\Delta \mathbf{V}})$ we get,

$$
\begin{align}
\widehat{\Delta \mathbf{V}} &= \frac{1}{\theta_\ell}\mathbf{f}_{b\to\ell} + \rho_\ell(\mathbf{u}_\ell\nabla\cdot\mathbf{u}_\ell) + \frac{1}{\theta_\ell}\left(\mu_\ell(\nabla\mathbf{u}_\ell + \nabla\mathbf{u}_\ell^T)\right)\cdot\nabla\theta_\ell \tag{7.1}\\
&= \frac{1}{\theta_\ell}\mathbf{f}_{b\to\ell} - \frac{\rho_\ell\mathbf{u}_\ell}{\theta_\ell}\left(\frac{\partial\theta_\ell}{\partial t} + \mathbf{u}_\ell\cdot\nabla\theta_\ell\right) + \mu_\ell\left(\nabla\mathbf{u}_\ell + \nabla\mathbf{u}_\ell^T\right)\cdot\frac{1}{\theta_\ell}\nabla\theta_\ell \tag{7.2}\\
&= \underbrace{\frac{1}{\theta_\ell}\mathbf{f}_{b\to\ell}}_{\text{I}} - \underbrace{\rho_\ell\mathbf{u}_\ell\frac{\mathrm{D}}{\mathrm{Dt}}(\ln\theta_\ell)}_{\text{II}} + \underbrace{\mu_\ell(\nabla\mathbf{u}_\ell + \nabla\mathbf{u}_\ell^T)\cdot\nabla(\ln\theta_\ell)}_{\text{III}}, \tag{7.3}
\end{align}
$$

where the velocity divergence is replaced by the material rate of change of the fluid volume fraction from the continuity equation 3.13.

This shows that the volumetric coupling forces can be obtained by simply dividing the two-way coupling momentum point-source by the local fluid volume fraction (term I), and adding two additional volumetric sources based on the local variations in the fluid volume fractions (terms II and III). The term II involves the local temporal and spatial variations in the volume fractions caused by motion of the bubbles. The third term represents modification of the viscous effects due to local variations in the volume fraction. For high Reynolds numbers, this viscous effect may be small compared to the other terms and may be neglected. Note that the last two terms are written as derivatives of the logarithm of the volume fraction. Owing to the Lagrangian nature of the bubbles, the source terms due to volume fraction variations can vary rapidly from one cell to another. Derivatives of the logarithm of the volume fraction will be smoother compared to the derivatives of the volume fraction field itself. The standard Lagrangian point-particle approach can now be easily modified by modeling the net reaction source this way. If the effects of bubbles on the continuity equation are neglected, the basic fluid flow solver used in these approaches will remain unchanged.

The above equation indicates that, for small bubbles ($d_b/\Delta_{cv} << 1$, $\theta_\ell \to 1$), the variations in the local volume fractions will be small and terms II and III will be negligible. The standard two-way coupling point-source is then recovered in a consistent manner. Depending upon the application, the dominant reaction term could be because of the net acceleration of bubbles (term I) or displacement of the fluid due to bubble motions (term II). This may in general depend on the dispersed phase volume loading, the particle Stokes number, particle to fluid density ratio,

the flow Reynolds number, orientation of gravity, and boundary conditions/effects.

For denser-than-fluid particle systems where the particle-to-fluid density ratio is small (for example sediment transport, liquid fluidized beds and risers etc.) the volumetric displacement effects can be large compared to the standard two-way point-source. Even for large density ratios, in regions where the subgrid particles are nearly in equilibrium with the fluid (reached terminal velocity), such as in the near wall region, the volume displacement effects may become important, and should be considered. To explore this formulation, the augmented momentum equation is solved with the volumetric force source term as shown in equation 7.4.

$$
\begin{aligned}
\rho_\ell \left(\frac{\partial \mathbf{u}_\ell}{\partial t} + \nabla \cdot (\mathbf{u}_\ell \mathbf{u}_\ell) \right) &= -\nabla p + \nabla \cdot [\mu_\ell (\nabla \mathbf{u}_\ell + \nabla \mathbf{u}_\ell^T)] - \rho_\ell \mathbf{g} + \frac{1}{\theta_\ell} \mathbf{f}_{b \to \ell} \\
&- \rho_\ell \mathbf{u}_\ell \frac{\mathrm{D}}{\mathrm{Dt}} (\ln(\theta_\ell)) + \mu_\ell (\nabla \mathbf{u}_\ell + \nabla \mathbf{u}_\ell^T) \cdot \nabla (\ln(\theta_\ell)). \quad (7.4)
\end{aligned}
$$

$$
\frac{\partial}{\partial t} (\rho_\ell) + \nabla \cdot (\rho_\ell \mathbf{u}_\ell) = 0, \tag{7.5}
$$

Continuity is enforced in the classic sense, without the divergent effect taken into account. The traditional conservation of mass equation is given in 7.5. Ideally, by including the volumetric force source term, the proper momentum should be predicted. Although the enforcement of conservation of mass will remove the divergence from the flow field, the important features of momentum augmentation by the source term should remain in the flow field. While enforcing continuity like

this may diminish some of the effect on the carrier phase flow, there are many additional possibilities for how to handle these issues. A series of case studies should be undertook to evaluate the relative strengths and weaknesses of utilizing this approach.

APPENDICES

Appendix A – Taylor-Vortex Case

Three validation cases are presented to show that the mathematical models described above as well as the numerical implementation are working properly. The first case is a simple test problem with a known analytical solution, the Taylor vortex case. This case demonstrates the solvers second order spatial accuracy. The second is the turbulent channel flow case on Kim, Moin and Moser (1987) [83] which will demonstrate the solvers ability to perform large-eddy simulation and accurately reproduce establish turbulent channel flow results.
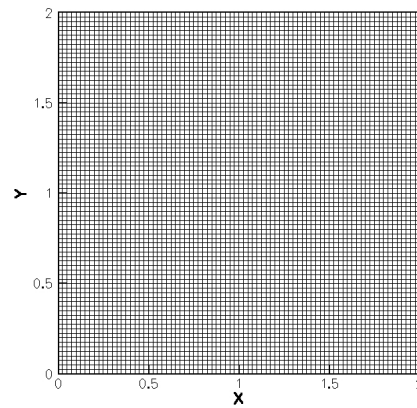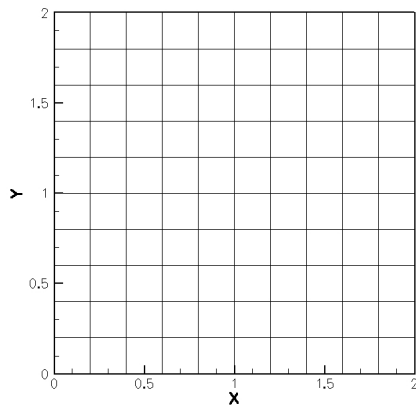
Figure A.1: *Mesh for the coarse grid Taylor-Vortex case.*

Figure A.2: *Mesh for the resolved grid Taylor-Vortex case.*

$$u(x, y, t) \quad = \quad -cos(\pi x) sin(\pi y) e^{-2\pi^2 \nu t} \tag{A.1}$$

$$v(x, y, t) \quad = \quad sin(\pi x) cos(\pi y) e^{-2\pi^2 \nu t} \tag{A.2}$$

$$p(x, y, t) \quad = \quad -0.25(cos(\pi x) + cos(2\pi y)) e^{-4\pi^2 \nu t} \tag{A.3}$$

The Taylor-Vortex case utilizes a known analytical solution to a simple physical situation for the Navier-Stokes equations. To measure the accuracy of the solver this case is set up and ran in order to measure the error between the computed temporal development of the flow (i.e. eddy decay) versus what is predicted by the analytical solution. The analytic solution is given here in equations (A.1), (A.2) and (A.3).
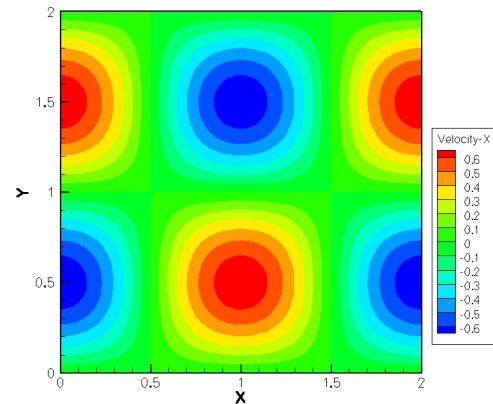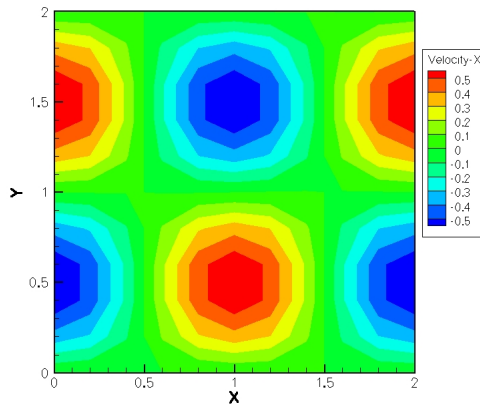
Figure A.3: *Coarse Grid - $\hat{x}$ Velocity.*   Figure A.4: *Resolved Grid - $\hat{x}$ Velocity.*

The exponential term provides an initial condition (at $t = 0s$) and a final solution, which in this case is at $t = 0.2s$. The simulation is ran with four different grid
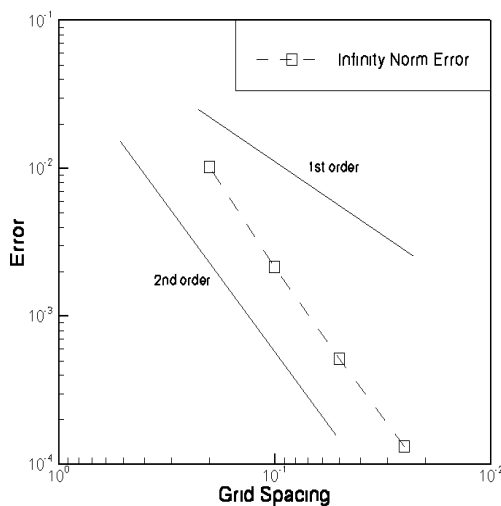
Figure A.5: L_∞ norm error. Lines indicate $1st$ and $2nd$ order error for reference.

spacings, each with an appropriate time step in order to keep the CFL (Courant–Friedrichs–Lewy) number constant. The four mesh spacings and time steps are $\Delta x = 0.2, 0.1, 0.05, 0.025$ and $\Delta t = 0.02, 0.01, 0.005, 0.0025$. The various relevant constants are set as follows; $\nu = 0.1$, $\rho = 1$ with a Reynolds number of 10.

The grids used for the least and most resolved cases are shown in figures A.1 and A.2. The refinement difference is clear, this should give the reader a fair idea of what to expect as far as accuracy.

Figures A.3 and A.4 are the $\hat{u}$ velocity components for the least and most resolved cases respectively. The eddy structures are quite apparent in these images. The meat of what we care about though is the overall accuracy of the solver, and its order associated with grid resolution.

Reference lines for $1st$ and $2nd$ order accuracy are placed on figure A.5. This figure shows the four error values corresponding to the four varying grid resolution cases detailed above. The infinity norm error is used for this, which is the maximum error at any point in the domain over the course of the simulation. The conclusion is that the solver is approximately $2nd$ order accurate spatially.

Appendix B – Turbulent Channel Flow

The Taylor-Vortex study showcased the codes ability to accurately solve fluid flow problems under simple circumstances. There is however, something more to be shown here. Somewhere buried within the convective terms of the Navier-Stokes Equations is the mainstay of turbulence, non-linear motion. These facets must interact harmoniously with the viscous terms to create a system where a delicate balance is created. The largest eddys must input energy and transfer them to smaller eddies and so on until ultimately viscous effects take over and win out. There are some numerical issues here that are less straight forward than some other cases, in particular the handling of these nonlinear terms. If there had been some small bungling of these terms it may not have shown up well in the Taylor-Vortex case, however a turbulent channel flow is a more difficult case study for a problem such as this to hide. We compare our results to that of the direct numerical simulation study of Kim, Moin and Moser (1987) [83].

Table B.1: Turbulent Channel Flow - Computational Parameters

Parameter	Value
Computational Domain	4π x 2 x 2π
Fluid Viscosity (μ)	0.0070303 kg/ms
Fluid Density (ρ)	1.0 kg/m^3
Reynolds Number (Re_τ)	180
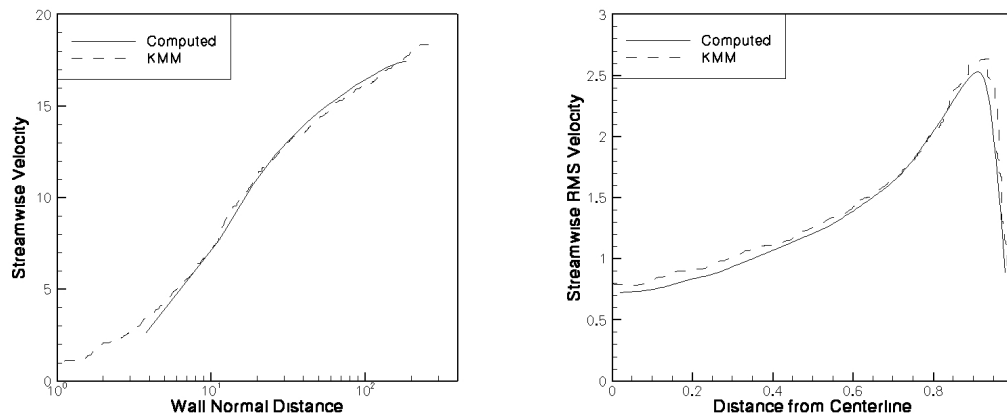
(a) *Mean Streamwise Gas Velocity for the* (b) *Streamwise RMS Velocity for the tur-*
turbulent channel flow case, $Re_\tau = 180$. *bulent channel flow case,* $Re_\tau = 180$.

The channel is forced using a constant mass flow rate forcing to maintain a bulk steamwise velocity of $20 m/s$. At each time step the body force, which is representing a fictitious pressure gradient, is computed that is needed to achieve this overall bulk velocity, which is directly proportional to the mass flow rate. The flow is ran until it reaches a statistically steady state before statistical data is collected. The determination of when a statistically steady state occurs is based on two features. First the variations in the bulk flow rate become very small, which happens almost immediately. Secondly the wall slip velocity u_τ is also tracked until it reaches its final value for a prolonged period of time.

The first set of figures shows the mean streamwise fluid velocity and the streamwise root mean square velocity. While our simulation is done using large eddy simulation instead of direct numerical simulation, it is shows that the agreement is quite good. Most of the perceived error on the graphics is due to the authors
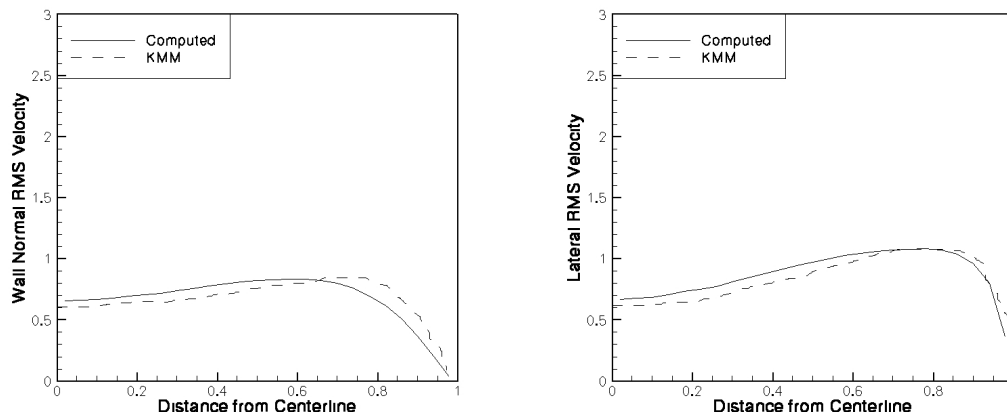
(c) *Wall Normal RMS Velocity for the turbulent channel flow case , $Re_\tau = 180$.*

(d) *Lateral RMS Velocity for the turbulent channel flow case, $Re_\tau = 180$.*

inability to trace the validation results concisely.

As with the streamwise root mean square velocities, both the lateral and wall normal rms velocities show good agreement with the provided data. This would seem to indicate that the numerical method given previously can adequately handle the convective terms. This capability of accurately simulating single phase turbulent is key for large eddy simulation to be able to handle particle laden flows as well as oxy-combustion. You may recall that the main reason Reynolds averaged Navier-Stokes models generally fail for particle laden flows within interesting domains is their inability to adequately handle the carrier phase motions, thus leading to physically inaccurate particle motion.

Many turbulent flow studies focus on a wall slip Reynolds number of $Re_\tau = 180$. It is important to show that the code is capable of handling higher Reynolds number flows adequately. The fundamental features of turbulent flows can change
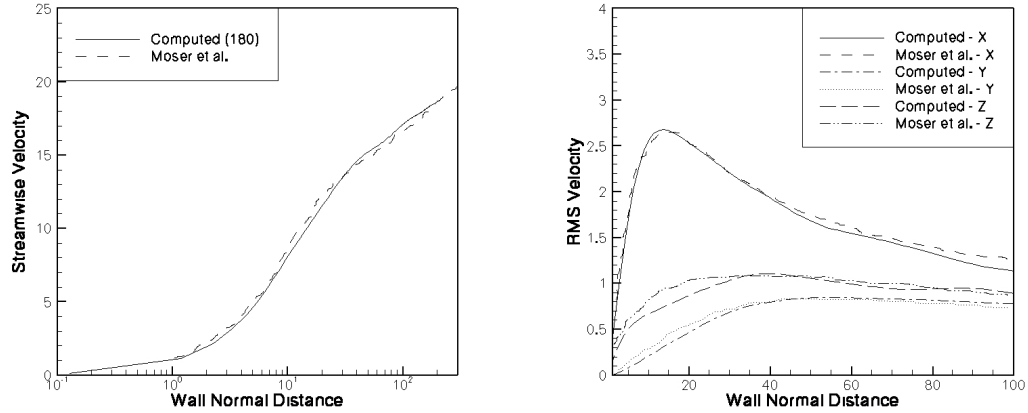
(e) *Mean Streamwise Velocity for the varying Reynolds number case, $Re_\tau = 180$.*

(f) *Streamwise RMS Velocity for the varying Reynolds number case, $Re_\tau = 180$.*

with Reynolds number, for example how production and dissipation interact and in what quantities. If features such as this are not properly handles inaccurate quantities will be predicted for the turbulent intensity, thus the root-mean-square velocities of the fluid. These cases are interesting because the selection of parameters is somewhat arbitrary as long as the Reynolds number is appropriate. For these studies a viscosity of $\mu = 0.0070303$ kg/ms and a density of $\rho = 1.0$ kg/m^3 were used. A constant pressure gradient forcing is used to enforce the given Reynolds numbers. This is done through a method detailed in the results section in which the pressure gradient needed in supplied as a fictitious body force into each control volume. The needed body force is calculated based on the expected drag at the walls of the channel, this loss must be balanced by the body force. The balance that is struck is the driving force behind the flow rate and flow structure of the domain.
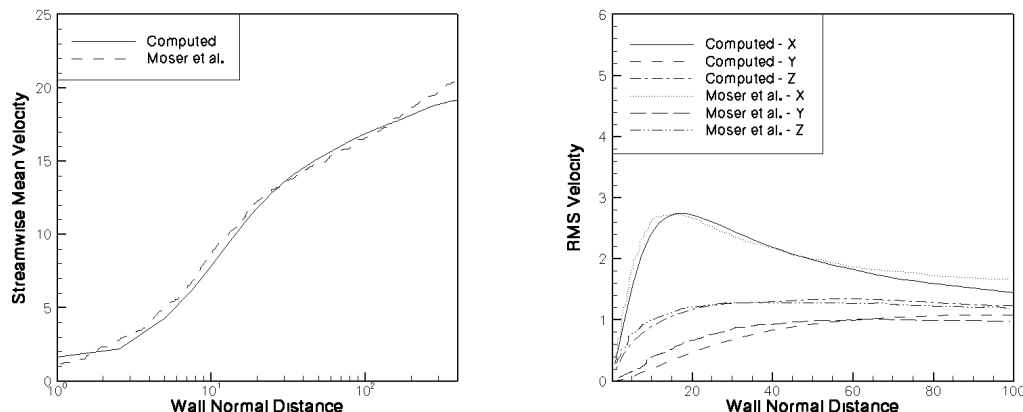
(g) *Mean Streamwise Velocity for the vary-ing Reynolds number case, $Re_\tau = 395$.*

(h) *Streamwise RMS Velocity for the vary-ing Reynolds number case, $Re_\tau = 395$.*

Figures B.1(e) and B.1(f) show, similar to the last validation case, that the code can adequately reproduce the features of low Reynolds number turbulence. This is not new. To show that higher Reynolds numbers can be handled we look to the next set of figures. In these figures, B.1(g) and B.1(h), we can see that $Re_\tau = 395$ turbulence is handled adequately as well.

Lastly we look to figures B.1(i) and B.1(j) to demonstrate that the highest Reynolds number turbulence in this study are also handled well. These figures show information for $Re_\tau = 590$. This case is somewhat vital as the turbulent particle-laden channel flow case presented in the results section has a Reynolds number of $Re_\tau = 644$.

Our results seem to agree well with those of Moser et al. (1999) [84]. This is a demonstration that the code scales well with increasing Reynolds number and predicts the proper flow features. The edges and slight jumps in the data are due
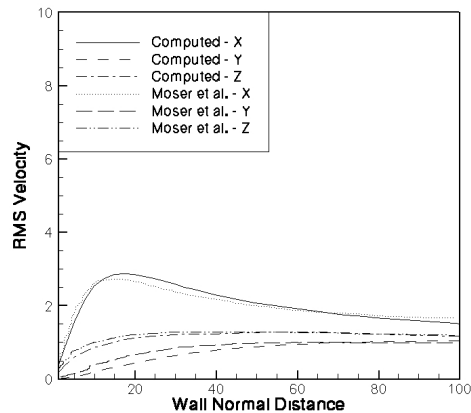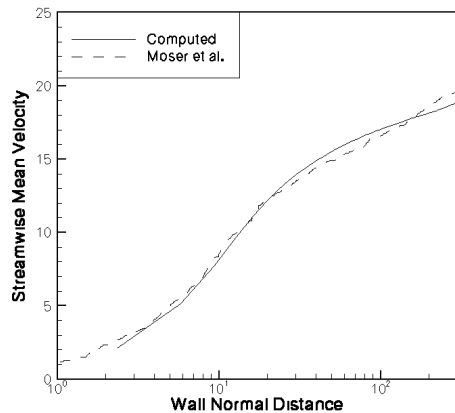
(i) *Mean Streamwise Velocity for the varying Reynolds number case, $Re_\tau = 590$.*

(j) *Streamwise RMS Velocity for the varying Reynolds number case, $Re_\tau = 590$.*

to the author having trouble ripping the data from the paper with the precision necessary to maintain the smooth curves in the paper.

Appendix C – Crossing Particle Jets

A main case of interest is that of a particle laden jet. Here the inter-particle collision model is validated using a dense particle jet and a dilute particle jet as test cases. This case is examined by Lostec et al. (2008) [85] for various collision models.

Where the Stokes number and Knudsen number are defined as:

$$St = 2\rho_p r_p^2/9\mu_f \tag{C.1}$$

$$Kn = 1/4\sqrt{2}ned_p \tag{C.2}$$

In the case of the dilute jet we are expecting to see minimal interaction between the particle jets as both only contain intermitent particles, it would certainly be a stretch to call either a stream. Figure C.1 shows isocontours of particle volume fraction, the contour values themsevles are unimportant as the individual particle locations are actually quite clear. Figure C.2 shows a flood contour map of the same features. As was desired we see that there is little to no noticable variance in the jet path due to the crossing trajectories. This is desireable for obvious reasons, however it was not entirely clear beforehand how well the collision model would perform. The model is designed to handle dense flows, not dilute ones. The inter-

Table C.1: Crossing Particle Jets - Computational Parameters

Parameter	Value
Computational Domain	1 x 1 x 0.2
Stokes Number - Dilute	0.01
Knudsen Number - Dilute	10
Stokes Number - Dense	1.0
Knudsen Number - Dense	0.1
Jet Velocity	1.0 m/s
Jet Width	0.1 m

particle repulsion force applied could have hypothetically derailed the jets even at such a low Knudsen number, however, these worries appear to be unfounded.
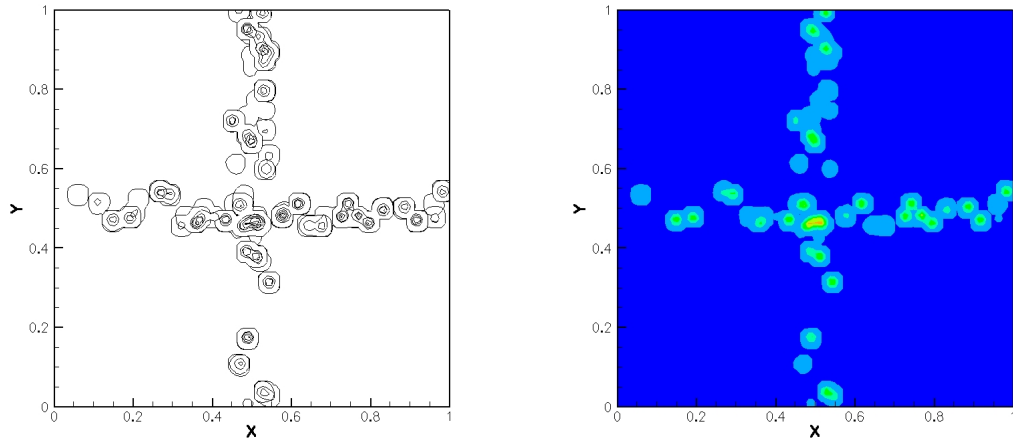
Figure C.1: *Dilute jet case: Particle volume fraction contours*

Figure C.2: *Dilute jet case: Particle volume fraction contour flood map*

While its comforting to know that the dilute jet case behaves properly, it is more important that the dense jet behaves properly as the pertinent flows are relatively dense. In this case the set up is the same as before but with a Knudsen

number of 0.1. The desired behavior for this case is that the two jets meet in the middle and form a unified jet.
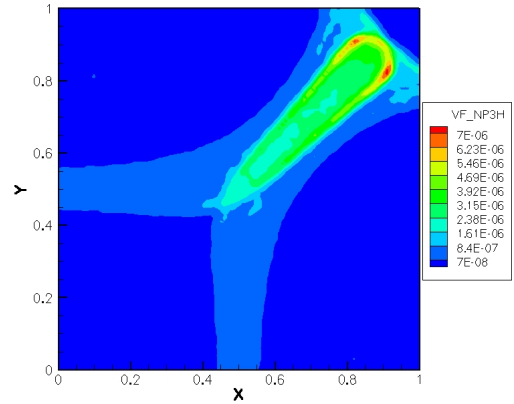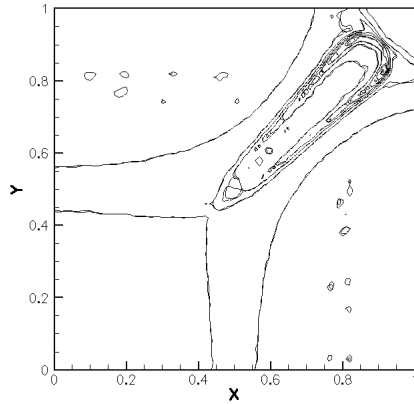
Figure C.3: *Dense jet case: Particle volume fraction contours*

Figure C.4: *Dense jet case: Particle volume fraction contour flood map*

As we can see in both figures C.3 and C.4 the two dense jets have a sufficient concentration that few if any particles escape the crossing, thus all particles are subject to influence from the opposing jet. The mean jet formed slowly expands due to the interparticle repulsion forces and non-uniform collision effects. A few particles stray out of the mean stream when these inter-particle forces become highly unbalanced. Since the particles are injected randomly there will be occasional times and places where the jets arent quite uniform and cause these lopsided effects.

Appendix D – Bubble Settling in a Line Vortex

To validate the solver for the type of work studied here, this section will focus on bubble entrainment in a line vortex. The velocity and pressure profiles are specified at $t = 0$, see equations D.1 and D.2, where Γ is the vortex circulation, r_c is the core radius u_θ is the azimuthal velocity component and P_∞ is a reference pressure. The vortex is then allowed to decay with time.

$$u_\theta(r) = \frac{\Gamma r}{2\pi r_c^2} \tag{D.1}$$

$$P(r) = P_\infty - \frac{\rho \Gamma^2}{4\pi^2 r_c^2} + \frac{\rho \Gamma^2 r^2}{8\pi^2 r_c^4} \tag{D.2}$$

As shown in the force balance diagram shown in figure D.2(a), the forces contributing to the settling location, see figure 5.1(b), of a bubble are direction dependent. In the azimuthal direction the buoyancy, lift, dynamic pressure and added mass forces are in balance, whereas in the radially outward direction the buoyancy, hydrostatic pressure and drag are in balance, per equations D.3 and D.4.

$$(\mathbf{F}_g + \mathbf{F}_{pH})cos(\theta_s) = \mathbf{F}_d \tag{D.3}$$

$$\mathbf{F}_b sin(\theta_s) + \mathbf{F}_\ell = \mathbf{F}_{pD}0 + \mathbf{F}_{am} \tag{D.4}$$
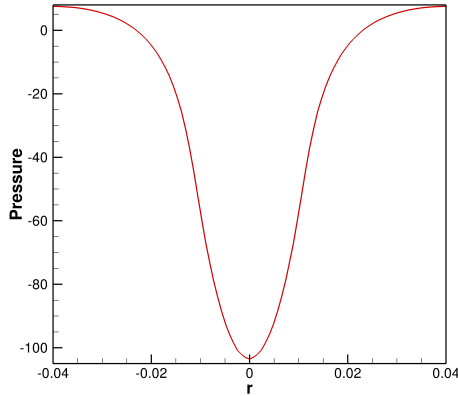
Figure D.1: Line vortex pressure profile.

The equations for the forces, previously given in section 3.1, are algebraically rearranged to isolate θ_s and r_s, the bubble settling coordinates relative to the vortex core center, yielding equations D.5 and D.6. The equations for θ_s and r_s are inseperable, so they must be solved as a coupled system.

$$\theta_s = cos^{-1}\left(\frac{3C_d u_\theta^2}{4d_g \mathbf{g}\left(\frac{\rho_b}{\rho_\ell} - 1\right)}\right) \tag{D.5}$$

$$r_s = \frac{(1 + C_{am})u_\theta^2}{\left(\frac{\rho_b}{\rho_\ell} - 1\right)\mathbf{g}sin(\theta_s) + C_\ell u_\theta \omega} \tag{D.6}$$

These equations are then checked iteratively outward from the core to find a settling location based on radial distance from the core center and angle from the horizontal. The settling locations obtained are for two different strength vortices $\Gamma_0 = 0.015m^2/s$ and $\Gamma_0 = 0.025m^2/s$ and for five bubble sizes between 300 and

(a) Line vortex pressure profile

(b) Bubble settling locations
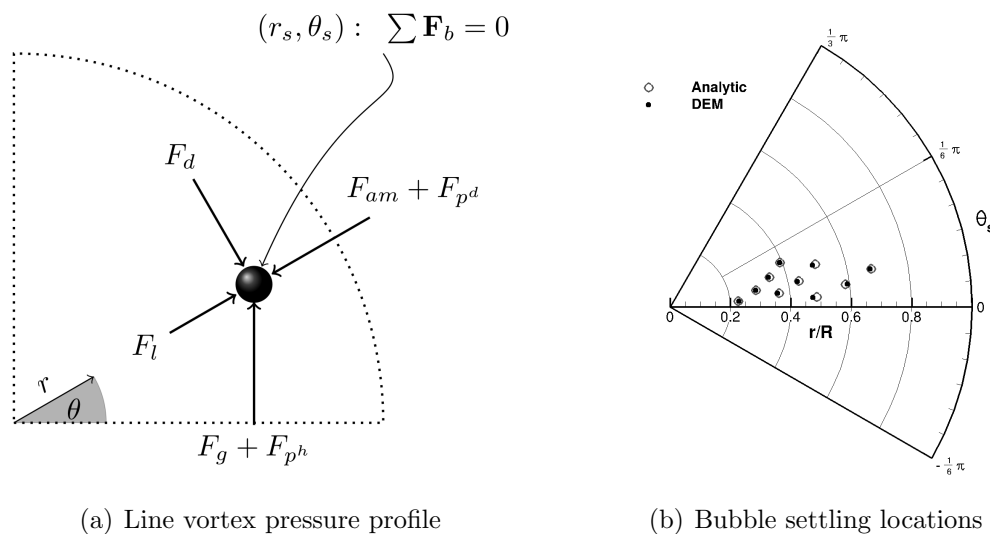
Figure D.2: Comparison of the analytic solution for the bubble settling location with the settling location predicted by the discrete element method (DEM) solver.

$1100\mu m$. Figure D.1 shows the relative pressure within the line vortex core. The settling locations predicted by the analytical method mentioned previously are compared to the settling locations found by running a one-way coupled simulation of bubble entrainment into a line vortex, as shown in figure D.2(b).

As the bubble entrains within the vortex it circulates until reaching its settling location. In this case very little bubble motion is evident once this position is reached, this demonstrates the accuracy of the particle's coupling to the fluid. The small differences predicted between the analytical and computational solutions are likely due to two factors. First, the force balance assumed, which is a good approximation, not a strict interpretation of reality. Second, a slight decay occurs within the vortex during the time it takes for the bubble to settle.

Appendix E – Vortex Ring Grid Study

This section offers a short explanation of the choice of grid utilized. To begin with a grid convergence study was done to ensure the strength of the vortex ring remained nearly constant as it traveled downstream and the integrated vorticity profile (same computations as were done in section 5.4, out to the vortex core radius) converged with increasing grid resolution. Figure E.1 shows two sample grids used for the convergence study. Both feature additional resolution near the inlet and in the region of interest of the study, and less resolution in the areas where the vortex ring does not reach. In figure E.2(b) the integrated vorticity profile is plotted against the streamwise grid spacing to show that the vortex profile converges with increasing resolution. The underresolved grids perform poorly because they do not sufficiently capture the inlet condition in order to allow the shear layer roll up to be properly handled.

While the grid converges well at the highest resolutions, one feature of this model should be noted. Since we are studying the behavior of bubbles whos volume is nearly that of the grid cells, additional resolution is not possible without changing some parameters of the system, such as the interpolation kernal. This is not desireable and exactly what makes this type of study so important. The need to develop a better understand of how these models perform when pushed to their limits is essential to the development of computationally efficient two-phase
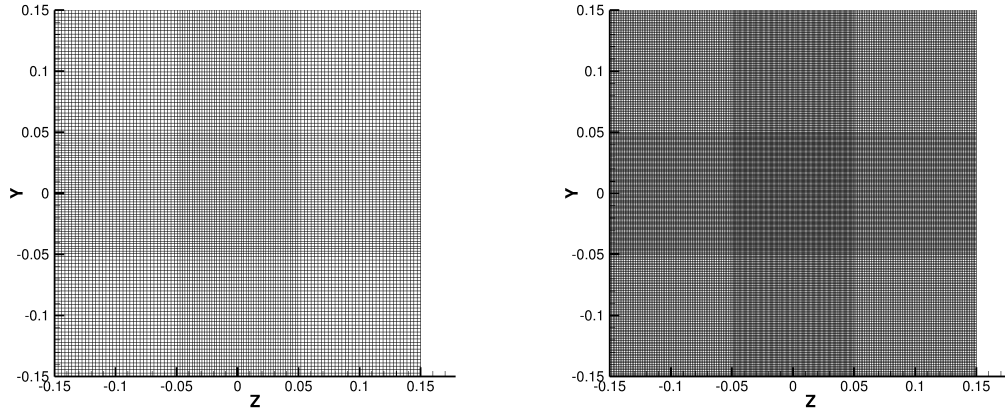
(a) Cross-section of underresolved grid.　　　(b) Cross-section of resolved grid

Figure E.1: Sample cross-sections of grids used for grid convergence study

flow Eulerian-Lagrangian models. In addition to the cartesian grid study, additional grids were made resolving the circular inlet condition with unstructured hex elements to follow the inlet cross-section, for an example of these unstructured grids see figure E.2(a). It was verified that when the grid is sufficiently resolved, the same vortex ring profile is generated with each grid. Thus the approximation of the circular inlet by small square cells works well, but only when sufficiently resolved.

Utilizing the error estimate method outlined in [86] the GCI for the fine grid calculation is found, as in equation E.1.

$$GCI(\mathbf{x}) = F_s \left| \frac{\phi_1 - \phi_2}{(r^2 - 1)} \right| \tag{E.1}$$

Using this equation with $F_s = 1.25$, as is appropriate for a fine grid estimate
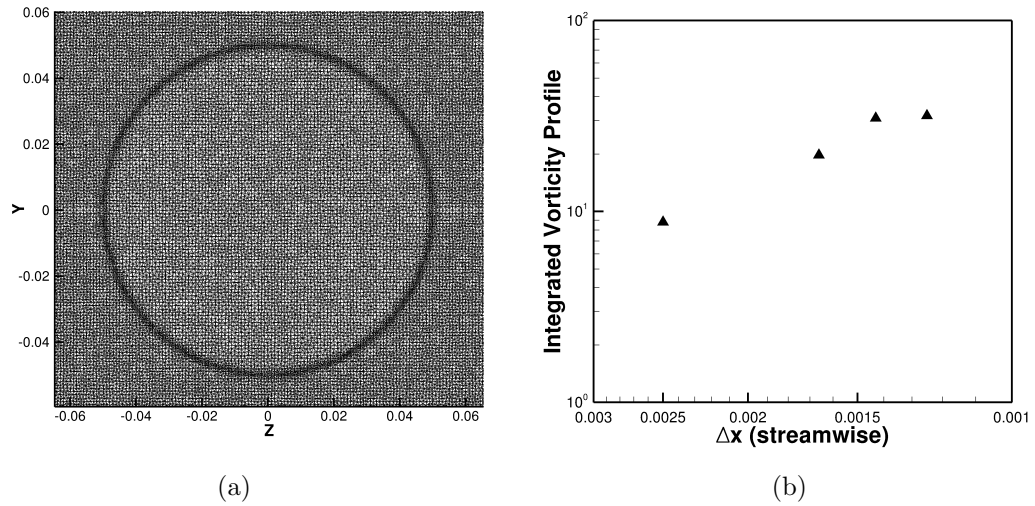
Figure E.2: (a) Cross-section of unstructured grid inlet. (b) Convergence of integrated vorticity profile.

[87], it is found that the conservative error estimate is 11.48% based on the circulation of the vortex ring within the core radius.

Bibliography

[1] Balachandar, S., 2009, "A scaling analysis for pointparticle approaches to turbulent multiphase flows," International Journal of Multiphase Flow, **35**(9), pp. 801–810.

[2] Balachandar, S. and Eaton, J. K., 2010, "Turbulent dispersed multiphase flow," Annual Review of Fluid Mechanics, **42**(1), pp. 111–133.

[3] Elghobashi, S., 2006, "An updated classification map of Particle-Laden turbulent flows," *IUTAM Symposium on Computational Approaches to Multiphase Flow*, vol. 81, Springer Netherlands, Dordrecht, pp. 3–10.

[4] Sridhar, G. and Katz, J., 1999, "Effect of entrained bubbles on the structure of vortex rings," Journal of Fluid Mechanics, **397**, pp. 171–202.

[5] Ceccio, S. L., 2010, "Friction drag reduction of external flows with bubble and gas injection," Annual Review of Fluid Mechanics, **42**(1), pp. 183–203.

[6] Sokolichin, A., Eigenberger, G., Lapin, A., and Lbert, A., 1997, "Dynamic numerical simulation of gas-liquid two-phase flows Euler/Euler versus Euler/Lagrange," Chemical Engineering Science, **52**(4), pp. 611–626.

[7] van der Hoef, M., van Sint Annaland, M., Deen, N., and Kuipers, J., 2008, "Numerical simulation of dense Gas-Solid fluidized beds: A multiscale modeling strategy," Annual Review of Fluid Mechanics, **40**(1), pp. 47–70.

[8] Hsiao, C. and Chahine, G., 2004, "Prediction of tip vortex cavitation inception using coupled spherical and nonspherical bubble models and Navier-Stokes computations," Journal of Marine Science and Technology, **8**(3), pp. 99–108.

[9] Higuera, F., 2004, "Axisymmetric inviscid interaction of a bubble and a vortex ring," **16**, p. 1156.

[10] Ferry, J. and Balachandar, S., 2001, "A fast eulerian method for disperse two-phase flow," International Journal of Multiphase Flow, **27**(7), pp. 1199–1226.

[11] Druzhinin, O. A. and Elghobashi, S., 1998, "Direct numerical simulations of bubble-laden turbulent flows using the two-fluid formulation," Physics of Fluids, **10**(3), p. 685.

[12] FeVrier, P., Simonin, O., and Squires, K. D., 2005, "Partitioning of particle velocities in gassolid turbulent flows into a continuous field and a spatially uncorrelated random distribution: theoretical formalism and numerical study," Journal of Fluid Mechanics, **533**.

[13] Maxey, M. R., 1987, "The gravitational settling of aerosol particles in homogeneous turbulence and random flow fields," Journal of Fluid Mechanics, **174**(1), p. 441.

[14] Squires, K. D. and Eaton, J. K., 1991, "Preferential concentration of particles by turbulence," Physics of Fluids A: Fluid Dynamics, **3**(5), p. 1169.

[15] Elghobashi, S., 1991, "Particle-laden turbulent flows: direct simulation and closure models," Applied Scientific Research, **48**(3-4), pp. 301–314.

[16] Elghobashi, S., 1994, "On predicting particle-laden turbulent flows," Applied Scientific Research, **52**(4), pp. 309–329.

[17] Reade, W. C. and Collins, L. R., 2000, "Effect of preferential concentration on turbulent collision rates," Physics of Fluids, **12**(10), p. 2530.

[18] Rouson, D. and Eaton, J., 2001, "On the preferential concestration of solid particles in turbulent channel flow," Journal of Fluid Mechanics, **428**, pp. 149–169.

[19] Xu, J., Maxey, M., and Karniadakis, G., 2002, "Numerical simulation of turbulent drag reduction using micro-bubbles," Journal of Fluid Mechanics, **468**, pp. 271–281.

[20] Li, Y., McLaughlin, J. B., Kontomaris, K., and Portela, L., 2001, "Numerical simulation of particle-laden turbulent channel flow," Physics of Fluids, **13**(10), p. 2957.

[21] Armenio, V. and Fiorotto, V., 2001, "The importance of the forces acting on particles in turbulent flows," Physics of Fluids, **13**(8), p. 2437.

[22] Vreman, A. W., 2007, "Turbulence characteristics of particle-laden pipe flow," Journal of Fluid Mechanics, **584**, p. 235.

[23] Wang, Q. and Squires, K., 1996, "Large eddy simulation of particle deposition in a vertical turbulent channel flow," International Journal of Multiphase Flow, **22**(4), pp. 667–683.

[24] Apte, S., Mahesh, K., Moin, P., and Oefelein, J., 2003, "Large-eddy simulation of swirling particle-laden flows in a coaxial-jet combustor," International Journal of Multiphase Flow, **29**(8), pp. 1311–1331.

[25] Segura, J., "Predictive capabilities of particle-laden large eddy simulation," Ph.D. Thesis, Stanford University, p. 2004.

[26] Moin, P. and Apte, S., "Large-eddy simulation of realistic gas turbine combustors." AIAA Journal, **44**, p. 698.

[27] Sommerfeld, M., Ando, A., and Wennerberg, D., 1992, "Swirling, particle-laden flows through a pipe expansion," Journal of Fluids Engineering, **114**(4), pp. 648–656.

[28] Sommerfeld, M. and Qiu, H., 1993, "Characterization of particle-laden, confined swirling flows by phase-doppler anemometry and numerical calculation," International Journal of Multiphase Flow, **19**(6), pp. 1093–1127.

[29] Lain, S. and Garca, J., 2006, "Study of four-way coupling on turbulent particle-laden jet flows," Chemical Engineering Science, **61**(20), pp. 6775–6785.

[30] Yamamoto, Y., Potthoff, M., Tanaka, T., Kajishima, T., and Tsuji, Y., 2001, "Large-eddy simulation of turbulent gasparticle flow in a vertical channel: effect of considering inter-particle collisions," Journal of Fluid Mechanics, **442**.

[31] Shams, E., Finn, J., and Apte, S. V., 2011, "A numerical scheme for Euler-Lagrange simulation of bubbly flows in complex systems," International Journal for Numerical Methods in Fluids, **67**(12), pp. 1865–1898.

[32] Ferrante, A. and Elghobashi, S., 2005, "Reynolds number effect on drag reduction in a microbubble-laden spatially developing turbulent boundary layer," Journal of Fluid Mechanics, **543**(-1), p. 93.

[33] Ferrante, A. and Elghobashi, S., 2007, "On the accuracy of the two-fluid formulation in direct numerical simulation of bubble-laden turbulent boundary layers," Physics of Fluids, **19**(4), p. 045105.

[34] Ferrante, A. and Elghobashi, S. E., 2007, "On the effects of microbubbles on TaylorGreen vortex flow," Journal of Fluid Mechanics, **572**, p. 145.

[35] Finn, J., Shams, E., and Apte, S. V., 2011, "Modeling and simulation of multiple bubble entrainment and interactions with two dimensional vortical flows," Physics of Fluids, **23**(2), p. 023301.

[36] Apte, S., Mahesh, K., and Lundgren, T., 2008, "Accounting for finite-size effects in simulations of disperse particle-laden flows," International Journal of Multiphase Flow, **34**(3), pp. 260–271.

[37] Crowe, C. T., Troutt, T. R., and Chung, J. N., 1996, "Numerical models for Two-Phase turbulent flows," Annual Review of Fluid Mechanics, **28**(1), pp. 11–43.

[38] Mandli, K., 2006, "Multiphase turbulent modeling using LES," .

[39] Pope, S. B., 2000, *Turbulent flows*, Cambridge University Press, Cambridge; New York.

[40] Maxey, M. R. and Riley, J., 1983, "Equation of motion for a small rigid sphere in a nonuniform flow," Physics of Fluids, **26**(4), p. 883.

[41] Tsuji, Y., 2007, "Multi-scale modeling of dense phase gasparticle flow," Chemical Engineering Science, **62**(13), pp. 3410–3418.

[42] Patankar, N. and Joseph, D., 2001, "Lagrangian numerical simulation of particulate flows," International Journal of Multiphase Flow, **27**(10), pp. 1685–1706.

[43] Patankar, N. and Joseph, D., 2001, "Modeling and numerical simulation of particulate flows by the EulerianLagrangian approach," International Journal of Multiphase Flow, **27**(10), pp. 1659–1684.

[44] Yu, Y., Zhou, L., Wang, B., and Cai, F., 2005, "A USM- two-phase turbulence model for simulating dense gas-particle flows," Acta Mechanica Sinica, **21**(3), pp. 228–234.

[45] Lun, C., 2000, "Numerical simulation of dilute turbulent gassolid flows," International Journal of Multiphase Flow, **26**(10), pp. 1707–1736.

[46] Lain, S. and Sommerfeld, M., 2003, "Turbulence modulation in dispersed two-phase flow laden with solids from a lagrangian perspective," International Journal of Heat and Fluid Flow, **24**(4), pp. 616–625.

[47] Q. Wang and Squires, K., 1996, "Large eddy simulation of particleladen turbulent channel flow," Physics of Fluids, **8**, p. 1207.

[48] Tang, X. and Wu, J., 2008, "An improved LES on dense Particle-Liquid turbulent flows using integrated boltzmann equations," The Canadian Journal of Chemical Engineering, **85**(2), pp. 137–150.

[49] Graham, D. and James, P., 1996, "Turbulent dispersion of particles using eddy interaction models," International Journal of Multiphase Flow, **22**(1), pp. 157–175.

[50] Uchiyama, T. and Fukase, A., 2006, "Vortex simulation of gas-particle two-phase compound round jet," Powder Technology, **165**(2), pp. 83–91.

[51] Deen, N., Van Der Hoef, Annaland, V. S., and Kuipers, J., 2007, "Numerical simulation of dense gas-particle flowsz using the EulerLagrange approach," Progress in Computational Fluid Dynamics, **7**(2).

[52] Maxey, M. R., Patel, B. K., Chang, E. J., and Wang, L., 1997, "Simulations of dispersed turbulent multiphase flow," Fluid Dynamics Research, **20**(1-6), pp. 143–156.

[53] Kuerten, J. G. M. and Vreman, A. W., 2005, "Can turbophoresis be predicted by large-eddy simulation?" Physics of Fluids, **17**(1), p. 011701.

[54] Wang, Q., Squires, K., Chen, M., and McLaughlin, J., 1997, "On the role of the lift force in turbulence simulations of particle deposition," International Journal of Multiphase Flow, **23**(4), pp. 749–763.

[55] Oweis, G. F., van der Hout, I. E., Iyer, C., Tryggvason, G., and Ceccio, S. L., 2005, "Capture and inception of bubbles near line vortices," Physics of Fluids, **17**(2), p. 022105.

[56] Rastello, M., Mari, J., and Lance, M., 2011, "Drag and lift forces on clean spherical and ellipsoidal bubbles in a solid-body rotating flow," Journal of Fluid Mechanics, **682**, pp. 434–459.

[57] Van Nierop, E. A., Luther, S., Bluemink, J. J., Magnaudet, J., Prosperetti, A., and Lohse, D., 2007, "Drag and lift forces on bubbles in a rotating flow," Journal of Fluid Mechanics, **571**, p. 439.

[58] Bluemink, J. J., Lohse, D., Prosperetti, A., and Van Wijngaarden, L., 2009, "Drag and lift forces on particles in a rotating flow," Journal of Fluid Mechanics, **643**, p. 1.

[59] Sridhar, G. and Katz, J., 1995, "Drag and lift forces on microscopic bubbles entrained by a vortex," Physics of Fluids, **7**(2), p. 389.

[60] Mazzitelli, I. M., Lohse, D., and Toschi, F., 2003, "The effect of microbubbles on developed turbulence," Physics of Fluids, **15**(1), p. L5.

[61] Deng, R., Wang, C., and Smith, K., 2006, "Bubble behavior in a taylor vortex," Physical Review E, **73**(3).

[62] Lohse, D. and Prosperetti, A., 2003, "Controlling bubbles," Journal of Physics: Condensed Matter, **15**(1), pp. S415–S420.

[63] Harper, J., 1972, "The motion of bubbles and drops through liquids," *Advances in Applied Mechanics*, vol. 12, Elsevier, pp. 59–129.

[64] Magnaudet, J. and Eames, I., 2000, "The motion of High-Reynolds-Number bubbles in inhomogeneous flows," Annual Review of Fluid Mechanics, **32**(1), pp. 659–708.

[65] Schiller, L. and Naumann, A., 1933, "A drag coefficient correlation," VDI Z., **77**(318).

[66] Merle, A., Legendre, D., and Magnaudet, J., 2005, "Forces on a high-Reynolds-number spherical bubble in a turbulent flow," Journal of Fluid Mechanics, **532**, pp. 53–62.

[67] Joseph, D., Lundgren, T., Jackson, R., and Saville, D., 1990, "Ensemble averaged and mixture theory equations for incompressible fluidparticle suspensions," International Journal of Multiphase Flow, **16**(1), pp. 35–42.

[68] Jackson, R., 1997, "Locally averaged equations of motion for a mixture of identical spherical particles and a newtonian fluid," Chemical Engineering Science, **52**(15), pp. 2457–2469.

[69] Zhang, D. and Prosperetti, A., 1997, "Momentum and energy equations for disperse two-phase flows and their closure for dilute suspensions," International Journal of Multiphase Flow, **23**(3), pp. 425–453.

[70] Gidaspow, D., 1994, *Multiphase flow and fluidization : continuum and kinetic theory descriptions*, Academic Press, Boston.

[71] Kuipers, J., van Duin, K., van Beckum, F., and van Swaaij, W., 1993, "Computer simulation of the hydrodynamics of a two-dimensional gas-fluidized bed," Computers & Chemical Engineering, **17**(8), pp. 839–858.

[72] Darmana, D., Deen, N., and Kuipers, J., 2006, "Parallelization of an EulerLagrange model using mixed domain decomposition and a mirror domain technique: Application to dispersed gasliquid two-phase flow," Journal of Computational Physics, **220**(1), pp. 216–248.

[73] Kim, J. and Moin, P., 1985, "Application of a fractional-step method to incompressible Navier-Stokes equations," Journal of Computational Physics, **59**(2), pp. 308–323.

[74] Choi, H. and Moin, P., 1994, "Effects of the computational time step on numerical solutions of turbulent flow," Journal of Computational Physics, **113**(1), pp. 1–4.

[75] Kim, D. and Choi, H., 2000, "A Second-Order Time-Accurate finite volume method for unsteady incompressible flow on hybrid unstructured grids," Journal of Computational Physics, **162**(2), pp. 411–428.

[76] Kulick, J. D., Fessler, J. R., and Eaton, J. K., 2006, "Particle response and turbulence modification in fully developed channel flow," Journal of Fluid Mechanics, **277**(-1), p. 109.

[77] Wang, L. and Maxey, M. R., 2006, "Settling velocity and concentration distribution of heavy particles in homogeneous isotropic turbulence," Journal of Fluid Mechanics, **256**(1), p. 27.

[78] Fessler, J. R., Kulick, J. D., and Eaton, J. K., 1994, "Preferential concentration of heavy particles in a turbulent channel flow," Physics of Fluids, **6**(11), p. 3742.

[79] Finn, J., 2009, "A multiscale modeling approach for bubble-vortex interactions in hydro-propulsion systems," M.S. Thesis, Oregon State University.

[80] Mohseni, K., Ran, H., and Colonius, T., 2001, "Numerical experiments on vortex ring formation," Journal of Fluid Mechanics, **430**, pp. 267–282.

[81] James, S. and Madnia, C. K., 1996, "Direct numerical simulation of a laminar vortex ring," Physics of Fluids, **8**(9), p. 2400.

[82] Glezer, A., 1988, "The formation of vortex rings," Physics of Fluids, **31**(12), p. 3532.

[83] Kim, J., Moin, P., and Moser, R., 1987, "Turbulence statistics in fully developed channel flow at low reynolds number," Journal of Fluid Mechanics, **177**(-1), p. 133.

[84] Moser, R. D., Kim, J., and Mansour, N. N., 1999, "Direct numerical simulation of turbulent channel flow up to re[sub]=590," Physics of Fluids, **11**(4), p. 943.

[85] Lostec, N., Fox, R., Simonin, O., and Villedieu, P., 2008, "Numerical description of dilute particle-laden flows by a quadrature-based moment method," Annual Research Briefs, Center for Turbulence Research, pp. 209–221.

[86] Roache, P., 1994, "Perspective: A method for uniform reporting of grid refinement studies," Journal of Fluids Engineering, **116**, pp. 405–413.

[87] Roache, P., 2003, "Conservatism of the grid convergence index in finite volume computations on Steady-State fluid flow and heat transfer," Journal of Fluids Engineering, **125**, pp. 731–732.